Isolated direct photon production and the Atlantis event display for the ATLAS experiment

Mark C. Stockton

Thesis submitted for the degree of
Doctor of Philosophy

Particle Physics Group,
School of Physics and Astronomy,
University of Birmingham.

November 2009

Synopsis

A study of the possibilities for a direct photon cross-section measurement is carried out, in the context of expectations for the first LHC collision data from the ATLAS experiment. Comparisons are made between Monte-Carlo predictions and an optimised method of selecting and reconstructing the events from data taken by the detector is described. Also explained is work carried out on the Atlantis event display.

The thesis begins with a general overview of current research in particle physics, motivating the building of the LHC and ATLAS. These are described, concentrating on the main motivations for a direct photon measurement. The Atlantis software is described next, explaining its role in ATLAS and some of its features. This is followed by a more detailed description of the work carried out on improving the existing Atlantis features and expanding the scope of the project.

Following this the steps required in making a direct photon cross-section measurement are laid out, beginning with a theoretical discussion of what direct photons are and why they are interesting to study. Studies carried out with different Monte-Carlo simulations are described. The methods used for trigger, photon and jet reconstruction are laid out along with cuts that can be applied to select pure photon samples. The final generator and reconstruction selections are then laid out step by step in the final chapter, which finishes with an assessment of the achievable precision on the differential cross-section.

Author's Contribution

This work has been carried out as part of the ATLAS experiment. The results shown here relied on the ATLAS software, for the physics analysis, and also the previous work of other developers of the Atlantis event display. The work here is mainly my own, but there have been other contributions to the work as documented here.

- Experiment Overview:

This is a summary of the ATLAS detector, and is based on more detailed descriptions in [1–3].

- Atlantis development:

For the Presentation section, there were many people who provided feedback for the creation of the new colour schemes, with Andreas Hoecker providing a large amount of feedback on colour suggestions. I contributed the expansion of the number of colours, final colour choices and code to accommodate these improvements, along with the anti-aliasing code and new start-up screen. I also contributed to initial tests of openGL code mainly based on code by Adam Davison. The openGL code was improved by Adam and I assisted with the migration into Atlantis. I also updated the configuration files and added the interaction interface to create the special view (although the final display involves further contributions from Adam).

The `LegoPlot` development was based on existing code specific to the `LegoPlot` and other functionality inside Atlantis. The L1calo work was an extension to the `LegoPlot` development, and had other contributions from Qiang Lu (addition of

ROIs), Juergen Thomas (JiveXML), Zdenek Maxa (created ADC count plots for the calorimeters, which I then adapted for L1calo) and the L1calo collaboration (suggestions for the configuration). The end-cap display code was my own, or developed from existing Atlantis code, but with feedback from Peter Watkins and Sven Menke. I am solely responsible for the Atlantis code development for Minerva. For the whole Minerva project the other largest contributions have come from Monika Wielers (talks, events, website French translation, configuration suggestions) and Peter Watkins (general feedback on the project with specific input to configuration and website). Other contributions came from:

* Other website translations: Juergen Thomas (German), Daniel Tapia Takaki (Spanish) and Angela Romano (Italian).
* Website feedback based on an open source Javascript quiz from cstruter.com.
* Minerva Help within Atlantis and exercises by Lauren Lewis.
* Other feedback from Cecilia Kozma, Masterclass events and HST @ CERN.

From the other developments described here Juergen Thomas provided the JiveXML developments to add data for Composite particles and from the MBTS (although I provided the geometry JiveXML development). For the TRT development I was assisted by Zdenek Maxa and Sebastian Fleischmann.

- Simulating Direct Photon Production

The section on Pythia refers to stand-alone use of Pythia, with some code adapted from work by Ivan Hollins [4]. The comparison between Pythia and Herwig use data from centrally produced ATLAS samples in release 12 of the ATLAS offline software.

- Selecting and Reconstructing Direct Photon Events, Direct Photon Cross-section Measurement

In these chapters the analysis uses ATLAS centrally produced Pythia samples in release 13 of the ATLAS offline software. The main details of the photon selection

variables use the ATLAS EGamma group standard definitions, outlined in [5]. The analysis itself uses the ATLAS offline software, with code based on example analysis skeletons, to output ntuples for further analysis within Root.

Acknowledgements

Firstly I would like to thank the staff closest linked to my work, namely Paul Newman (my supervisor), Pete Watkins, Juergen Thomas and John Wilson for their availability, helpful discussion and assistance throughout my research. I would also like to thank the rest of the Birmingham ATLAS and Grid staff for all their support during my PhD. In fact all of the staff in Particle Physics group in Birmingham have been very good to me over my seven years at the University, which has made it very hard to contemplate leaving. Along with the staff, Birmingham has great students and I have relished sharing an office with Ivan, Richard, Chris, Neil, Joseph, Dave and Martin. This also extends to all the students not in my office (a special thanks to Jody and Arvinder for use of their sofas), as we all make up a great group to work and relax with even if we do talk strawberries. Especially from these I mention Dan who became one of my closest friends and was sorely missed by me and the group (hopefully I filled Dan's role as head post-grad well).

I thank the Atlantis developers for making working on Atlantis very enjoyable (even if our meetings are on the long side). For discussions and feedback on my analysis I also thank Andrew Hamilton, Francesca Bucci, Maria Teresa Dova, Martin Tripiana Gorgojo and the others involved in the direct photon note. Similarly I thank the ATLAS Direct Photon, Standard Model and EGamma groups. The last group within ATLAS I would like to thank is the L1calo group who, even though I only contributed to the group via Atlantis, have always made me feel welcome. I also thank all those who have helped with the masterclass project, either helping out on

the day or by giving feedback, especially Monika Wielers for helping produce such clear events for the students to analyse. The JetPhox authors Jean Philippe Guillet and Francois Arleo both have helped me progress with the software, but I especially thank Gudrun Heinrich for the discussions at Durham.

Of course there are also all the students and colleagues at CERN and from conferences who made the PhD really special especially those who visited Chicago, kept me company running (long live CERN UK Ninja Turtles!), or taught me the joys of skiing (even if its given me a scar). Whilst mentioning CERN I should also thank the UK admin staff based at CERN for their assistance on, and STFC for funding, my many productive and enjoyable visits to CERN. Next I would like to thank all my house-mates over the years, all of the congregation from Selly Park Baptist Church and friends from undergrad for being good company and a welcome break from work. I also can not forget all my friends from home (the Ferrers Massive) you guys have always been there for me and I look forward to showing you Geneva.

I thank all my relatives for support and showing interest in my research. Most importantly I would like to thank my parents. You have always only been too happy to help me in any way possible (from just talking on the phone to helping with moving me to and from Birmingham) and have always inspired me to achieve my full potential. I am so grateful that this thesis is dedicated to you.

Contents

List of Figures

List of Tables

Chapter 1

General Overview

Research in particle physics is all about designing the very big, to study the very small. This thesis concentrates on the study of protons, particles from the nucleus of an atom, which have a radius of 10^{-15} m, whereas the LHC, the Large Hadron Collider at CERN, has a radius of 4.3 km. The LHC is an accelerator ring, which fires protons in opposite directions around the ring at nearly the speed of light. As they travel around this ring they are collided in four experimental halls where detectors are placed to view the products of the collisions. One of these is ATLAS, A Toroidal LHC ApparatuS, which is 44 m by 25 m, and is designed to detect the particles produced from collisions of these protons. The aim is that through colliding protons, their constituent parts can be studied and new, previously unknown, particles such as the Higgs boson may be produced.

The type of collisions that this thesis will focus on will be those when photons are produced, where photons are the particles carrying electromagnetic radiation (e.g. light, x-rays, radio waves, etc.). The photons in question are called direct photons, as they originate directly from the interaction between the constituents of the colliding protons, and will have no other particles nearby in the detector (so they are "isolated"). These photons will pass through the detector and be turned

into an electrical signal, in a detector called a calorimeter, which is then interpreted to work out the energy of the photon.

The interpretation of these signals, from the detector, is done by specialised hardware and software. The physicist can then analyse the results from the software to learn more about the physics taking place in the collisions, an example would be to look at the energy of photons created in different collisions. To be able to connect with the physics better, rather than just looking at plots/tables, the physicist can also use event display software to "see" what took place in a single collision. Atlantis is such a piece of software, which graphically displays the detector response to the particles passing through it.

At the time of writing there had been no proton-proton collisions at the LHC, so the work here is based on simulations of what we expect to see. Since then the first collisions (see examples in figure 1.1) have taken place, albeit at low energy. When the LHC begins taking its first high energy data, direct photons will be one of the most prominent and frequent products from the collisions, so there will be plenty of data to study. By comparing the results obtained in the experiment with those predicted by simulations, different models can either by ruled out or improved to get an accurate description of the proton and perhaps to uncover new physics.

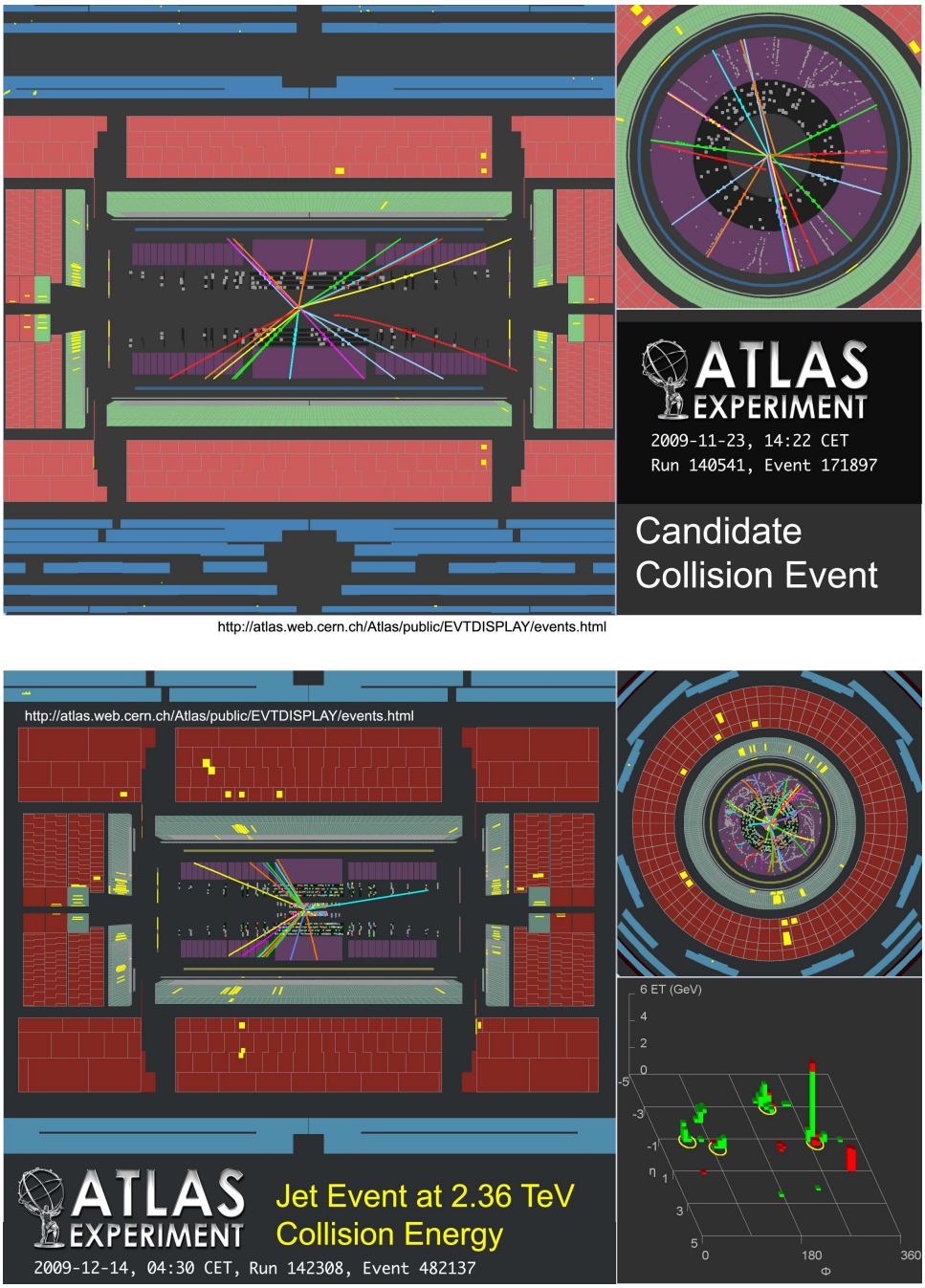

Figure 1.1: Two event display images from the first LHC collisions in 2009 [6].

Chapter 2

Experiment Overview

2.1 Introduction

Since its development in the 1970s the Standard Model [7–11] has been describing the fundamental particles making up the matter around us and the interactions between them. It consists of fermions, the quark and lepton particles which make up matter, and bosons, which control the interactions between the fermions. The Standard Model's predictions have been validated by nearly every experiment designed to test it since its creation. However there are still several elements of the Standard Model which are less accurately known, particularly those involving the strong interaction between quarks. Searching for the physics beyond the Standard Model, along with improving our current understanding, motivates the building of the LHC and ATLAS, which are described in this chapter.

2.2 Motivation and Physics Aims

The Standard Model consists of three generations of quarks and leptons and four gauge bosons, along with their anti-particle pairs where appropriate. Of these not all are observable in a detector, e.g. quarks only exist in bound states. The main objectives for ATLAS are to discover the missing ingredient from the Standard Model, the Higgs boson, and also to search for any new physics appearing from running at higher energy and intensity than has previously been possible.

2.2.1 Standard Model

In the Standard Model context, ATLAS particularly hopes to improve measurements on the top quark, W boson and investigate further the CP violation in the B physics sector. The top quark has been well studied in $t\bar{t}$ events [12] and more recently has also been observed in single top events [13]. This is the heaviest quark, hence why it was the last to be discovered, and has a mass of 171 GeV, compared to the other quarks which are all lighter than a ~ 5 GeV. The accuracy of the top quark mass measurement is down to 2 GeV, and apart from confirming the result, further measurements at the LHC can improve the accuracy of this measurement. The top quark decays to another lighter quark, $> 99\%$ of the time to b quarks, either leptonically or hadronically.

In the leptonic case a neutrino and lepton will be created. As the neutrino is so weakly interacting it is not possible to make a detector to measure all neutrinos produced. Instead they are inferred through missing energy, this requires an accurate knowledge of all energy in the calorimeters. For the leptons, all types require tacking information; electrons require accurate electromagnetic calorimeters; muons also require extra muon tracking to help identify them at high luminosity when the tracker will become highly occupied. In the hadronic case at least three jets will

be created from one top quark, so it is key to be able to accurately resolve these (although this is difficult for top quarks with large transverse momentum, as the jets produced are likely to overlap partly/fully) and to be able to tag the flavour of the heavy flavour jet, also needed for the b quark in the leptonic case.

Also requiring flavour tagging, including reconstruction of secondary verticies, is the wide ranging B physics program in ATLAS. Results in this area are important for studying CP violation, not only for understanding symmetries in particle physics, but also for cosmology, as it can provide an explanation of the matter anti-matter imbalance in the observable universe. In fact these results may gain even more importance, as recent results have shown for example that measurements of the B_s can probe new physics with high sensitivity [14]. Further studies [15] of B physics can probe further the Cabibbo-Kobayashi-Maskawa unitarity triangle and rare B decays.

The W and Z bosons are the particle physics equivalent of the astronomy standard candle. They have very accurate precision, better than 0.05% on their mass, and so can be used to confirm predictions from extrapolating theories from one experiment to another at a different energy. Again these require accurate leptonic measurements and also missing energy in the case of W bosons decaying leptonically. Along with validating previous results, they can also be used to probe further the parton density functions and gauge boson couplings (e.g anomalous triple gauge couplings [16]).

2.2.2 Higgs

The Higgs is crucial to the Standard Model, as it is the particle controlling the mass of the other particles. It has not been observed in an experiment to date: results from LEP [17] found 17 candidate events and set a lower exclusion limit, which the Tevatron has begun adding to, as shown in figure 2.1. As shown in figure

2.2a, the Higgs decays to a large range of particles. Optimising the measurement of each of these channels, means that the overall significance of a possible Higgs observation improves. This adds to the detector requirements the need for accurate photon measurement, as at a low mass the $\gamma\gamma$ channel provides a far cleaner event signature compared to the other low mass decays.

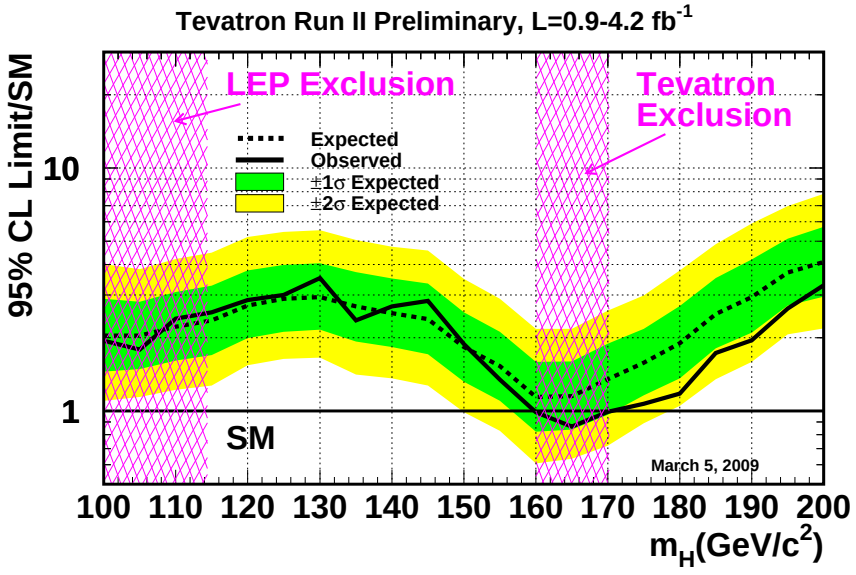

Figure 2.1: Exclusion regions for the mass of the Higgs, updated with results from the Tevatron [18].

As with the top quark, the Higgs has a large mass so also requires a high energy accelerator, to provide a large enough centre of mass energy to create real Higgs bosons. In fact, the Higgs, or some other related new physics, must be found below around 1 TeV, to avoid unitarity problems with W and Z couplings, so making sure that this energy range can be probed is crucial. The other problem with the Higgs is that its cross-section is small, shown in figure 2.2b, so to be able to obtain enough events the accelerator must have a large luminosity.

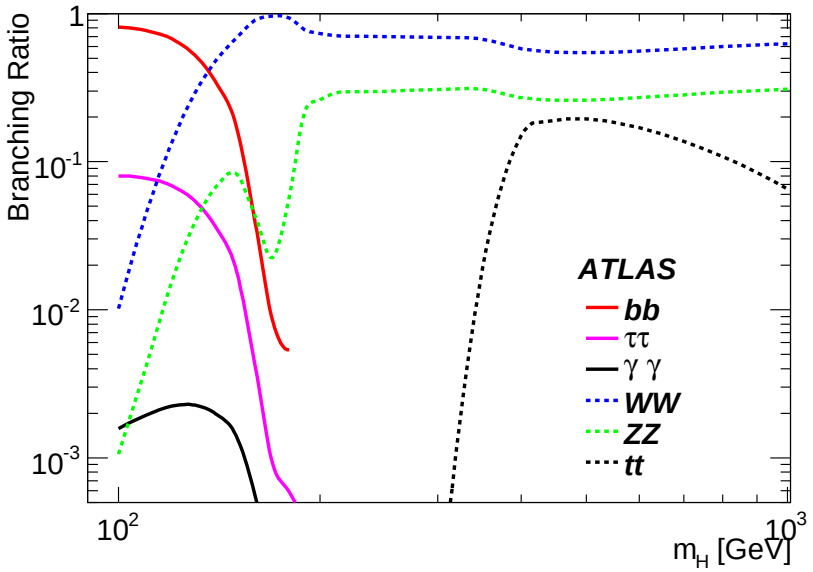

a)

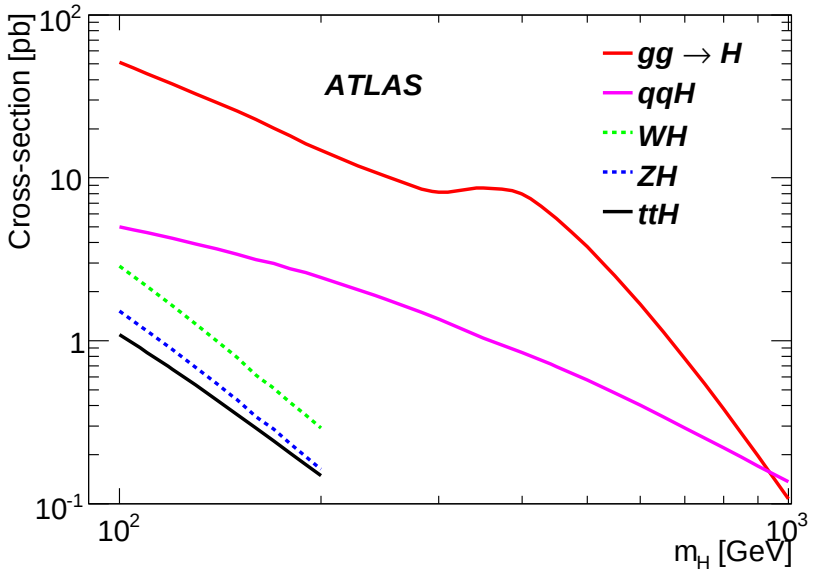

b)

Figure 2.2: Higgs a) decay branching ratios and b) production cross-sections at the LHC with centre of mass energy= 14 TeV [19].

2.2.3 Beyond the Standard Model

Even with a completely constrained Standard Model the story would not be over for particle physicists. There are still many effects which the Standard Model does not address which is why the LHC is also set up to search for supersymmetric particles, extra dimensions and any other new physics. Missing energy will be a crucial in identifying many new particles, as in many models supersymmetric particles do not interact with normal matter. However, supersymmetric signals may be more prominent than neutrinos in the top quark case as the missing energy can be much larger. The best sign of new physics is to find resonances in mass spectra, but the other main principle of looking for new physics is looking at the shape of particle momentum distributions (for example supersymmetry models alter the shape of the di-jet mass distribution [20]), which is most noticeable at high values of momentum. There are many different models/scenarios of new physics. As well as searching for each individually ATLAS will make accurate measurement of leptons, photons, jets and missing energy and then search for any deviation from the Standard Model predictions. As these searches are at high momenta, and can be for particles with large mass, the energy provided by the accelerator is critical. However, a large luminosity is also needed, as the production of supersymmetric particles at energies above threshold has a small cross-section, which often falls with centre of mass energy.

2.3 LHC

The LHC has been designed to achieve the highest possible luminosity with the largest possible energy, limited by magnet technology and the existing tunnel from its predecessor accelerator, LEP. The LHC is the final synchrotron in the chain of accelerators, as shown in figure 2.3, to get the protons to the required energy. The pre-accelerator chain also includes previous CERN energy frontier accelerators.

The proton's route starts with hydrogen atoms being stripped of their electrons and then accelerated up to 50 MeV through a linear accelerator, LINAC2. The protons then pass around three storage rings, PS Booster, PS and SPS, where the protons keep being accelerated until they reach the LHC injection energy whilst also being combined into bunches. After reaching an energy of 450 GeV the protons are injected into the main LHC accelerator, where they are accelerated to the final collision energy, with a designed maximum energy of 7 TeV. However in early running an energy of 5 TeV will be used[†].

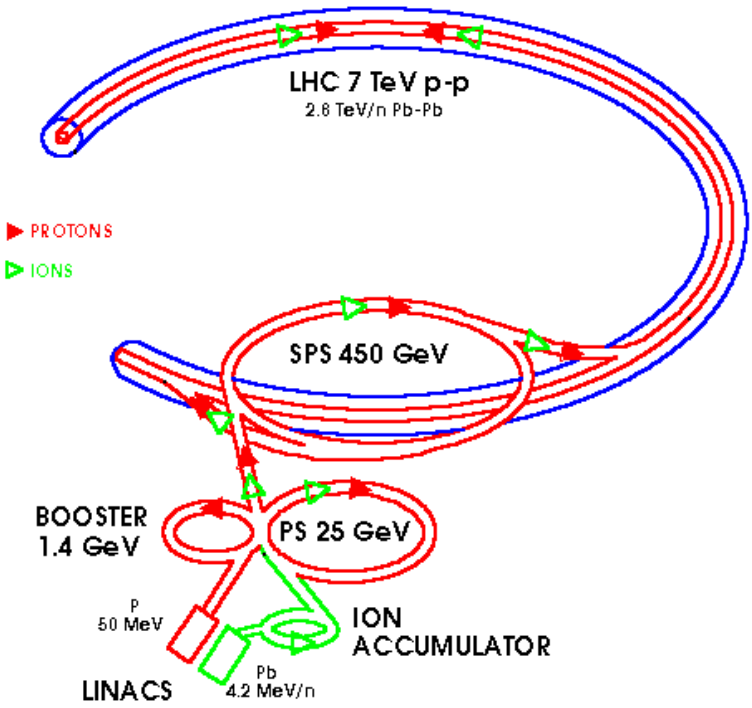

Figure 2.3: The accelerators used to get protons into the LHC and up to 7 TeV [21].

One downside of circular accelerators is synchrotron radiation, which is released as the ultra relativistic protons are accelerated in a circular motion by the magnetic field, lowering the beam energy. However by keeping the bunches circulating in a storage ring, such as the LHC, more interactions can occur from the same amount

[†]At the time of writing the first LHC collisions will be at the injection energy, quickly followed by beams of 3.5 TeV, increasing towards 5 TeV at the end of the first run.

of original particles compared to linear colliders. Along with the beam energy the other main characteristic of an accelerator is the luminosity, the number of events per unit cross-section, it can achieve per second, determined by:

$$Luminosity = nf\frac{N_1 N_2}{A} \tag{2.1}$$

where there are n bunches in each beam revolving at a frequency f, with N_1 and N_2 particles in the colliding bunches which have an overlapping area of A. For the first run of the LHC the luminosity will be at $10^{31}\text{cm}^{-2}\text{s}^{-1}$, and will accumulate a data sample of around 200 pb^{-1}.

Increasing the luminosity is the only way to collect increased yields of events of processes with low cross-sections. Unfortunately increasing this luminosity, by increasing the number of particles in a bunch, also increases the number of interactions per bunch crossing. For the design peak luminosity, $10^{34}\text{cm}^{-2}\text{s}^{-1}$, there are around 23 interactions on average per bunch crossing [22]. This is calculated from the total proton-proton cross-section, creating a Poisson distribution with a mean at 23, but with a shape which is independent of luminosity. So for the starting luminosity, $10^{32}\text{cm}^{-2}\text{s}^{-1}$, this is 100× less than the optimal running, i.e. a mean of 0.23 events (assuming the same number of bunches at low and high luminosity). Therefore most of the time when an event is triggered there should only be 1 interaction. In early running this effect, known as pile-up, should not be an issue, but later on, especially for the proposed SLHC [23] with 10× the LHC luminosity, pile-up will have to be carefully dealt with by the detector.

2.4 ATLAS

The ATLAS detector is placed at point 1 on the LHC ring as shown in figure 2.4. Figure 2.5 shows that the detector is split into different subdetectors, which all have different roles in resolving the particles created in the collision. The detector nearest

to the beam line is the inner tracking detector: for identifying charged particles and secondary vertices. Next come the calorimeters, to determine the particle energies, and finally there are muon chambers for detecting minimum ionising particles that are able to travel through the rest of the detector. The name ATLAS refers to the toroid magnet system in the muon chambers which is complemented by a solenoid magnet between the Inner Detector and calorimeters. Further along the beam pipe there are also other detectors covering the very forward region. The whole experiment is linked by the trigger system which has the role of deciding which events are read out to disk.

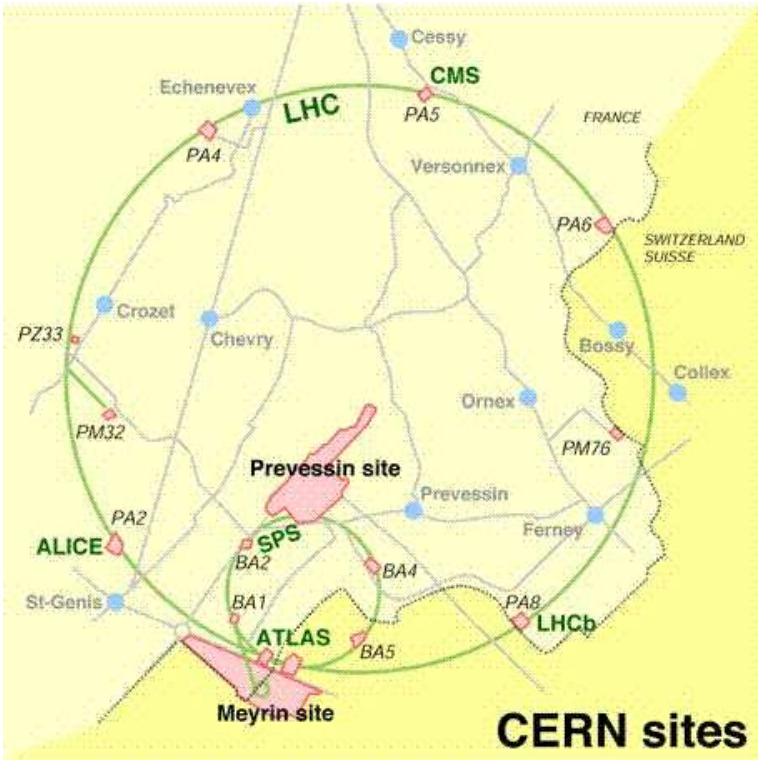

Figure 2.4: Image showing the four experiments on the LHC ring [24].

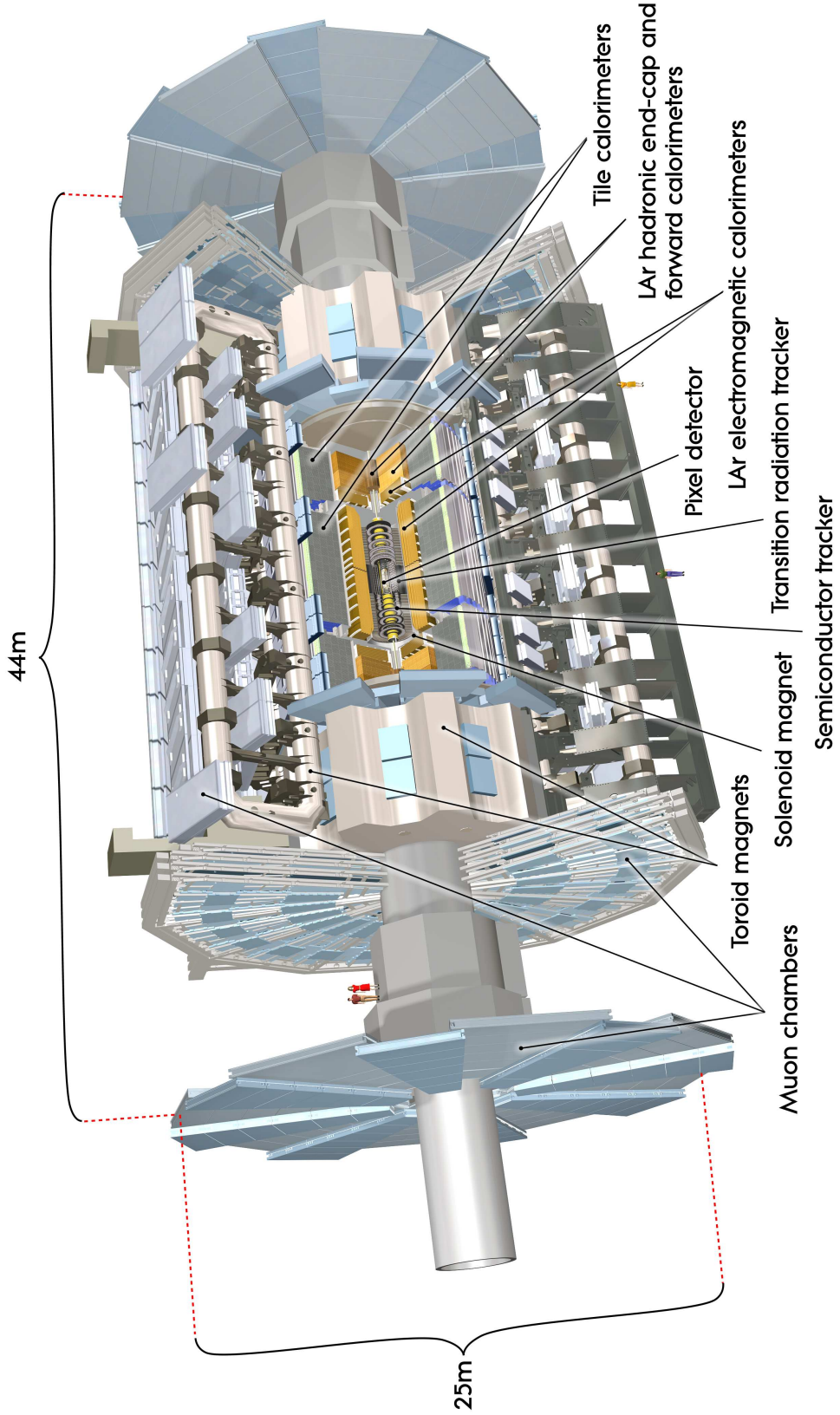

Figure 2.5: Image showing the ATLAS detector [25].

2.5 Coordinates

To understand the geometry of the detector there are several coordinate systems used. The simplest is x, y and z where: the z direction is along the beam line, the positive x axis points to the centre of the LHC ring and the positive y axis points upwards. Then in polar coordinates: θ is the polar angle from the beam axis, ϕ is the azimuthal angle around the beam axis and $\rho = \sqrt{x^2 + y^2}$. Other useful quantities are the pseudorapidity, $\eta = -\ln(\tan(\theta/2))$, and the separation distance between two directions, $\Delta R = \sqrt{\Delta\eta^2 + \Delta\phi^2}$. Many quantities are computed transverse to the beam axis in the x-y plane, e.g. transverse momentum (p_{T}).

2.6 Before the Calorimeters

The Inner Detector, figure 2.6, covers a region of $|\eta| < 2.5$ and is made up of several types of tracker with increasing radius: silicon pixel (Pixel); silicon microstrip, "semi-conductor tracker", (SCT); and straw tubes, with transition radiation material, (TRT). The Pixel and SCT trackers have high granularity to produce precise measurements of track parameters, in an environment with a high density of tracks, and for finding primary and secondary vertices. These detectors are costly in money and material, so are limited to only 3 pixel layers and 8 SCT layers. The TRT then provides typically 36 tracking points per track at a much lower cost in money and material, giving a highly accurate momentum measurement and enhanced electron identification, from transition radiation. Being the closest detector to the beam line the radiation damage after a few years of running will force the Pixel tracker to be replaced.

Surrounding the Inner Detector is a 2T solenoid, to enable the precise measurements of the momentum of charged tracks from the track sagitta in the solenoidal field. Locating the solenoid inside the calorimeter reduces its cost, but to achieve

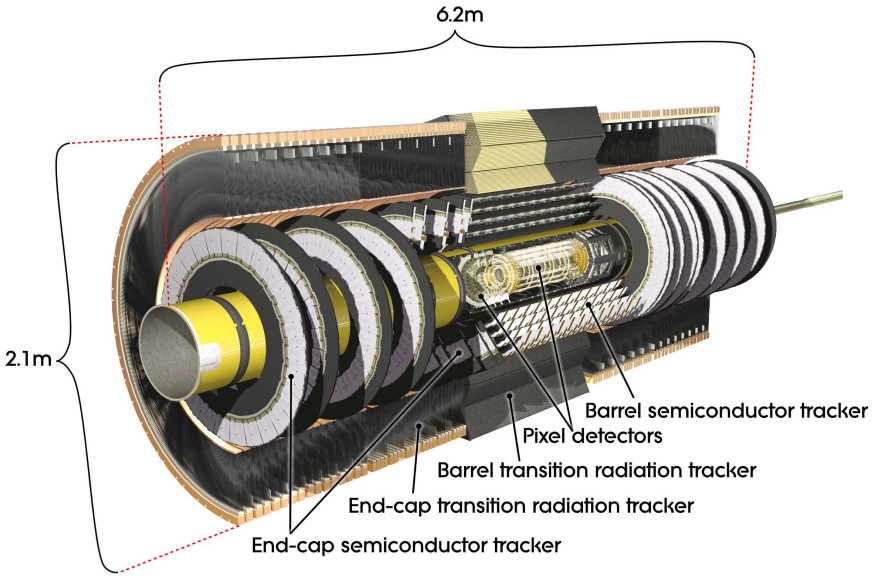

Figure 2.6: The Inner Detector [1].

this the solenoid had to be designed to add as little material as possible in front of the calorimeter. For example, the calorimeter and solenoid share a vacuum chamber to remove two vacuum walls. The solenoid; tile calorimeter, which acts as the return yoke, and toroid magnets, discussed in section 2.8, are all shown in figure 2.7.

2.6.1 Conversions

One reason for reducing the material in the Inner Detector and solenoid is to reduce the number of photon conversions, to e^+e^- pairs, occurring before reaching the calorimeter. The actual amount of material in these parts can be seen in figure 2.8, showing the total before and after the LAr presampler, described in section 2.7. This corresponds to $\sim 80\%$ of photons converting before the calorimeter. In fact $\sim 40\%$ of photons convert in the Inner Detector alone, which affects the accuracy of measuring photons. Figure 2.9 shows these Inner Detector conversions, showing that the details of the Inner Detector can clearly be seen from reconstructing the $\gamma \rightarrow e^+e^-$ vertex in a sample of 90000 conversion electrons.

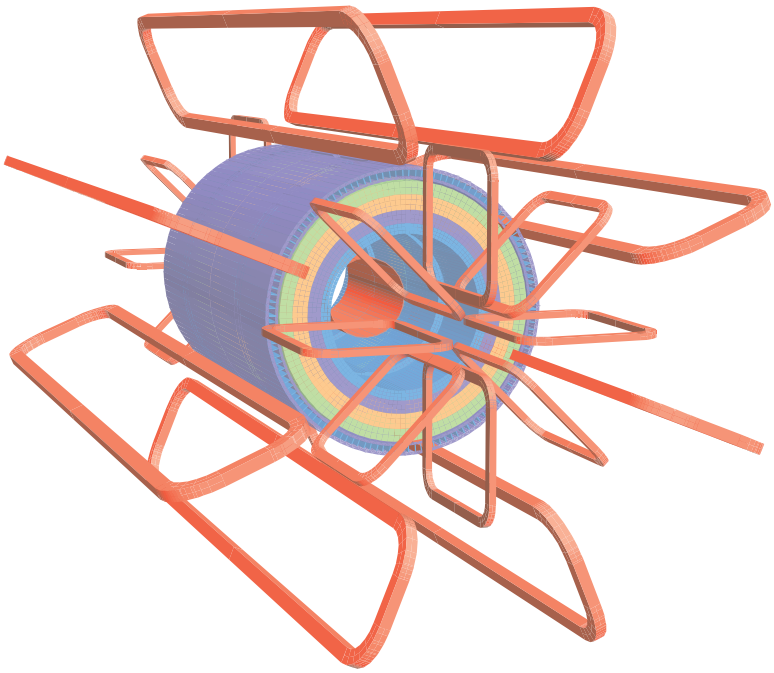

Figure 2.7: The magnet system (red) and layers of the tile calorimeter steel (central cylinder) [1].

2.7 Calorimeters

Figure 2.10 shows the layout of the calorimeters in ATLAS. As in other experiments they are split into electromagnetic (EM) and hadronic (HCAL) sections, of which the EM part is the most important sub-detector for the reconstruction of photons, as described in section 7.6.

The EM calorimeter is made of liquid-argon active material (hence is also given the name LAr) between lead absorber plates and extends over $|\eta| < 3.2$. It is symmetric in z and rotationally symmetric in ϕ, a quadrant is shown in detail in figure 2.11. This shows that it is split into a barrel region of $|\eta| < 1.475$ and an end-cap of $1.375 < |\eta| < 3.2$. However the region $1.37 < |\eta| < 1.52$ is not used for precision physics as there is a large amount of material in front of the calorimeter (from the boundary of cryostats in the Inner Detector), as shown in figure 2.8. There

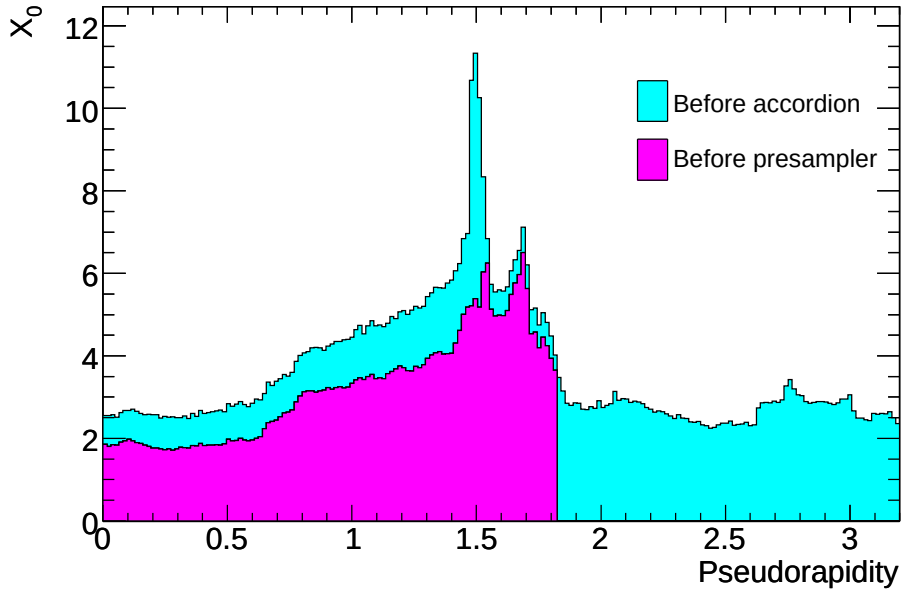

Figure 2.8: The material before the accordion structure (see figure 2.12) and presampler layer of the EM calorimeter (section 2.7) as a function of η, measured in radiation lengths (X_0) [1].

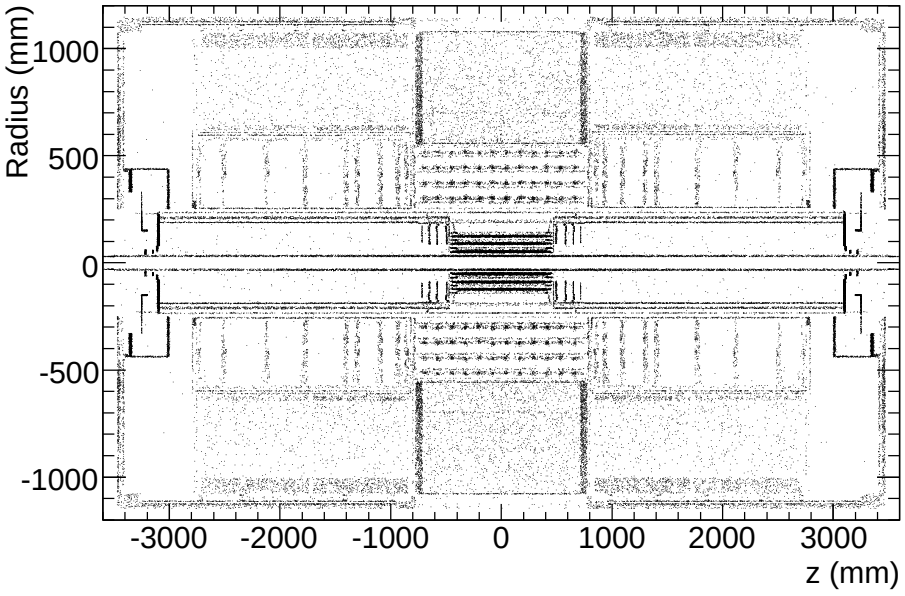

Figure 2.9: Simulated photon conversion verticies in the Inner Detector [1].

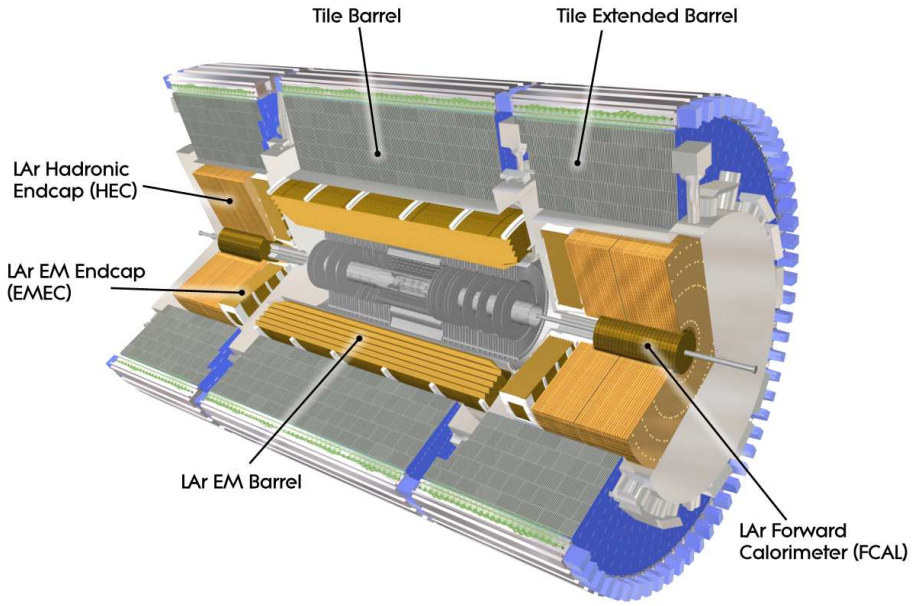

Figure 2.10: The ATLAS calorimeters [1].

is also a split where the two parts of the calorimeter are joined at $\eta = 0$.

In front of the EM calorimeter is a Presampler layer over $|\eta| < 1.8$ to correct for energy lost before particles reach the main three layers of the calorimeter. This is achieved by adding the energy deposited in the presampler, weighted as a function of η to account for the different amounts of material in front of the calorimeter, to the total particle energy. As the Presampler only picks up energy from charged particles, it is also used for identifying photon conversions.

The lead absorber and electrodes for readout in the main layers have an accordion shape to give full and uniform ϕ coverage and a faster signal readout. Ganging the electrodes together provides ϕ separation, with etching of the electrodes providing the η and depth separation. By varying the thickness of the lead with η the energy resolution can be optimised. In the first layer the cells are strips in ϕ with narrow width in η, with dimensions in the barrel of $(\Delta\eta \times \Delta\phi)$ 0.0031×0.098, the other two layers forming cell shapes of 0.025×0.0245 and 0.05×0.0245, as shown in figure

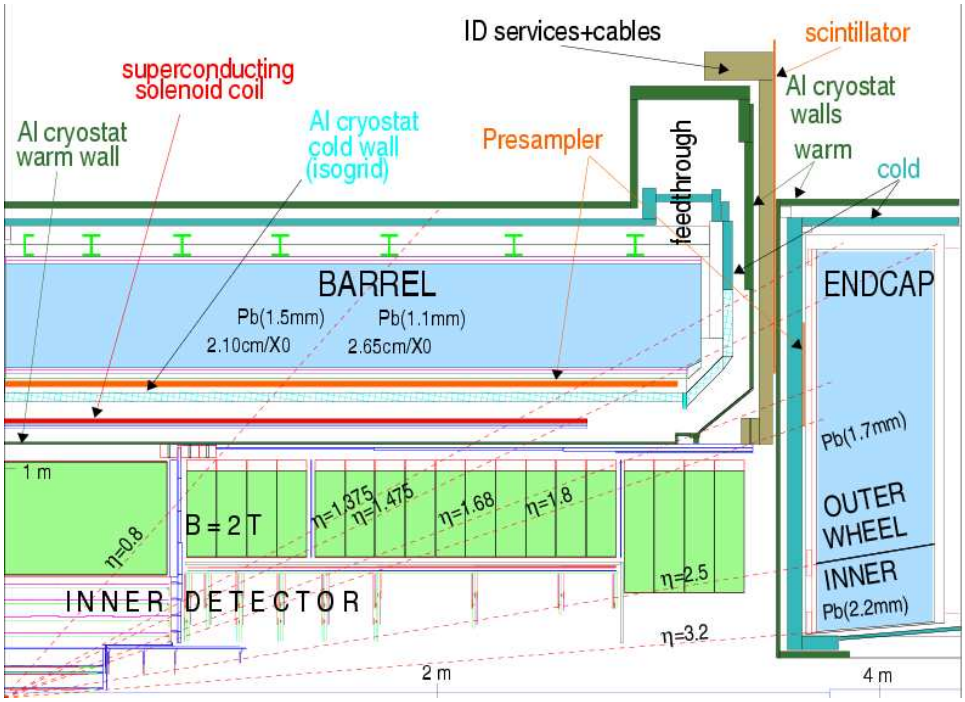

Figure 2.11: A quadrant of the EM calorimeter [26].

2.12. The dimensions of the cells are similar in the end-cap, except for the region $2.5 < |\eta| < 3.2$ where there are only two layers.

The strip layer is used for π^0/γ separation. When the π^0 decays, the resulting two photons will be spatially separated so the high granularity of the strips will be able to distinguish a π^0 from a single photon at all but the highest energies. The middle layer, square cells, provides most of the depth of the EM calorimeter, as shown in figure 2.13. This layer is where most of the electromagnetic energy is absorbed and is also used to study the width and isolation of the shower. The final layer of cells, rear cells, increases the total radiation length, to over $25X_0$ in the barrel, which is needed to contain very high energy electron and photon showers inside the EM calorimeter.

The HCAL barrel region covers $|\eta| < 1.7$ outside the EM calorimeter and uses plastic scintillator tiles embedded in iron absorber. It is responsible for stopping

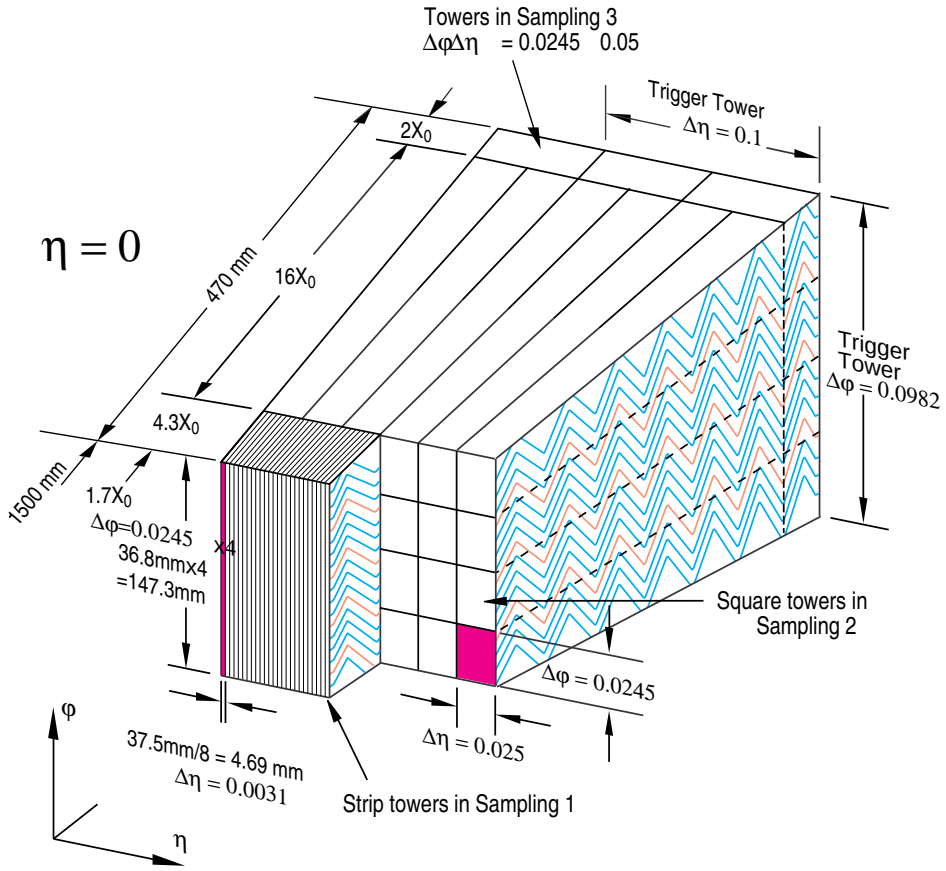

Figure 2.12: The EM calorimeter barrel cell structure [26], showing the three layers and accordian structure (and ganging) of the electrodes.

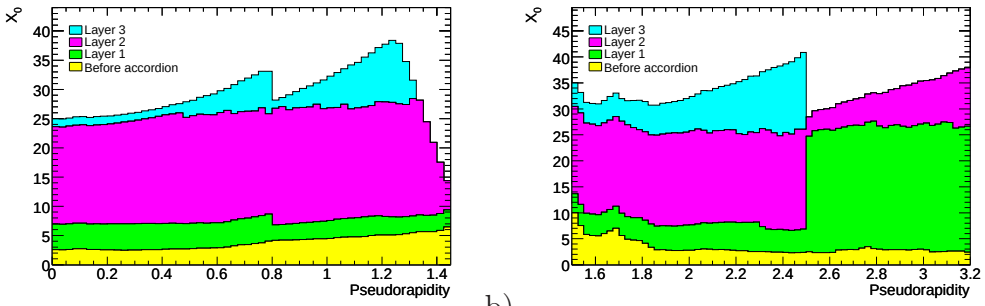

a) b)

Figure 2.13: Cumulative radiation lengths in the a) barrel and b) end-cap parts of the EM calorimeter [1].

hadrons that pass through the EM calorimeter and measuring their energy. The hadronic end-cap calorimeter (HEC) covers $1.5 < |\eta| < 3.2$. The HCAL is indirectly used in photon reconstruction, for removing backgrounds. Photon showers should be contained inside the EM calorimeter, so a candidate shower with leakage into the HCAL is likely to not be a photon, unless the photon has a large enough energy. For this to occur the photon would need to have an energy of above 500 GeV [26].

The remainder of the calorimeter coverage comes from the Forward calorimeter (FCAL) in the region $3.2 < |\eta| < 4.9$. Both the HEC and FCAL use liquid-argon with copper absorbers and also tungsten absorbers for two of the FCAL layers. They are both located inside the end-cap cryostat along with the LAr end-cap and the minimum bias trigger scintillators (MBTS). The MBTS are important for observing low transverse momentum inelastic pp scattering in early minimum bias measurements and can hence be used for luminosity measurements.

2.8 Other Detector Elements

The outermost layer of the detector is the muon system, which is made up of 4 components: Monitored Drift Tubes (MDT), Cathode Strip Chambers (CSC), Resistive Plate Chambers (RPC) and Thin Gap Chambers (TGC), all shown in figure 2.14. The triggering is carried out by the RPCs in the barrel and TGCs in the end-cap regions, covering a total range of $|\eta| < 2.4$. These also provide second coordinates for the more precise MDTs and CSCs. The MDTs give accurate momentum measurements over most of the detector, with the CSCs covering $2 < |\eta| < 2.7$, as these can withstand the higher rate in this region.

As can be seen from figure 2.14, the muon system also has its own magnet system. In this case there are toroids in both the barrel and end-cap regions as shown in figure 2.7. The superconducting air-core toroid magnets are placed inside the muon chambers and are split into barrel ($|\eta| < 1.4$) and end-cap ($1.6 < |\eta| < 2.7$) regions,

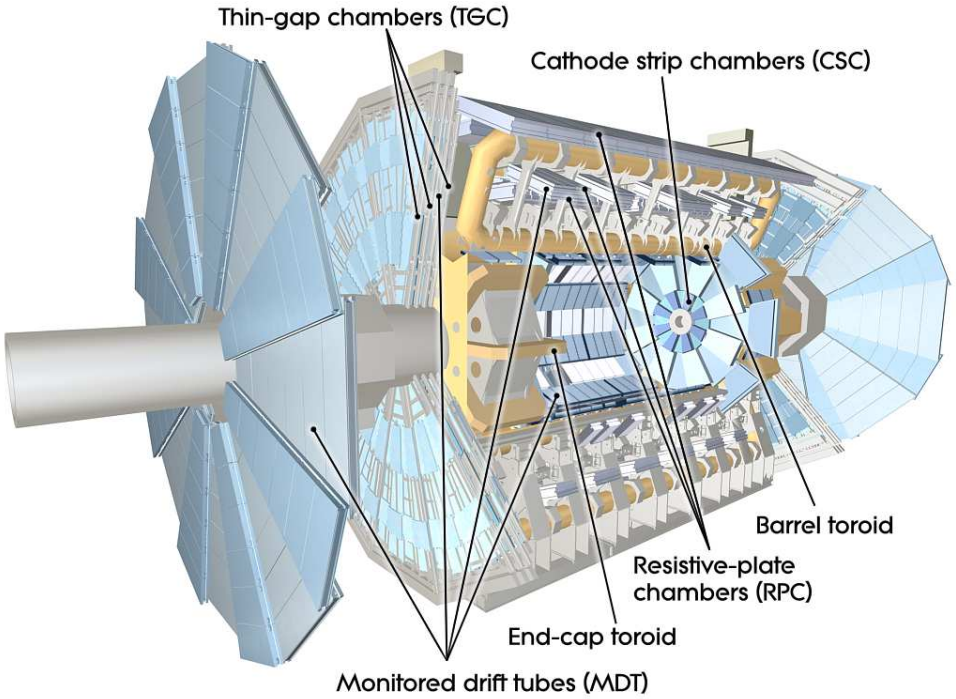

Figure 2.14: The muon detector and magnet system [1].

with fields of 0.5T and 1T respectively. The design of these toroids is very distinct to ATLAS and their scale can be seen in figure 2.15, just after their installation was completed.

Along with the main detectors described above there is also a group of forward detectors, as shown in figure 2.16. This consists of: LUminosity measurement using Cerenkov Integrating Detector (LUCID), Zero-Degree Calorimeter (ZDC) and Absolute Luminosity For ATLAS (ALFA). LUCID uses Cerenkov tubes to detect inelastic p-p scattering to provide an online relative luminosity. The ZDC detects very forward neutrons in heavy ion collisions and consists of quartz strips between tungsten absorber plates. Finally the Roman-pot ALFA detector will calculate the absolute luminosity by measuring elastic p-p scattering.

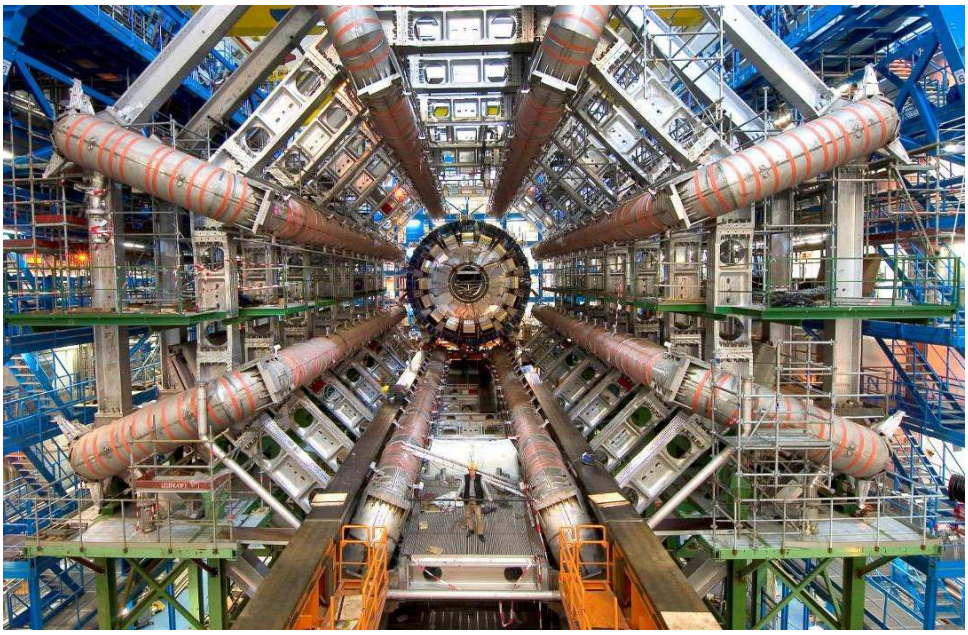

Figure 2.15: The toroids after installation [1].

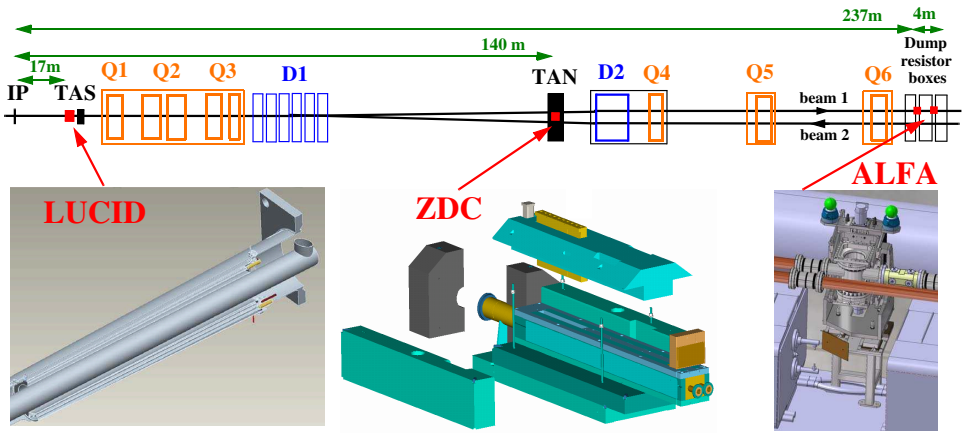

Figure 2.16: The ATLAS forward detectors [1].

2.9 Trigger and Data-acquisition

The pp interaction rate, at full luminosity, at ATLAS is of the order of 1 GHz [2] (bunch crossing rate 40 MHz with 23 interactions per bunch crossing), creating far too much data to be stored. Most of this data is not interesting for physics analysis. As a result a trigger system is designed to trim this rate down to a more manageable data flow. It comprises three levels, which in turn reduce this rate to $\sim$ 100 KHz, $\sim$ 1 KHz and finally 100 Hz. Each of the levels use cuts to decide whether to keep the event, which is based on the fast, relatively crude, reconstruction of physics objects (like jets, photons, electrons, muons). These cuts for each object are called items, which can be true or false depending if all the cuts for an object are passed.

All the data is stored in pipelines until the first level (Level-1, or L1) makes its decision from items based on trigger towers, combinations of calorimeter cells, and muon data from the RPCs and TGCs. These pipelines give L1 a latency of 2.5 μs and upon an event passing L1 are read into buffers, creating deadtime of 4 bunch crossings [27]. When L1 accepts an event it also produces regions of interest (ROI), which describe the position and p_{T} of the physics objects found. The second level of the trigger (Level-2, or L2) uses these ROIs to select data from the buffers at a higher granularity. Events now pass through the event builder to combine all the separate buffers from different detector components and then pass through the final trigger level (Event Filter, or EF). This is adapted from more complex offline algorithms, which are unable to be used at L2 due to its latency constraints of 1-10 ms depending on the event. Events that pass all three levels are then passed to mass storage for offline analysis.

Chapter 3

Atlantis Features

3.1 Introduction

An event display is a way of looking at what is happening in the detector while the experiment is running, or for studying stored/simulated data. It can give clear pictures of what actually took place in a single event rather than studying groups of events in histograms. Atlantis is the ATLAS event display and is based on DALI, the event display for ALEPH [28]. This chapter gives a brief overview of its basic features and examples of it in use.

3.2 Why Java?

DALI was written in FORTRAN but Atlantis has been changed to use Java. One of the best reasons to change to use Java is that it is platform independent. This means that developers, in general, can write code without knowing about the user's operating system. In fact the developers themselves use different operating systems.

For the user, the only requirement to launch Atlantis[†] is that Java has been already installed.

Java also has a very useful function called Webstart which allows software to run from a click on a weblink, with any installation and file transfer hidden from the user, a second click on the weblink checks for updates before running the software previously downloaded. Due to this, Atlantis is the easiest piece of software to start in ATLAS. As it is lightweight software, i.e. small in physical size with low performance requirements, it can be installed on a laptop, meaning events can be looked at anywhere, by anyone.

3.3 Overview

The main ideas behind Atlantis are that it should be fast, intuitive and capable of displaying complete ATLAS events. Achieving this revolves around using many 2D projections rather than using 3D images, which makes the drawing quicker. By allowing several projections to be viewed at the same time, the user can gain the same information as a 3D display and due to the complexity of the events and the detector, these multiple 2D projections usually produce a simplified, more easily digestible representation.

Atlantis works by having two main windows: Canvas and GUI. The GUI, shown in figure 3.1, is where the user selects which data to display, how to display it and how to interact with the Canvas. The Canvas itself, shown in figure 3.2, is split up into different configurations of sub windows depending on the selected layout and window choices, as shown by the "window control" section of figure 3.1.

[†]Launched by using the command: `java -jar atlantis.jar.` after extracting the downloaded zip archive.

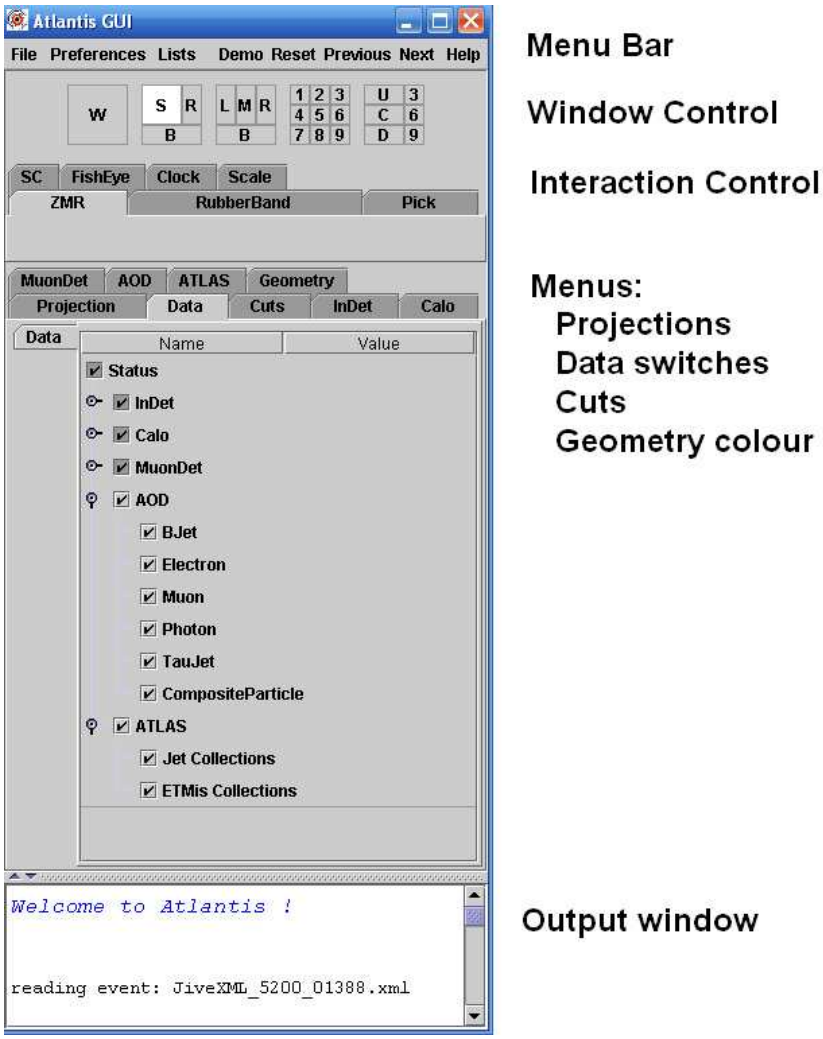

Figure 3.1: The Atlantis GUI and explanation of sections.

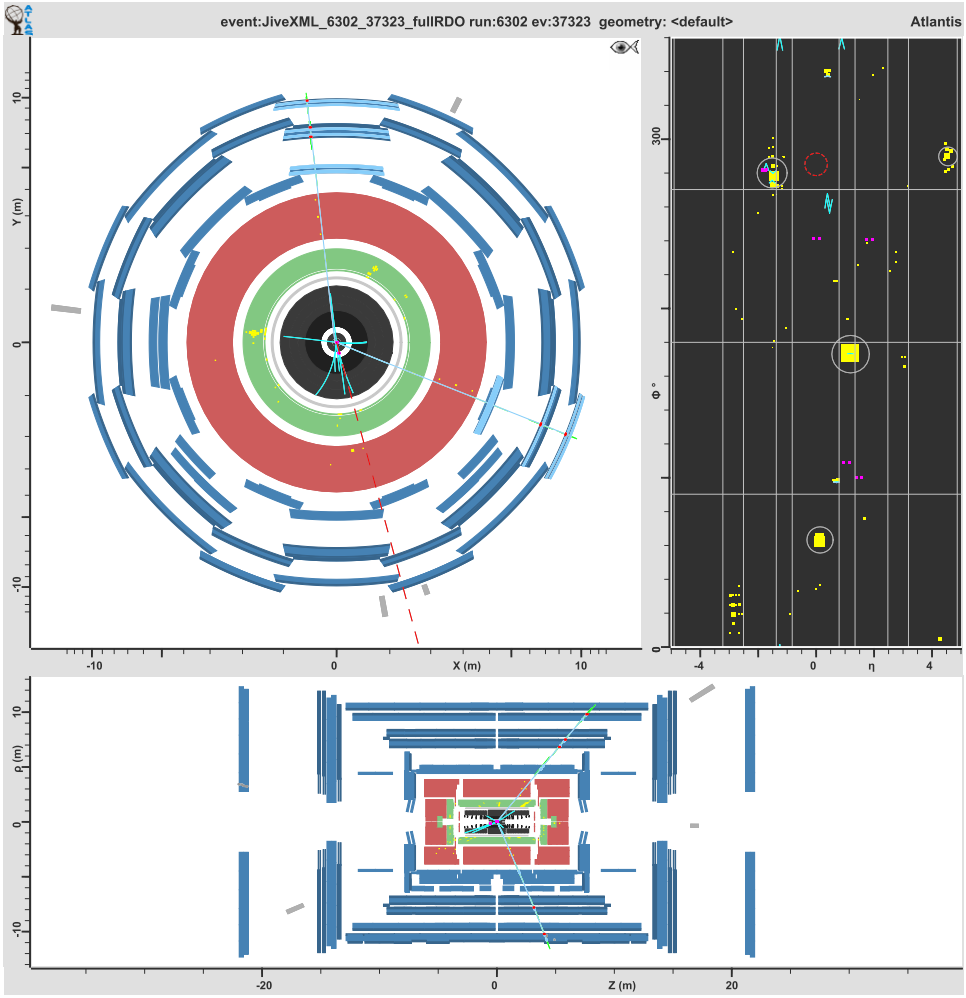

Figure 3.2: The default view of the Atlantis canvas.

3.4 Events

The events displayed in Atlantis are stored in xml files, which are produced by using the JiveXML package[†]. These can then be viewed individually, or combined into a zip archive, which Atlantis can cycle through using the previous/next event buttons. Instead of creating all the event xml files before running Atlantis, an on-line mode can be set up where Atlantis runs at the same time as newly recorded events are being produced and shows each one once they have been processed. This can be used when real data is being taken, allowing Atlantis to be used in the ATLAS control room to check for real time problems in the detector.

3.5 Projections

Figure 3.3 shows nine of the ten Atlantis projections based on the ATLAS coordinates (section 2.5), with the most used being the: y verses x, `YX` ; the ρ verses z, $\boldsymbol{\rho}$`Z` ; the ϕ verses η, $\boldsymbol{\phi\eta}$; and the `LegoPlot` , see section 4.3. Some of the projections have specific uses: the `3DBox` is used to look for secondary vertices and the `Residuals` shows the track residuals for a selected track. Each of the windows can display any one of these projections and the same projection can be displayed differently on two windows, e.g. at different zoom levels.

3.6 Interactions

The interactions are what make the event display much more than just a nice picture, with the most used of these being:

[†]This can be run during real data taking or Monte-Carlo event generation by applying the command `doJiveXML=true`, producing a separate xml file for each event the user runs over.

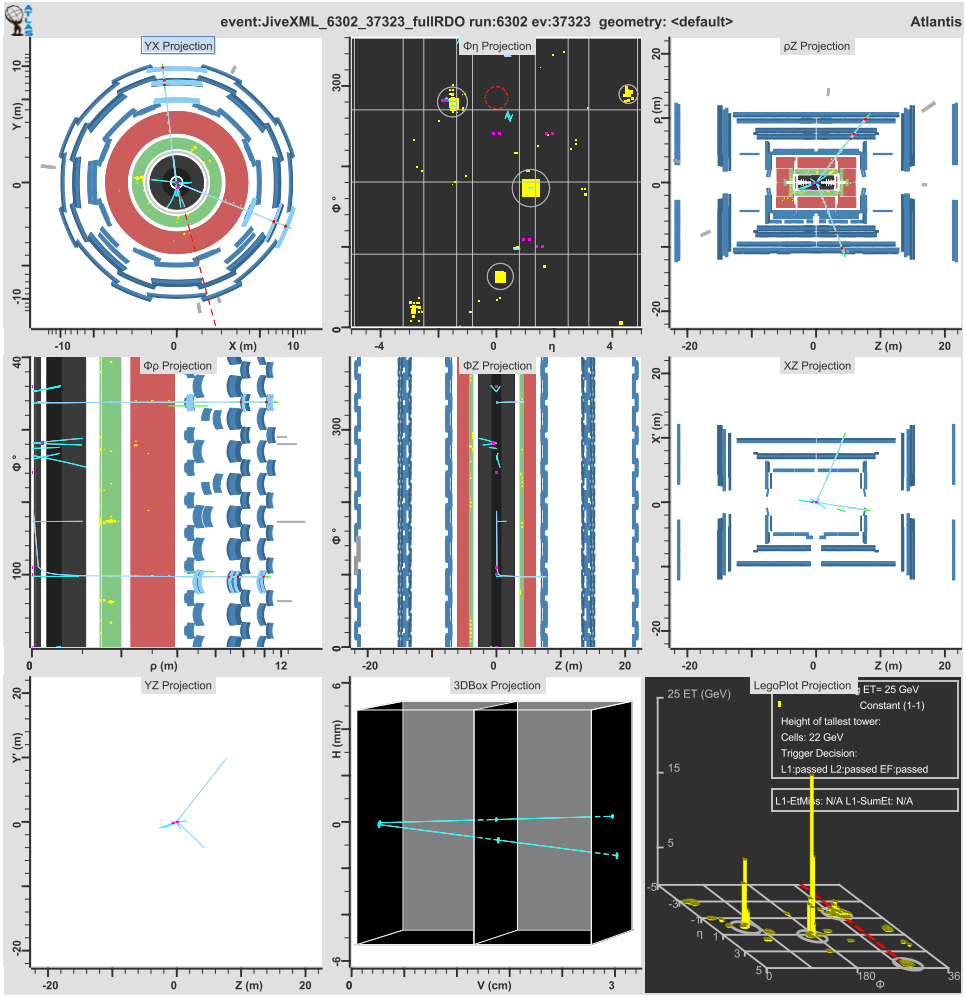

Figure 3.3: Nine of the projections available in Atlantis.

- ZMR - allows the user to Zoom/Move/Rotate the selected projection.
- Rubberband - allows the user to select a certain region and then to zoom or output information, to the GUI, about what is in this region.
- Pick - the user can select an item of data to find out its details (energy, η, ϕ, etc.), which appear in the GUI output window, and can also find where it appears in the other projections. Extra details can also be plotted e.g. ADC counts as shown in section 4.4.
- Synchro Cursors (SC) - shows where the cursor position is on multiple projections at the same time.
- Fisheye - used to magnify the inner part of the projection to allow better viewing of the Inner Detectors.

Each of these interactions has more than one operation available. These are available by using the modifier keys: e.g. `Z`=Zoom, `M`=Move and `R`=Rotate for the ZMR interaction. For the dexterous, these can be used by holding a key and then using the mouse as normal, but as this can prove to be difficult on a laptop a window loaded from the help menu allows the operation required to be selected, removing the need to hold down a key.

3.7 Data

Atlantis is capable of showing all the ATLAS datatypes, from cells to reconstructed objects, see section 7.2. All of the datatypes are then drawn on top of their respective detector, apart from the reconstructed objects which are drawn as histograms around the outside of the detector. Some datatypes can be produced by several algorithms within a single event, so a "multiple collection" option allows the user to select the required algorithm for these datatypes. All this information would overcrowd the display if was all present simultaneously, so each of the datatypes can be switched on or off, on all windows or on specific windows. This uses a feature of the GUI where

each parameter can be set to local or global depending on whether the parameter setting is to apply to one window or to all windows respectively. To further simplify the display, basic ATLAS cuts are applied. By default these have reasonable physics motivation behind their values. The cuts are fully customisable by the user, so the values can be set to match the specifics of a particular analysis.

Once the user is happy with the objects that are displayed, the look of the display can be improved through many colouring options. This ranges from simple colour by type/index, to select individual object colours; or selecting object colours via lists[†]; or more complicated still, using associations[‡]. A few examples of these options are explained below:

- Constant: user chooses the one colour used for a given datatype.
- Calorimeter Layer: all cells in the same layer will have the same colour.
- ECAL/HCAL: colour all EM calorimeter cells one colour and HCAL another (related to detector colours).
- Energy: use a special colour map where each colour maps to an energy range, determined on an event-by-event basis.
- Calorimeter Jet: colour cells according to the jet associated to the cells.
- Object: Similarly tracks and clusters can be coloured to reflect the reconstructed object they are associated with. For cases where multiple associations are present the colour is chosen in a pre-defined order of preference: Electron, Photon, Muon and finally Jet.
- Sim/reco: Tracks and hits can be coloured according to the corresponding simulated tracks. This is useful to see which extra hits/tracks are present in the reconstruction.

[†]Atlantis lists are groups of objects created by selecting objects either via the Pick or Rubber-band interactions.

[‡]Objects can be associated to other objects, for example: tracks are associated to hits in the inner detector.

3.8 Configuration

With all of these options, the user can customise what is displayed from an event to great extent. Once they are happy with the setup, an option exists to save the current settings into a configuration file, in xml format, which Atlantis can use to return the display to the same state next time Atlantis starts. To use this new configuration the default configuration (`config.xml`) can be overwritten, or it can superseded with a configuration (`.Atlantis-config.xml`) saved in the default home directory. Alternatively it can be saved as a separate file and loaded using the `-c` option on the command line. However there is not only one default configuration: Atlantis is used by many detector groups in the ATLAS control room (ACR), as shown in figure 3.4, so each of these groups now has its own configuration. For an example see section 4.4.

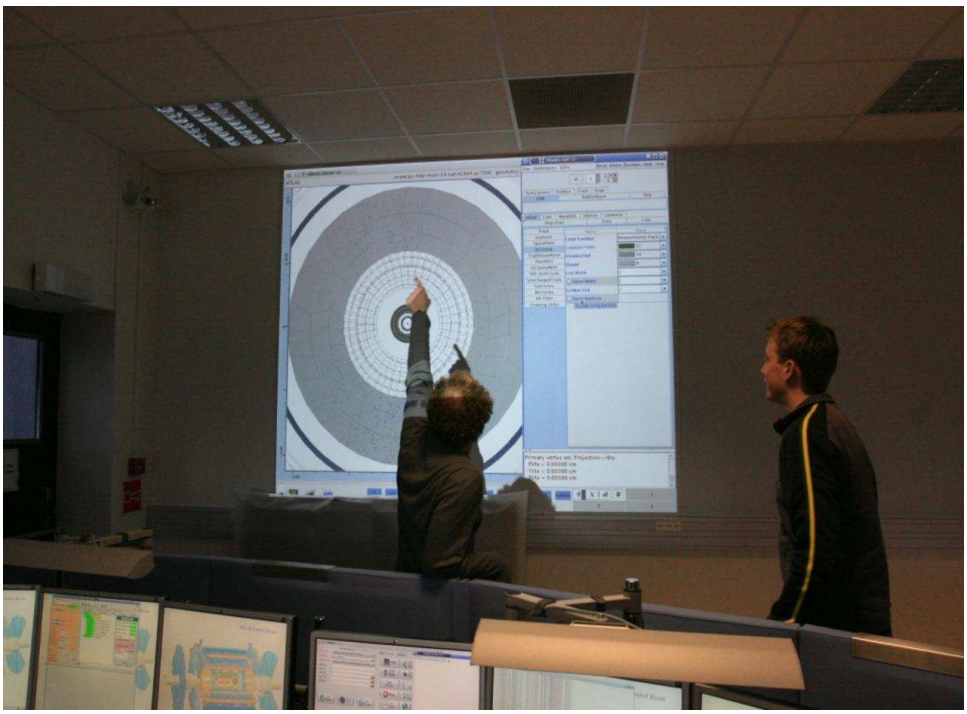

Figure 3.4: Atlantis being used in the ATLAS control room.

3.9 Development

As with all ATLAS tools the code for Atlantis is stored in an ATLAS SVN (Subversion) repository, previously CVS (Concurrent Versions System), which keeps a copy of all versions of the code. This allows all developers to modify the same version of the code, but before they can add in any changes they have to synchronise with the repository. This then updates their code with any changes other developers have added and then allows their code to be uploaded/committed into the repository. After doing this a tag is applied to give this version of the code its own specific identifier, which also allows users to see if their version of Atlantis is out of date compared with the latest in the repository. The best way for a normal user to obtain Atlantis is to go through the website (www.cern.ch/atlantis), which is updated regularly with a well tested version. During the three years of this project there have been nearly 600 updates (with contributions from 10 developers) to Atlantis, which shows that features and improvements are constantly being added and improved.

Chapter 4

Atlantis Development

4.1 Introduction

The previous chapter provides an overview of the basic principles behind the ATLAS event display, Atlantis. This chapter will give a more detailed explanation of work carried out on specific parts of the software, ranging from presentational issues and new displays to working with a detector group and in outreach.

4.2 Presentation

For graphics software, the appearance can be just as important as the functionality. As mentioned before Atlantis was originally based on DALI, and has kept much of the same style. By default Atlantis has several predetermined colour schemes, fully customisable in a colour editor. These were named “Default”, “Printer”, “Gray” and “B/W” and can be seen in figure 4.1, along with a DALI event display. Atlantis images can be seen on a screen, projector and printed on paper, all of which have different demands. To combat this the “Printer” colour map was designed with

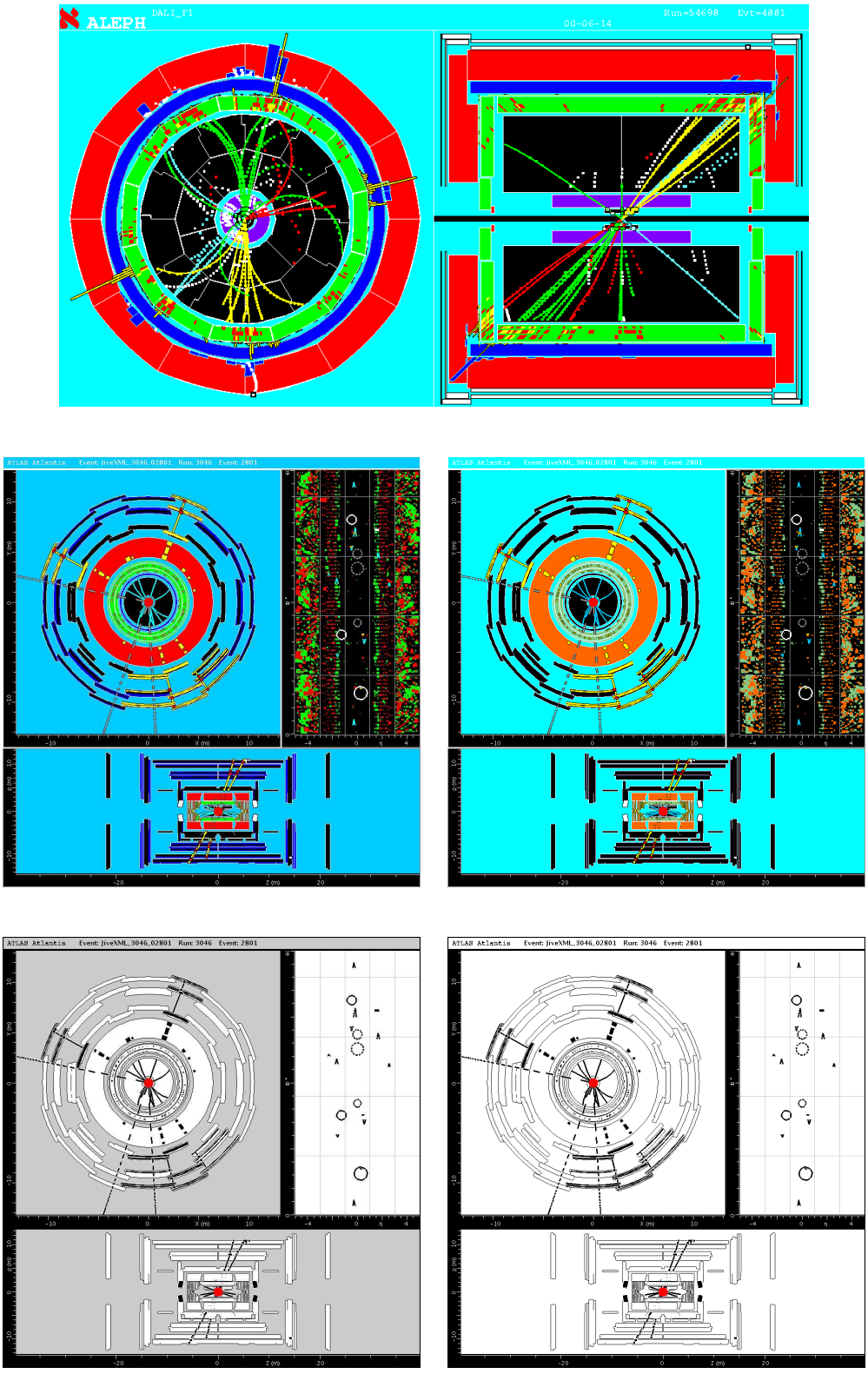

Figure 4.1: Top: DALI Higgs candidate event [29]. Below: Old Atlantis colour schemes showing a simulated Higgs event, clockwise from top left: Default, Printer, Gray and BW

colours that would print close to how they appear on screen, although not producing the nicest colour selection. The "Gray" and "B/W" colour schemes were optimised printed materials, especially for inclusion in papers.

It had been felt for some time that Atlantis should have improved style and extra motivation for this is provided by the fact that several ATLAS press release images were produced, such as that shown in figure 4.2, which had clearly been edited by hand from Atlantis images. Along with this, Atlantis is not the only ATLAS event display, so to remain competitive a whole range of presentational issues were looked into.

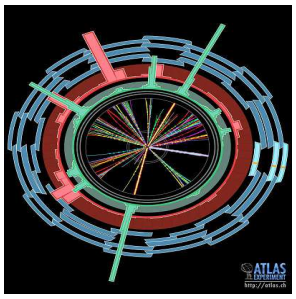

Figure 4.2: ATLAS PR image adapted from Atlantis [25].

Atlantis had already been used in ACR during the M3 commissioning run[†] and the decision was taken to improve the colour scheme before the subsequent M4 and M5 runs, based on the ATLAS press release image. To be able to achieve this the amount of colours used in Atlantis was increased from just 16, not all unique, to 28, where shading was used so that dark colours could be used for detectors and lighter for data objects. This new colour scheme ("M4M5") was a success, except for the problem that the projectors in the ACR made the image too dark. After more development a range of new schemes was created, figure 4.3, and has been well accepted, although the "M4M5" colour scheme is still the default in the ACR after the projectors were improved. With these changes the colour schemes also printed much better so the "Printer" colour map was replaced with "GrayDet" as it kept the

[†]M runs are milestone runs, when data from cosmic rays is used to rehearse running multiple sub-detectors at once.

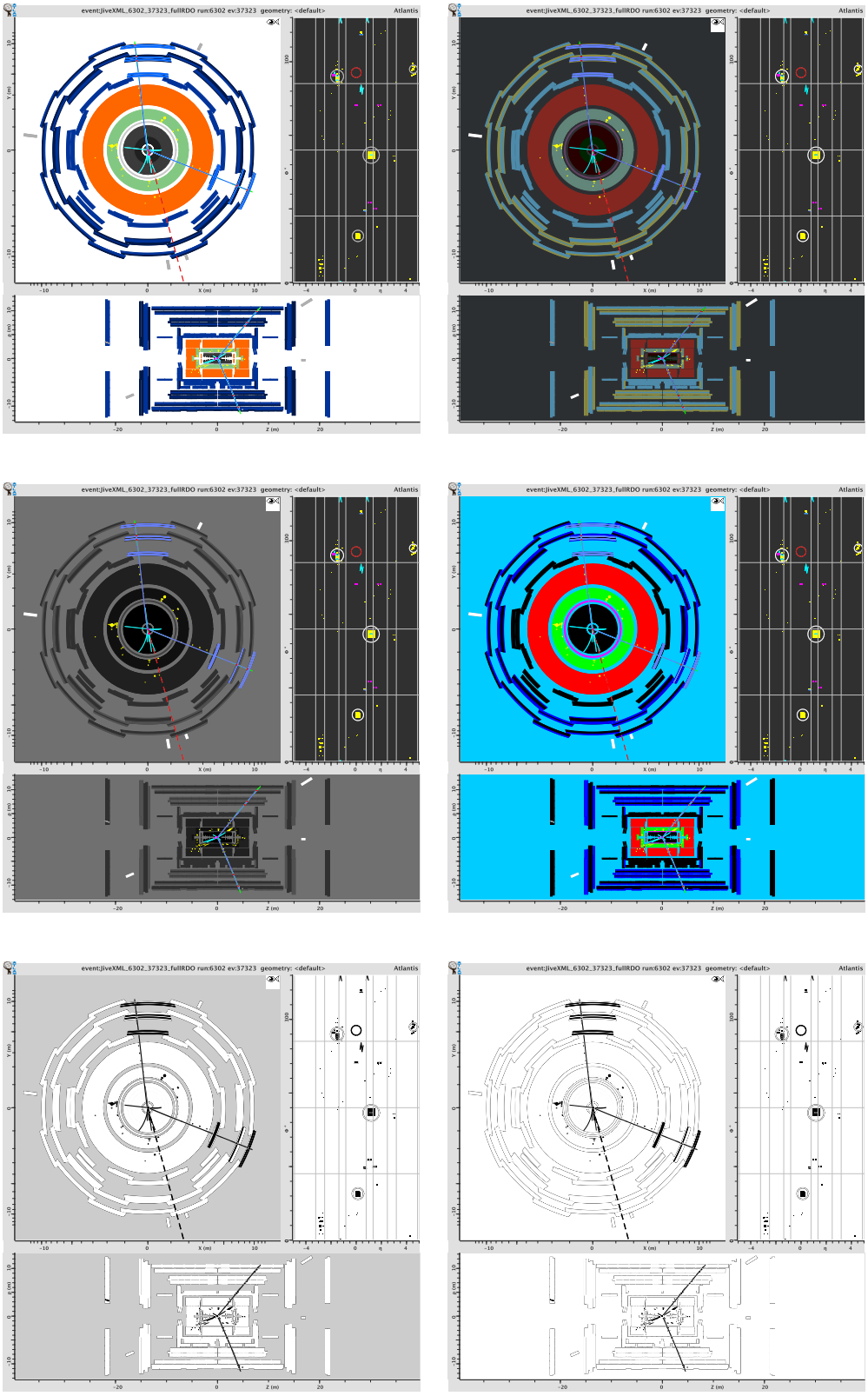

Figure 4.3: New colour schemes showing a simulated Higgs event (Default1 is shown previously in figure 3.2) in rows left to right from top:Default2, M4M5; GrayDet, Orig; Gray and BW.

default colours for objects on the display and just shaded the detectors in different shades of grey.

These new colour schemes were also improved to appear much sharper when printing `.png` images (in this document `.eps` are used). This is due to the addition of anti-aliasing, which smooths out lines and so improves the outline of objects[†]. However this has two drawbacks as it has a significant effect on the speed of drawing objects and also requires the user to have a more recent version of Java installed. The new Java requirement (version 1.5 or higher rather than the previous requirement of version 1.4) was not much of an issue, as most users already had a version beyond what is required, and it also enabled other improvements. However the user interaction with anti-aliasing was noticeably slower on a user level, e.g. when zooming. As a first step anti-aliasing was by default off, but was automatically used when outputting `.png` images (`.eps` images are drawn differently so already produces sharp images). This idea of switching anti-aliasing on and off was extended to occur when the user performs an interaction. So with anti-aliasing enabled the interaction functionality was unchanged during user operations and kept the same speed, but once the user released the mouse button, the image would refresh in higher quality.

The display now looked far improved and was well accepted within ATLAS. Due to this the start-up screen (the image displayed on screen while Atlantis loads) was updated with a new logo merging the ATLAS detector and the new display, as shown in figure 4.4. With these new colour schemes also a new option was added to show the detectors just in outline mode, which meant that the display became less cluttered, as shown in figure 4.5.

Further enhancements, such as faster rendering, sharper images and object transparency, have been requested by users. The best method of achieving these is to

[†]At the time of writing some parts in Atlantis were not correctly anti-aliased due to the methods used for drawing. Further improvements to use openGL have overtaken this improvement.

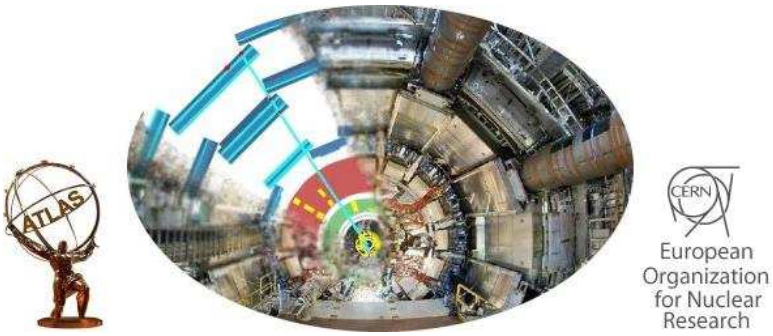

Figure 4.4: New start-up screen.

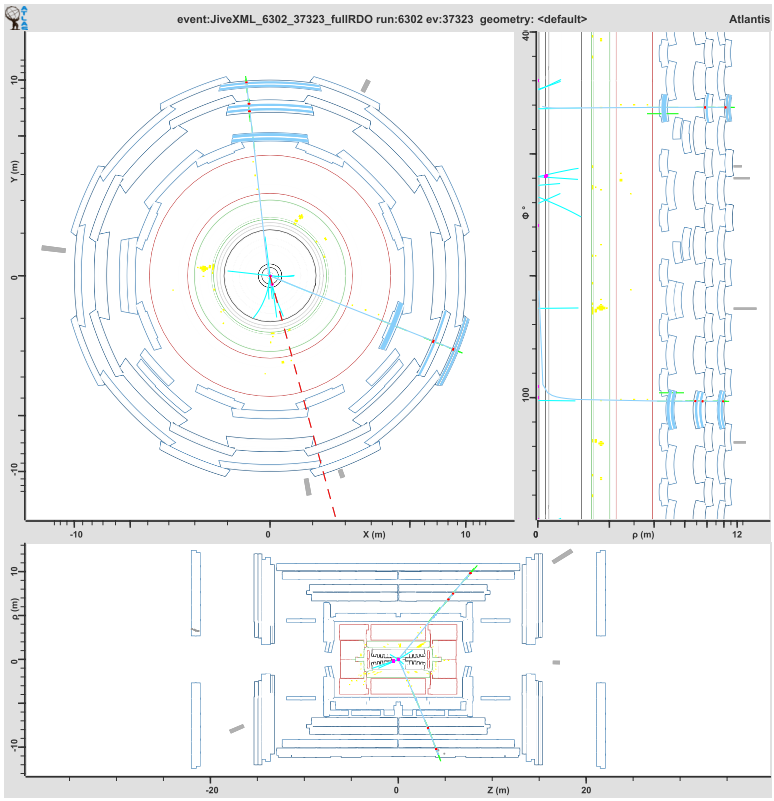

Figure 4.5: Option to make the detector only show an outline to simplify the image, so that objects are easier to identify (shown for a simulated Higgs event).

use openGL [30], rather than the native Java drawing. Preliminary trials have investigated the feasibility of using this within Atlantis, and have been successful. Following this further work was carried out specifically looking at the requests mentioned above, which progressed well to the point where other possibilities were also investigated, for example moving into 3D displays. Atlantis is predominately 2D as this is the simplest form of image for a user to process quickly, but in specific cases 3D images can be useful. The work focused on two areas: recreating one of the existing projections in openGL and creating a new specific 3D view. The most used projection is the `YX` projection, so this was chosen to be reproduced in openGL. The purpose of the special 3D view was to provide the user with information in a way not possible in 2D, rather than just creating a general 3D view of the whole detector. It was chosen to concentrate on displaying the constituents of a jet in 3D, as this is hard to see in the current 2D projections. After selecting a jet this special view appears showing cells and tracks around the selected jet, which is useful to study how the calorimeter cells have been combined into clusters before being combined into jets. These developments are shown in figure 4.6, where there are transparent jets drawn onto a new `YX` projection and also the 3D of view a jet with each cell coloured according to its associated cluster.

4.3 LegoPlot

The `LegoPlot` has historically been one of the main means of displaying events in hadronic scattering experiments and is one of the projections available within Atlantis. It displays the $\eta\phi$ plane with towers showing the E_{T} of the cells/objects. The `LegoPlot` was not needed for the e^+e^- collisions at ALEPH so DALI didn't have this functionality. Instead the `LegoPlot` has been adapted from an event display at DØ [31]. The other Atlantis projections were all developed to follow the DALI user functionality but the `LegoPlot` needed integrating into Atlantis from first principles.

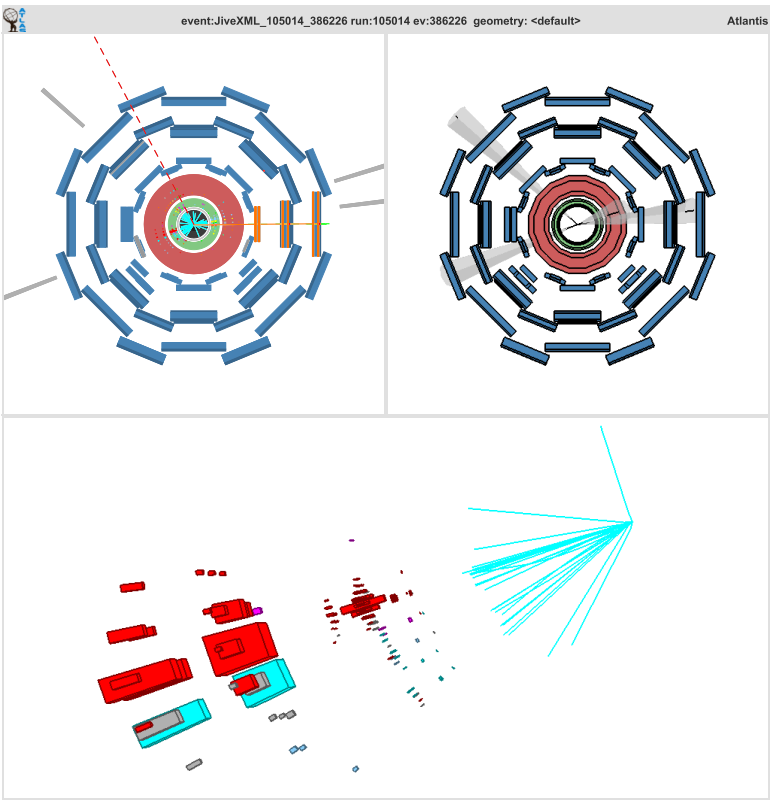

Figure 4.6: New views made possible by the addition of openGL: (top left) normal `YX` , (top right) openGL `YX` and (bottom) 3D jet view. The event shown is a di-jet event generated in the region: 140 GeV $< p_{\mathrm{T}} <$ 280 GeV.

For code simplification the single paint method was split into several classes (and methods): one for drawing, one for calculating the histograms and one base class for parameters and calling the drawing. This increased the ease of understanding the code along with removing sections repetitively used. Full support of the ZMR interaction could then be added, along with some specific "default" views and unzoom options. The vertical axis has to remain a constant height when looping through events, otherwise the base grid size altered depending on the transverse energy of the event. Methods were added therefore to scale the energy onto this constant vertical axis.

The plot is 3D and so has to be tilted to be shown on a 2D display, which leaves room for extra information to be displayed without overlapping the event data. For this three legends are added displaying information related to the plot: the value of the missing energy, colours of towers, the value of the highest tower and trigger information. The trigger information consists of: the three trigger level results; L1-SumEt and L1-Etmiss; and all the items that were passed in the event. These items are split into three separate lists so that they can be viewed individually. All these extra legends can be switched on or off, as can the plot itself if the legend information is deemed more useful, and are especially useful in the ACR to be able to quickly see what trigger items were passed in the event.

The current version of the `LegoPlot` is capable of displaying all calorimeter information (cells, trigger towers, jet elements and ROIs) and object locations: jets (drawn as rings with a customisable radius), missing energy (a dashed line in phi) and all AOD objects (drawn as outlined towers, although this can be customised so either/both cell/AOD towers can be solid/outlined). For any study involving the calorimeter this is now a very useful display, for both detector study along with physics analysis. For example, figure 4.7 is taken from a simulated Higgs decay to two muons and two electrons, via $H \rightarrow ZZ^*$. The underlying event provides some extra low E_{T} calorimeter deposits, but the two electron signals are very clear in the

normal view. As the muons leave very little energy in the calorimeter they are not visible, but the `LegoPlot` confirms that there are no other large calorimeter deposits in this event. On the detector level the trigger towers and jet elements also match up with the calorimeter cells, so confirming why the event passed the L1 trigger, see section 4.4. The result of the trigger can also be seen from the many items that were passed in this event. Also by colouring the trigger towers according to detector this confirms that the large showers are in the EM calorimeter, so consistent with being two electrons.

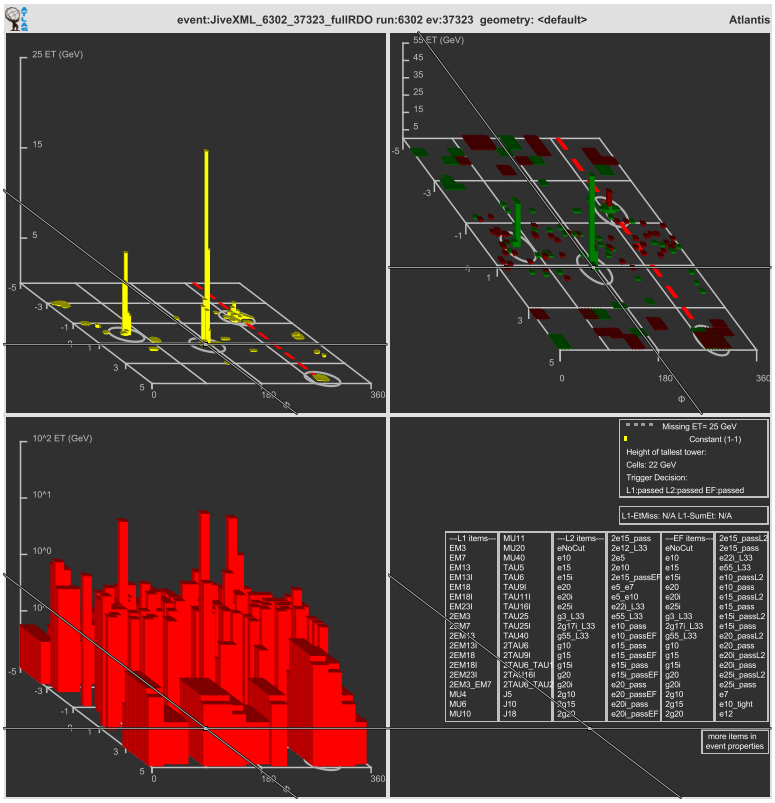

Figure 4.7: Image showing 4 versions of the `LegoPlot` for the same simulated Higgs event all displaying the SC interaction. Clockwise from top left: Normal view of cells, trigger towers coloured by EM(green)/hadronic(red) calorimeters with a different viewing angle, just the legend and finally jet elements displayed on a log scale.

4.4 L1calo

L1calo, the Level-1 calorimeter trigger, has already been outlined in section 2.9. As mentioned already it produces ROIs (split into three categories: EMTau, i.e. photon/electron/tau; Muon and Jet) and also has objects called trigger towers and jet elements, which are reduced granularity objects. Trigger towers are typically 0.1×0.1 in $\Delta\eta \times \Delta\phi$ and sum all the depths of each calorimeter. The jet elements are coarser still, typically 0.2×0.2, and sum together the EM and hadronic calorimeters. As these objects are calorimeter based they would normally overlap the calorimeter cells, so they are switched off in the default Atlantis display and have a different draw colour. The trigger towers also have an added functionality (like that present for calorimeter cells), in that once they are selected, using the pick interaction, an extra window like figure 4.8 appears. This window shows the Analogue-to-Digital Converter (ADC) counts, verses bunch crossing. These can be used to analyse the pulse time structure and so are important information to see, to check the timing of the detector. An extra feature of this plot is that the dots will turn red if the signal is saturated, which occurs for energy deposits around 250 GeV [27].

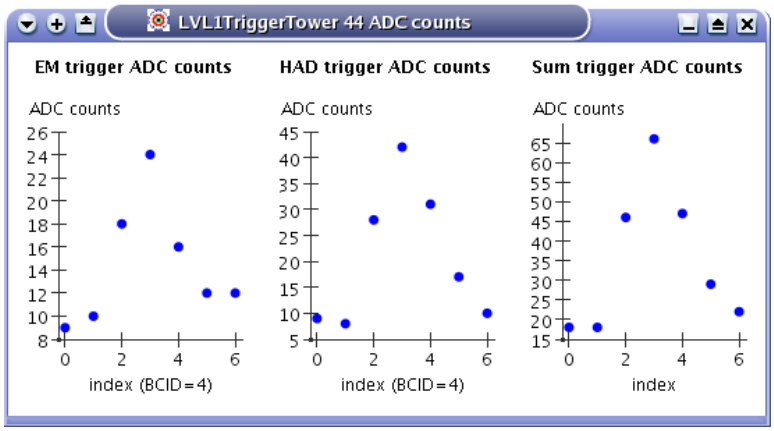

Figure 4.8: ADC count information obtained by using the pick interaction to select a trigger tower.

As mentioned already the `LegoPlot` is very useful for the L1calo group, so much

so that a button was added to take the display to a state with cells, trigger towers, jet elements and legends each shown in four separate windows. Figure 4.7 actually is based on the display created by this view, with some extra colouring and view options. The `LegoPlot` is also very useful for the L1calo specific configuration shown in figure 4.9, used in the ACR as referred to in section 3.8. This uses all the special features added to help the L1calo group:

- Comparisons of `LegoPlot`'s between cells, trigger towers and jet elements.
- Window titles, with extra mode detail to explain what is drawn.
- L1 only trigger items list.
- ROIs, correctly ordered to make EMTau/Muon appear on top of jet ROIs.
- Trigger towers in the `YX` view, so that they can be picked to see the ADC counts.
- Other views zoomed in to display just the calorimeter region.

4.5 End-caps

One of the features of Atlantis is its ability to use multiple projections to study the same part of the detector. On the `YX` projection the detector is split up so that the barrel region can be viewed, hiding the end-caps. The muon end-caps and the FCAL may then be viewed by selecting the appropriate detector from a view drop down menu. This functionality was missing for the calorimeter end-caps, so ten new views were required: 1 LAr presampler, 2 LAr inner wheels, 3 LAr outer wheels and 4 HEC layers. To make these easier to display a special option was added to the rubberband interaction which showed eight views of the layers where the inner wheels were placed inside the outer wheels. The length in the z coordinate of the first inner wheel overlaps with two layers of the outer wheel so it was decided to display it inside the outer layer it matches best. Also a tick box allowed the user to display the FCAL layers inside the relevant HEC layers.

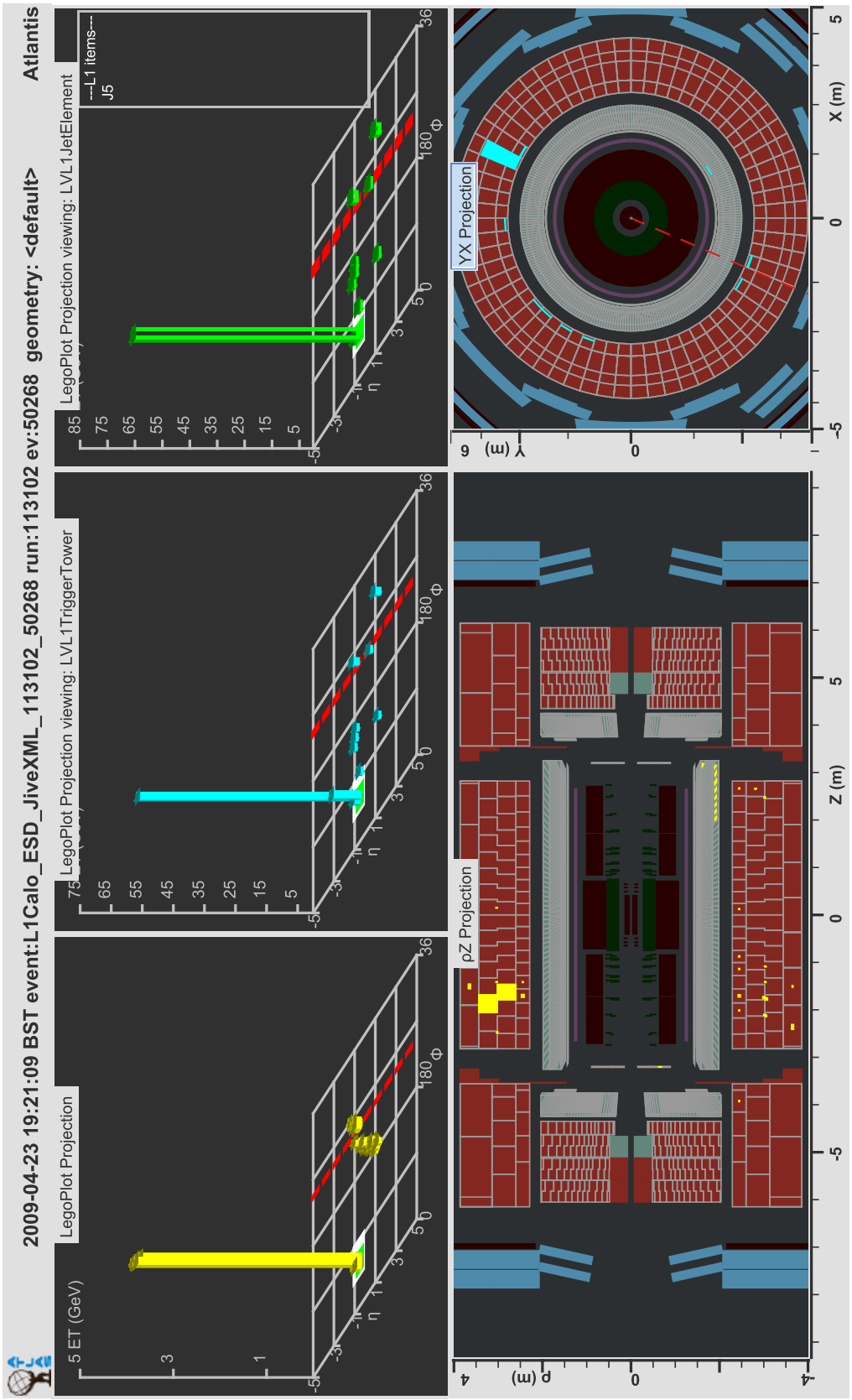

Figure 4.9: The ACR L1calo configuration, displaying a cosmic event from a calorimeter run.

Existing displays for the end-caps, made for use in Root (a data analysis framework [32]), already had features to sum up all the layers of the end-caps. Achieving the normal level of interaction in Atlantis with this feature was not possible. However with user feedback the layered end-caps were drawn with cells combined in z and also in ϕ if they overlapped the chosen grid size. This would indicate where the majority of the energy was deposited, but without the pick interaction, the actual value would be unknown. However by adapting the colour-by-energy function the energy of each colour could be displayed in a legend. The colours used were changed to match those found in Root, where the colour goes in steps from blue to red with increasing energy. Of course in the "Gray" mode this is adapted to use shades of grey (in the "BW" mode there is no shading so all cells always appear black). The shades were carefully chosen so that the steps between the colours were optimally visible, to help seeing the difference between cells similar in energy. The legend itself then can be selected from the `Preferences` menu and shows the energy threshold for each colour and maximum energy, as shown in figure 4.10.

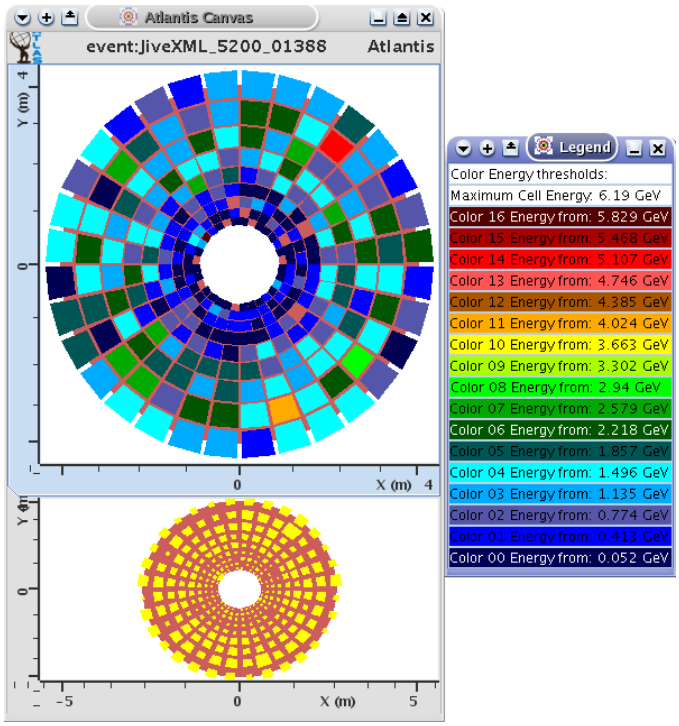

Figure 4.10: The colour-by-energy option makes it easier to find an energetic cell, here in the summed end-cap. The legend can also be used to see the scaling of the colours.

Through drop down menus the user can select the summed view and choose either a 0.1 or 0.2 binning in η and ϕ. Also available is an option to use a mixture of both 0.1 and 0.2 binning to replicate the actual geometry, where the cells become larger near the beam pipe. To get away from hard-coding the geometry with this split the user selects the point of the split binning so it can be changed for backward compatibility with older detector models, but by default it matches the actual detector layout. One remaining problem was that some cells seemed to appear outside the detector. This was because not all the cells at the edge of the detector are full cells so they had to be trimmed to their correct size.

To view all the summed end-caps or layers of end-caps the layout in Atlantis is automatically changed to best show the four or eight views, respectively. The best view of the eight views was when the canvas was split into nine windows, so a further improvement to the rubberband functionality was to add a ρZ view into the free window. This allows the user to see which of the end-caps they have selected more easily. The value of the zoom for this ρZ window had to be hard-coded as the z position can not be retrieved from the YX window coordinates. These optimised views of the end-caps can be seen in the figures 4.11 and 4.12.

To help the user go back to the previous view, an unzoom option was added to the right click menu, which saves the user from having to perform a full reset. This expanded the existing rubberband unzoom feature, to also unzoom multiple windows as well as reverting any layout changes. Instead of unzooming many windows each individual window can return directly to the first step by using the "unzoom full" function, also located on the right click menu. These features, originally designed for just the end-caps, were expanded to allow other parts of the code to have the same functionality, including adding the code to the ZMR interaction.

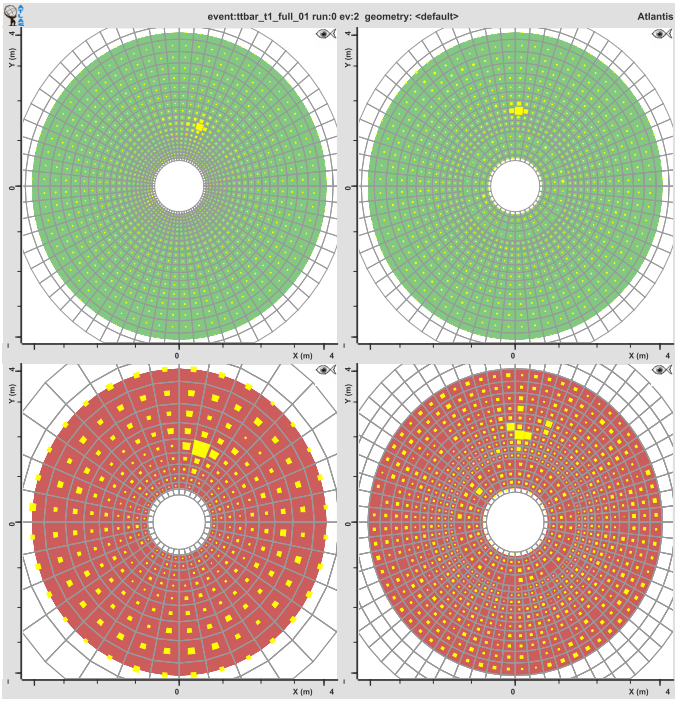

Figure 4.11: Image of the summed view of the end-caps (with cell outlines), showing (left) the $-z$ End-cap with default binning and (right) the $+z$ End-cap with split binning, for (above) the LAr and (below) the HEC.

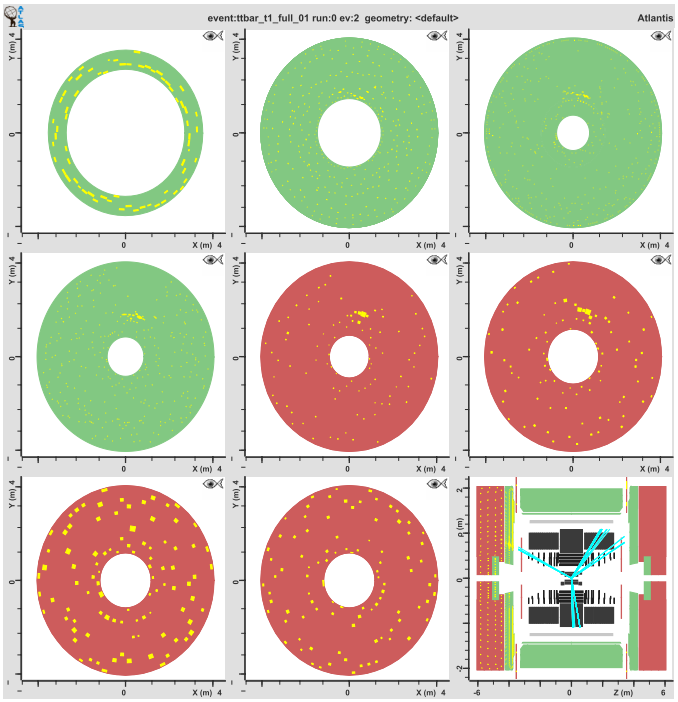

Figure 4.12: Image of the individual layers in the end-caps, showing from left to right row by row: LAr end-cap Presampler, LAr End-cap layers 1, 2 and 3, HEC layers 1, 2, 3 and 4 and ρZ view showing calorimeter data from the selected End-cap.

4.6 MINERVA

Atlantis has been designed for physicists to enable them to have online and offline displays of any chosen event and to help understand confusing events. Being able to visualise what happens in a collision is also useful to help the general public understand the ATLAS experiment. Images from Atlantis are used on logos for CERN merchandise, for example that shown in figure 4.2, and also were widely used on newspaper front pages on the 10th of September for the LHC switch on, see an example in figure 4.13.

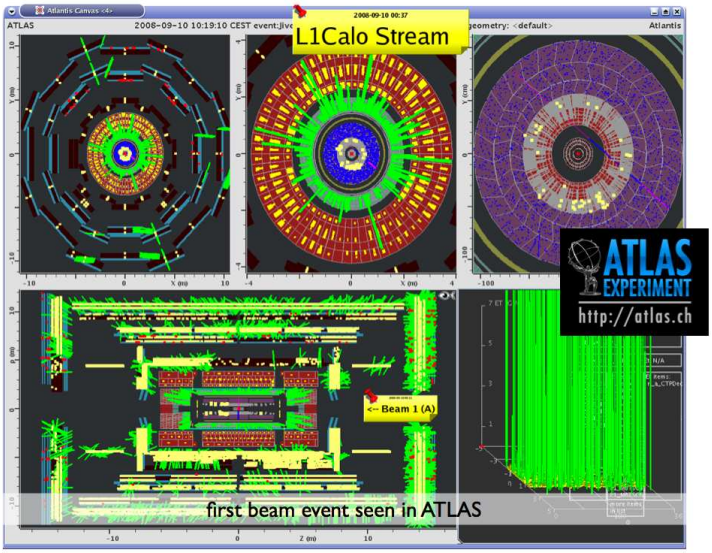

Figure 4.13: Image of a beam splash released to the media, from Atlantis on the 10th of September.

The ATLAS collaboration has agreed that some of the ATLAS data can be made available to the general public, with the aim of promoting particle physics to students of all ages. Atlantis is a perfect tool for giving students a way of understanding the data, for example at specially organised Masterclass events operating at universities around the world. These consist of students visiting an institute for a day, seeing some talks on particle physics (usually given by current PhD students), have question and answer sessions, tours of either local experimental equipment or video tours

of ATLAS and finally a hands-on session. The hands-on session has previously been based on LEP event scanning, but with the LHC coming online this needed updating to LHC events. Originally a Greek group decided to use the Atlantis code base to produce their own event scanning software, Hypatia [33]. Unfortunately this software changed much of the normal Atlantis display, e.g. splitting up the GUI, which made it impossible to include the Hypatia code into Atlantis. This meant that any Atlantis updates had do be re-done by the Greek group, leading to several difficulties understanding problems in Hypatia.

In the UK the largest particle physics Masterclass is based at RAL, where hundreds of students visit each spring. The decision was made to use Atlantis to scan through specially selected simulated ATLAS events and Birmingham, which also runs its own Masterclass, became involved in the development of a special configuration file. The event sample for the students included:

- W decays to $e\nu$ and $\mu\nu$
- Z decays to ee and $\mu\mu$
- Background events from di-jet events.

The aim was for features in these events to be easily recognised by a student. A preliminary scan through the events showed that using histograms to show cell energies was important for picking out electron events and rejecting background events. The easiest displays to explain to people are the `YX` and $\boldsymbol{\rho}$`Z` projections as they represent side-on views of the detector. As we had found histograms useful for cells we also chose the `LegoPlot` , fixing the height of the axis so the more energetic events stand out compared with the normal histograms which are scaled per event.

From the first trials of the software it was a big success, with students being able to get to a point where they could study on their own very quickly. Some even managed to spot a Higgs event slipped into one sample, for which they were awarded prizes. Further improvements were needed as muons were often missed as

were events with particles going into the end-cap.

To make it easier to describe to the collaboration, add as one of the Atlantis specific configurations and to create webpages the project was given a name: MINERVA, Masterclass IN Event Recognition Visualised in Atlantis. New events were produced along with better sorting inside groups, to have the easier events nearer the start and progressively adding difficulty through the events. These were then packaged up into different download files, to help teachers with limited storage facilities. On the Atlantis side, figure 4.14 shows the current default view of Minerva, with the following differences to the normal Atlantis configuration:

- `YX` and ρ`Z` projections with histograms to easily see calorimeter deposits.
- `YX` projection has an η cut applied to make it only show objects in the barrel.
- `LegoPlot` with fixed E_{T} axis height to be able to see the size of the deposit.
- All muon objects coloured the same colour, with the addition of tracks to make them more apparent and show that they go through the whole detector.
- Missing energy line thickness alters depending on the size of the missing energy (its value is displayed on the `LegoPlot` legend).
- Simplified GUI hiding parts not needed by the users, achieved by using a setting ("userlevel") already existing in the configuration file.
- Altered canvas title, the run number is hidden to avoid students realising that the events can be recognised by this.
- Simplified output, when an object is picked only selected information is needed in the GUI. Other data not from pick just passes to the terminal output.

These options are all adapted in Atlantis through hidden flags in the configuration file. This configuration was added as one of the Atlantis custom configurations, allowing the first webstart version to be created and added to the Atlantis website. Some of the features, however, are available in all versions of Atlantis: "mass calculation", "about" window and help. The "about" window and online help system both

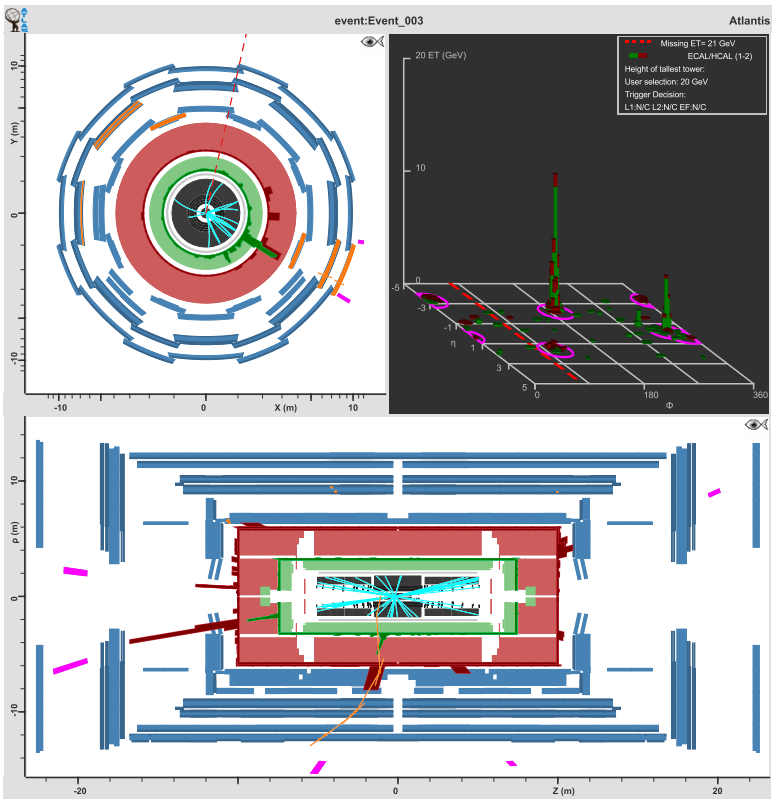

Figure 4.14: Minerva display of a background event.

have updated details for Minerva. The "mass calculation" tool is a simplification of existing features. When looking at the event it can be useful to sum the energy of tracks to find the mass that they correspond to. This can be done by creating a new "list" in Atlantis, then using pick with the "add to list" modifier key and finally using the "summarise" option on this list (done by selecting the list in the list manager window). Instead of this complicated procedure, a "mass calculation" modifier key (`M`) was added along with a dedicated list. When this key is used, with the pick interaction, objects are automatically added to the "mass calculation list" with a summary of the calculated mass outputted automatically to the GUI.

So far the Minerva software was designed just for use in Masterclass events; successfully used in 2008 and 2009 at RAL and Birmingham and also elsewhere including 6 Masterclasses in the US. This has been a huge success with a lot of positive feedback for such a young project. The current setup is approaching a version which will be ready to take real events possibly as early as spring next year. Expansion of the project will also take it into university laboratories, school classrooms and onto the web. This will require a different introduction to the software, as such applications will lack the normal talks given at a Masterclass event. This resulted in the creation of a website[†] containing some introductory information, the ability to launch Minerva and a method to feedback to the user their success at finding events. The website homepage has two main links: one for leaders of Masterclass events, taking them to the twiki as used previously, and another to start using Minerva. The home page layout is shown in figure 4.15, displaying prominently these main link buttons, but there are also support, news and contact links and some introductory translations.

When the "Start Minerva" button is pressed a few introductory slides are shown. These are limited so that users won't lose interest before the software starts. Once these are read Minerva is downloaded via webstart. At a Masterclass event, experts

[†]www.cern.ch/atlas-minerva.

Figure 4.15: Home page of the Minerva project.

are on hand to help guide students through the exercise. To replace this, five tutorial events are loaded first and the user can enter their event choices into the website, which will tell them how well they did. This means that the user should understand the physics and software to a reasonable level before scanning a full set of twenty events. The question page code can also be reused for the full set of events, which is helpful even at Masterclasses as marking hundreds of student answers is a time consuming task. At present this is the limit of the website, but extensions are possible to add a Higgs search and to output more information to the user, e.g. comparison of the real W/Z ratio with what they find, investigation of composite masses when looking at Z^* and Z events, certificate to say they completed the task, etc.

4.7 Other Contributions

The topics described above have been some of the more substantial, or more noticeable, contributions to Atlantis. However, listed in this section are some of the additional contributions by the author.

4.7.1 MBTS

The MBTS, as mentioned in sec 2.7, was previously not included in the basic Atlantis geometry, or datatypes. Outputting the geometry information required working on the JiveXML side of the project. Once this geometry data was in a usable format, Atlantis was required to display MBTS information in specific views like those for the end-cap layers. The finished display of the MBTS can be seen in figure 4.16, with views in ρZ and each end in YX . The hits have been coloured blue to highlight them on the ρZ projection as this view only adds information on their position in the detector, whereas they are easy to understand from the YX projection. As in YX the cells line up over each other, when the cell is picked both the +z and -z cell energies are outputted. These views were demonstrated to some MBTS experts, who were happy with the general features.

4.7.2 TRT

As shown in figure 4.17 the TRT, outlined in section 2.6, consists of drift tubes and as the track traverses it will cause ionisation in each chamber it passes through. In Atlantis these "hits" are represented by circles with a radius scaled to the drift radius. However, when demonstrating Atlantis at an Inner Detector specific tutorial it was shown that extra details from the tracking algorithms were present in a TRT event display, which were then included into Atlantis.

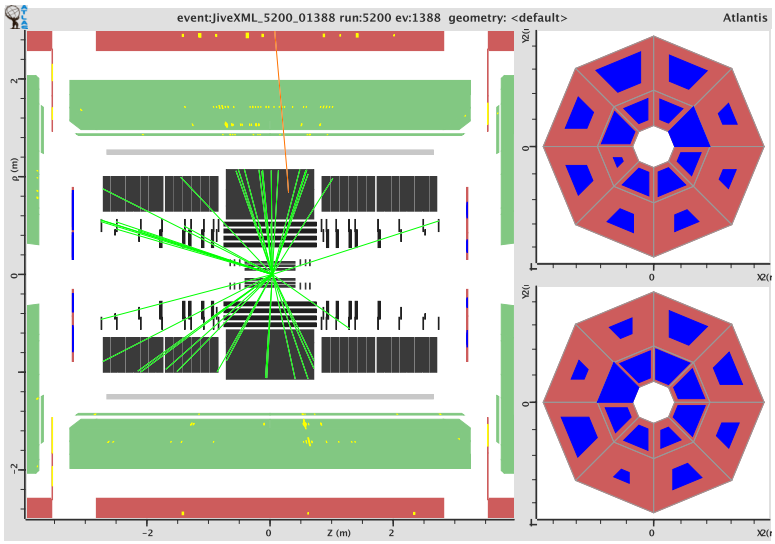

Figure 4.16: The MBTS in Atlantis, see text for details.

Firstly as the direction of each drift is known, an arrow was added to show this direction. Due to their size the corresponding drift circles appear as lines until the user has zoomed in far enough. There are many TRT hits, so rather than wasting valuable drawing time the hits were changed to be drawn as lines until the user has zoomed into a level where the circles are actually visible. Then the circle appears, along with the arrow if the hit is associated to a track. This performance improvement could be further extended to any other shapes that could be drawn with less points.

Along with adding the arrow, colouring options were also added. Firstly colouring by drift direction, which meant it was easier to look at the trends of the drift directions with respect to a track. Secondly colouring was added for outlier hits, which are hits that are associated to a track, but don't match well. Figure 4.18 illustrates the developments showing outlier hits linked to a track that ends before the TRT, an outlier on a track and finally drifts in different directions along two nearby tracks.

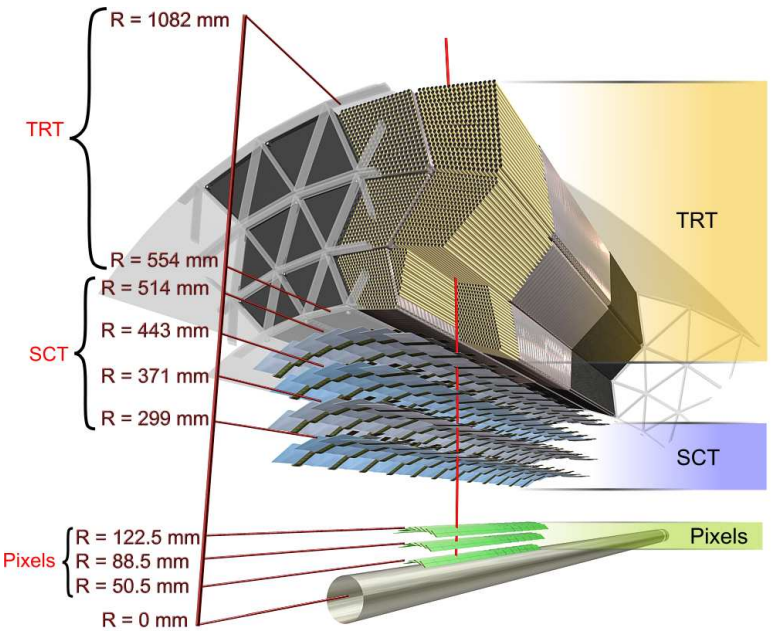

Figure 4.17: Image of a track passing through the Inner Detector [1].

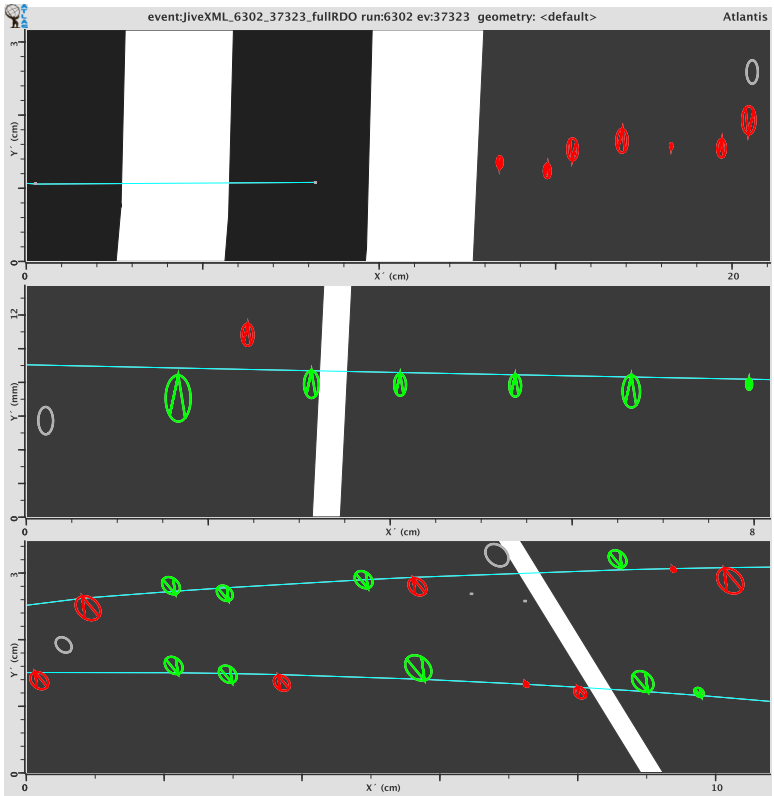

Figure 4.18: Inner Detector TRT hits. Top and Middle: colour by outlier. Bottom: colour by drift direction. See text for more explanation.

4.7.3 User help tools

Atlantis has an in-built help system which allows the user to see documentation, which the developer is in charge of maintaining, on any object by right clicking. Added to this there are several tools to help the user understand what is being displayed. The most useful of these is the event properties panel, which gives a listing of all the objects in the event. To improve this many other pieces of information were added:

- Trigger results, L1 sums as on `LegoPlot`
- all L1, L2 and EF trigger items which were passed, and their prescales
- special trigger item list, filled from item names in a text file
- additional trigger info (trigger streams and hex patterns for experts)
- MBTS cell hits

For new users to Atlantis, just understanding what is drawn can be a daunting task. To help with understanding the geometry of each display, a pop-up window was added to output the current pointer position (selected by using `O` with right click). In addition the colours of each object can be understood by introducing a help window, as shown in figure 4.19, which, as well as showing the current object colour in the selected window, also shows the current collection of each object being displayed.

4.7.4 Composite particles

Composite particles are another set of particles produced in the reconstruction software, created from combining other particles e.g. combining leptons to form a Z. Addition of this data type in Atlantis led to the by-product that other new data types not previously displayed can also be added, as this datatype only has simple data tags (energy, η, ϕ, particle type, etc.). Using the particle type information the

Figure 4.19: Window to explain current colours and collections in use in Atlantis.

object can be given the usual colouring, i.e. if a composite particle is an electron then it would be coloured like a normal AOD electron. To distinguish these particles they are drawn as: histograms located outside normal AOD objects, squares on the $\phi\eta$ projection and as towers on the `LegoPlot` (even if they represent a jet).

One of the ways this datatype was used was to display "Eventview" particles directly from an ntuple. "Eventview" was a proposed method to create composite particles and aid in selecting the correct reconstructed objects, in cases where the same detector deposits are classed as several reconstructed objects. This is best explained via figure 4.20, showing "Eventview" particles and normal reconstructed objects, with five particles highlighted. Table 4.1 then shows the objects "Eventview" has chosen as the best match (out of the reconstructed objects) to the detector deposits for the five particles highlighted, including a composite particle combined from other objects in the event.

Table 4.1: Comparison between "Eventview" reconstruction and all reconstructed objects.

Label	Default Athena	Eventview
1	electron and jet	electron
2	photon and jet	jet
3	electron and jet	B jet
4	none	composite particle
5	B jet and jet	jet

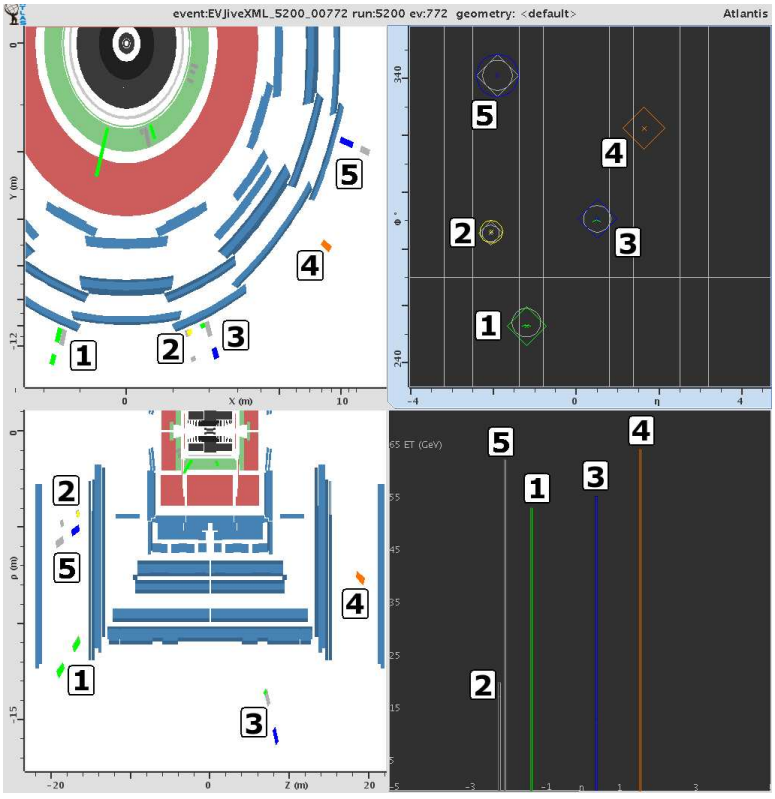

Figure 4.20: Composite particles in Atlantis, see text for details.

Chapter 5

Direct Photons

5.1 Introduction

"Direct", or "prompt", photons are so named as the photon originates directly from the hard proton-proton interaction, distinct from photons appearing later in a decay chain. They have been studied previously in hadronic collisions at fixed target experiments [34–36], as well as in colliders [37–44], and have several uses in detector calibration and physics analysis. This chapter will give an outline of the theory describing collider physics kinematics and direct photon production dynamics along with a motivation for accurate direct photon measurements at ATLAS.

5.2 Collider Physics

In describing collider kinematics there are some important quantities that need to be defined. The proton-proton centre of mass energy, denoted $\sqrt{s}$[†], is not the energy

[†]For two relativistic particles colliding with 3-momentum p: $s = 4p^2$, therefore the Mandelstam variable s is the square of the centre of mass energy of the particles.

of the fundamental interaction to study, which will be between the partons inside the proton. The energy carried by these is reduced relative to the proton energy by a factor of the Bjorken scaling variable x. This is defined as the fraction of the proton momentum carried by a parton in a Lorentz frame in which the proton momentum tends to infinity. For the two incoming protons the colliding partons will be carrying x_1 and x_2, as shown in figure 5.1, creating a partonic collision with energy: $\sqrt{\hat{s}} = \sqrt{x_1 x_2 s}$.

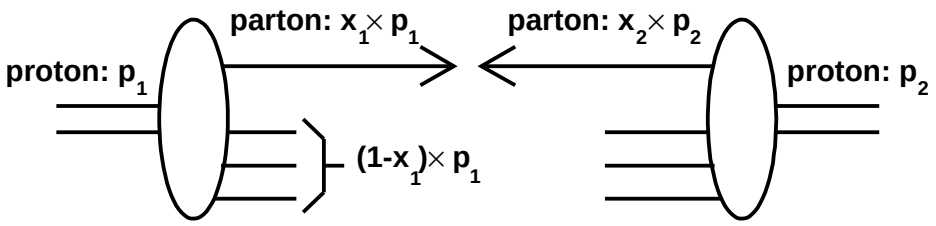

Figure 5.1: Explanation of the kinematics of a proton proton collision.

Originally the partons inside the proton were thought to be just three quarks (two up and one down). These quarks, known as valence quarks, provide the proton with its charge. However deep inelastic scattering experiments, where leptons are used to probe inside the proton, have shown that protons contain other partons. Firstly there are other quarks, which form quark-antiquark pairs and combined with the valence quarks they provide $\sim 50\%$ of the proton's momentum. The remainder of the proton's momentum is carried by gluons, which hold the proton together. Figure 5.2 shows the parton distributions, i.e. the momentum weighted probability of finding a parton, as a function of x when the proton is probed at a scale of $Q^2 = 100$ GeV^2, where Q^2 is the momentum transfer. This shows that at high x there are twice as many up quarks compared to down quarks (from the three valence quarks), but any light quark is equally likely to be found at low values of x. Also shown is that the gluon is dominant over most of the x region, until very high x values.

When two of these partons collide in a $2 \rightarrow 2$ collision, two incoming partons

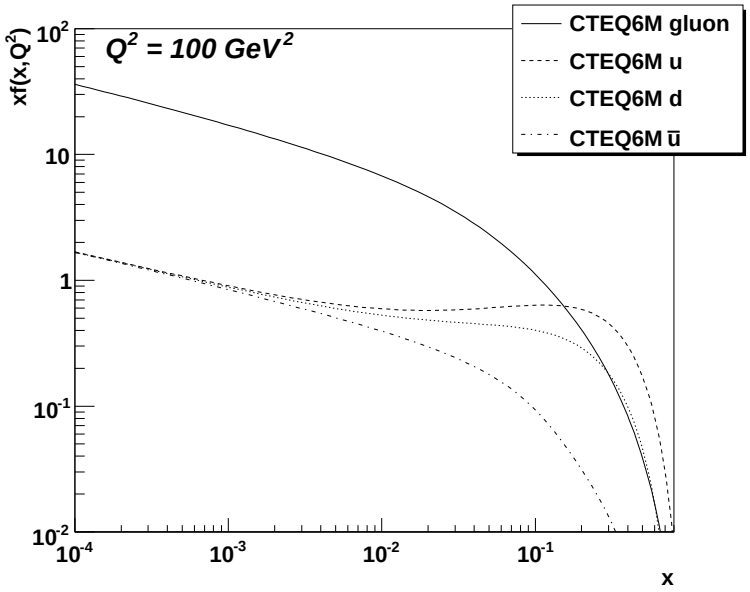

Figure 5.2: CTEQ6M [45] x distributions for a gluon, up quark (u), down quark (d) and anti-up quark ($\bar{u}$), produced with [46].

producing two final state particles, the outgoing particles will be back-to-back in the parton-parton centre of mass frame. However, as x_1 does not generally equal x_2 this is no longer the case in the lab frame. If they were back to back in the lab frame, then each outgoing particle would have a 3-momentum $p = \sqrt{s}/2$, so a variable x_T can be defined as:

$$x_T = \frac{2p_{\mathrm{T}}}{\sqrt{s}} \tag{5.1}$$

such that in the back to back case, at $\eta = 0$ in the lab frame, $x_T = x$. When one of the incoming partons has a larger momentum than the other, then both the outgoing partons will be boosted in the direction of the incoming parton with larger momentum, as demonstrated in figure 5.3[†]. This feature of the event can also be used to find the minimum x detectable, for a given η and p_{T}, by the formula (derived in appendix A):

$$x_{min} = \frac{x_T e^{-\eta}}{2 - x_T e^{\eta}} \tag{5.2}$$

[†]Although in general $\eta_3 \neq \eta_4$, where 3 and 4 are the outgoing particles.

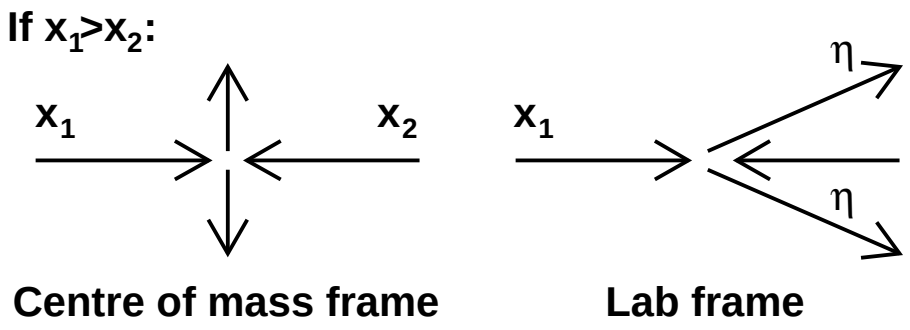

Figure 5.3: A $2 \rightarrow 2$ process with outgoing partons at $\eta = 0$ in the centre of mass frame transformed to the lab frame in the case where $x_1 > x_2$.

As described in section 2.6, the ATLAS Inner Detector, which is needed for photon measurements to distinguish them from electrons, only extends up to $|\eta| < 2.5$. To maintain an acceptable trigger rate photons are accepted with $p_{\mathrm{T}} > 10$ GeV, which can be combined with the η requirement to calculate values of x_{min}, as shown in table 5.1.

Table 5.1: Calculations of x_{min} for different values of p_{T} and $\sqrt{s}$.

p_{T}(GeV)	x_{min} for $\sqrt{s} = 14$ TeV	x_{min} for $\sqrt{s} = 10$ TeV
10	6×10^{-5}	8×10^{-5}
20	1×10^{-4}	2×10^{-4}
50	3×10^{-4}	4×10^{-4}
100	6×10^{-4}	9×10^{-4}
250	2×10^{-3}	3×10^{-3}
500	5×10^{-3}	1×10^{-2}

5.3 Direct Photons

As stated above the direct photons come directly from the hard interaction and at leading order (LO), order ($\alpha\alpha_s$), there are two sets of diagram. These are the Compton process ($qg \rightarrow q\gamma$) and the annihilation process ($q\bar{q} \rightarrow g\gamma$), as shown in figure 5.4. In terms of detector observables these will ideally be seen as one isolated photon and one jet, which will be back to back in the azimuthal direction of the detector. The jet will be formed from the outgoing q/g and the isolation for the photon means that there should be no large energy deposits near to the photon, a feature which can be used in selecting the events, see section 7.6.4.

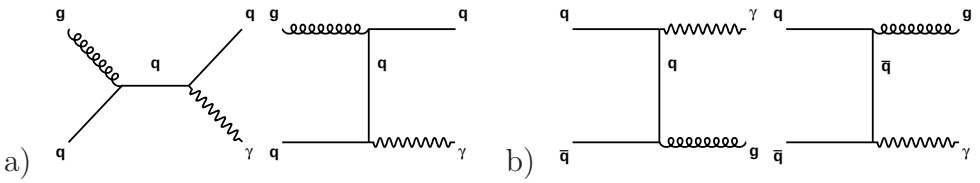

Figure 5.4: Feynman diagrams of the a) Compton and b) annihilation processes.

Beyond the order ($\alpha\alpha_s$) diagrams are the Bremsstrahlung process in di-jet events, arising from Initial/Final State hard QED Radiation (I/FSR) from a quark, and the dual gluon process, see figure 5.5. The Bremsstrahlung process is of order ($\alpha\alpha_s^2$) and the outgoing photon is generally not well isolated. The LO dual gluon process is higher order again ($\alpha\alpha_s^3$) but this may still be an important process as the gluon dominates in the proton parton densities at low values of x, see figure 5.2, increasing the cross-section of this process for low x values.

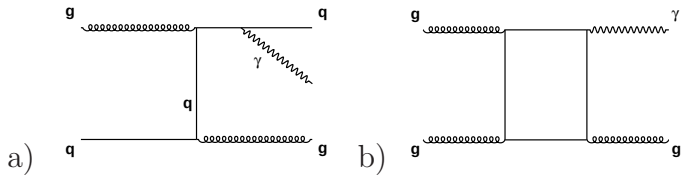

Figure 5.5: Feynman diagrams of a) the Bremsstrahlung and b) the dual gluon processes.

The cross-section for direct photons is then calculated as a sum of the LO direct photon processes, Compton and annihilation (neglecting the dual gluon for the moment) and the Bremsstrahlung processes:

$$\frac{d\sigma}{dp_{\mathrm{T}}d\eta} = \frac{d\sigma^{dir}}{dp_{\mathrm{T}}d\eta} + \frac{d\sigma^{brem}}{dp_{\mathrm{T}}d\eta} \tag{5.3}$$

The lowest order forms of these separate parts are then shown in equations 5.4 and 5.5, based on the formulae given in [47].

$$\frac{d\sigma^{dir}}{dp_{\mathrm{T}}d\eta} \propto \sum_{i,j=q,g} \int dx_1 dx_2 F_i(x_1, M) F_j(x_2, M) \alpha_s(\mu) \alpha \frac{d\hat{\sigma}_{i,j}}{dp_{\mathrm{T}}d\eta} \tag{5.4}$$

$$\frac{d\sigma^{brem}}{dp_{\mathrm{T}}d\eta} \propto \sum_{i,j,k=q,g} \int dx_1 dx_2 F_i(x_1, M) F_j(x_2, M) D_{\gamma/k}(z, M_F) \alpha_s^2(\mu) \alpha \frac{d\hat{\sigma}^k_{i,j}}{dp_{\mathrm{T}}d\eta} \tag{5.5}$$

These are summed over all combinations of colliding gluons and quarks (denoted by indices i and j). The term $\frac{d\hat{\sigma}_{i,j}}{dp_{\mathrm{T}}d\eta}$ represents the partonic cross-section, which is the cross-section of the hard scatter process. There are also parton densities, $F(x, M)$, which give the number of quarks and gluons in the proton at a scale, M. This scale is the factorisation scale to control collinear singularities, i.e. singularities arising from particles being radiated with low p_{T}, in the initial state. There is also a renormalisation scale (μ), due to the running of the coupling α_s. These scales are required because the cross-section is calculated at a fixed order and normally both of these scales are chosen to equal to the photon p_{T}. In the Bremsstrahlung process fragmentation functions, $D(z, M_F)$, are needed to describe the probability for a parton (denoted by the index k) to fragment into a system including the radiated photon. The value z relates to the ratio of the magnitude of the longitudinal momentum of the produced particle to that of the parton, i.e. in this case $z = p_\gamma/p_k$, whereas M_F is the final state factorisation (or fragmentation) scale and again is set to equal to the photon p_{T}.

5.3.1 Phase space

As the direct photon p_{T} increases the η distribution narrows and a larger fraction of events are observable in the detector. Figure 5.6 shows this expected kinematic coverage for the entire phase space acceptance for the LHC s compared to that of the range from HERA and fixed target experiments. The lower limit in Q^2 corresponds to the trigger requirement $p_{\mathrm{T}} > 10$ GeV. This shows that the majority of the area of sensitivity has not been observed before at HERA and in the low x region, $x < 10^{-5}$, this is the first experiment to study at scales where perturbative QCD is applicable. Also shown is the phase space acceptance for direct photons, which is mostly limited in x by the η coverage of the detector. This is still a new region of phase space, which has a slight shift to higher x values when running at 10 TeV rather than 14 TeV.

5.4 Intrinsic k_{T}

Previous measurements of the direct photon cross-section at the Tevatron and elsewhere have shown a discrepancy at low p_{T} when compared to the theoretical next-to-leading order (NLO) cross-section, as illustrated in figure 5.7. One explanation is the presence of recoil corrections arising from soft gluon radiation, taking the form of an intrinsic transverse momentum, k_{T}, of the incoming partons [48]. This would account for any problems arising from poorly understood parton evolution at low x and such an intrinsic k_{T} model does seem to correct the NLO prediction, as shown in figure 5.7. At the LHC photons with a $p_{\mathrm{T}}(\gamma) \gtrsim 60$ GeV are not expected to be affected by this k_{T} effect. Only data taken by the experiment can confirm the size of this effect at the LHC, so the aim is to measure the cross-section over as wide a range of phase space as possible, especially at low p_{T}.

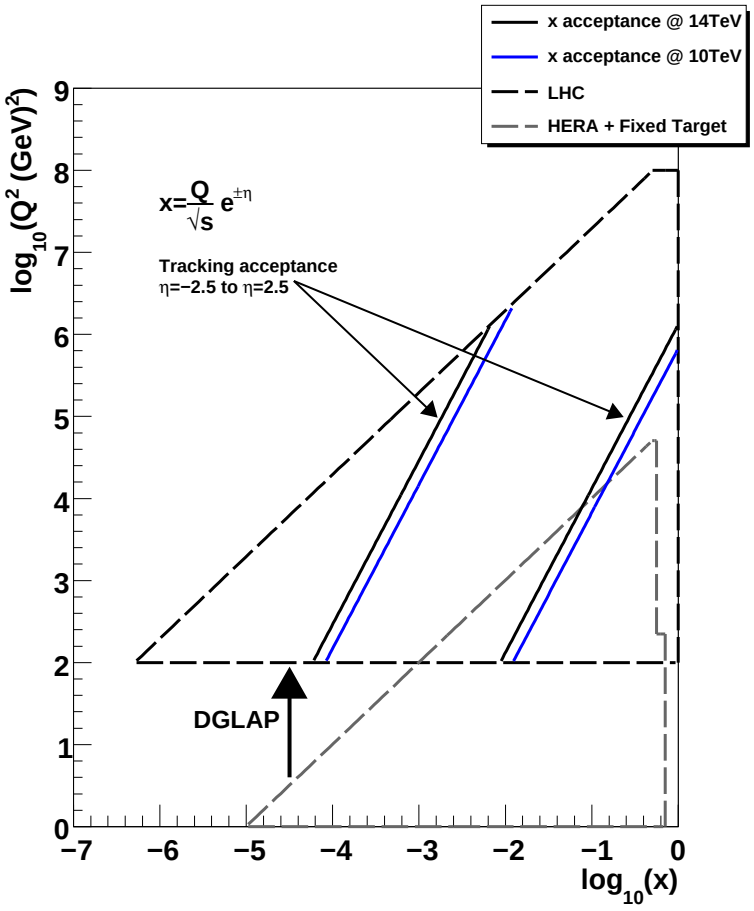

Figure 5.6: Phase space acceptance, $\log_{10}(Q^2)$ versus $\log_{10}(x)$, for both the LHC and HERA with fixed target experiments. The dashed line represents the phase space available from the LHC s, with the solid lines showing the x obtainable for a given Q^2 and η.

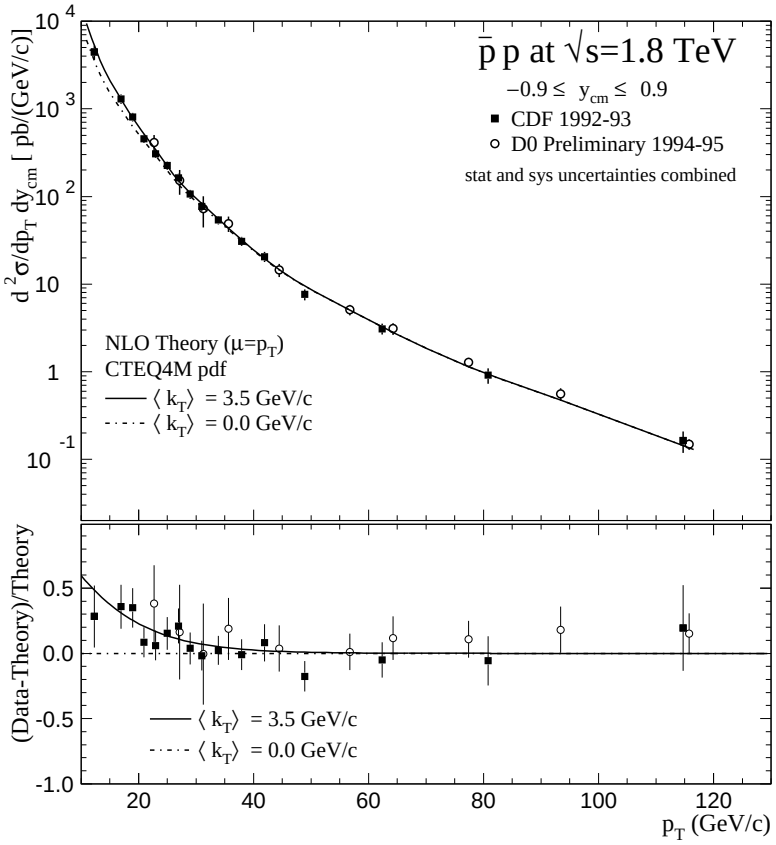

Figure 5.7: CDF and DØ isolated direct-photon cross sections compared to NLO theory, with and without intrinsic k_{T} [48].

5.5 Background

The above section has outlined what processes are included in the definition of direct photon processes. Now the backgrounds to this process need to be looked at. The largest source of background photons will come from meson decays, where the meson decays either directly (or through another meson) into photons. The creation of this meson would be as one of the constituents of a hadronic jet of particles, originating from a q or g. An example of this is shown in figure 5.8 as part of a di-jet event, which has the largest cross-section of any hard process. Being part of a jet means that the photon is likely not to be isolated, unless the meson is created at very high z. The majority of these mesons will be a π^0, which decays directly to two photons at the interaction point, as its lifetime is $\sim 10^{-17}$s. As the momentum of the pion increases then the separation distance between the photons it decays into decreases, which will make it harder to distinguish from the signal single photons.

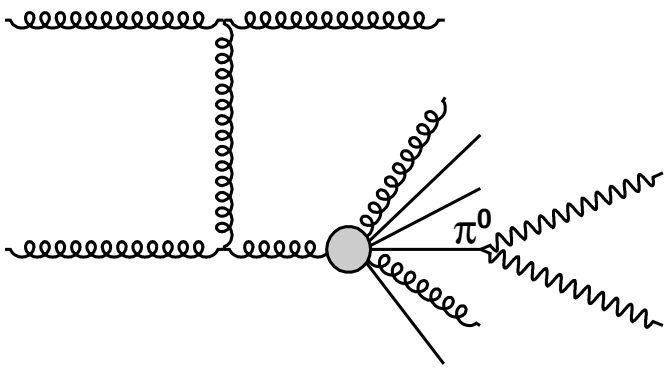

Figure 5.8: Feynman diagram showing a $\pi^0 \rightarrow \gamma\gamma$ decay inside a jet in a di-jet event.

5.6 Motivation

There is good reason for making precise measurements of the direct photon process, over a wide kinematic range, as it has several uses for:

- Calibration.
- Study of the gluon density of the proton.
- Parton evolution.
- Underlying event (see section 6.5.2).
- Backgrounds to, and searches for, new physics.

The role of direct photons is not just limited to pp collisions. It is also important in heavy ion collisions [49], but this is not discussed here.

When the photon and jet are produced in the central region of the detector, $|\eta| < 1.37$, then the energy of the photon can be measured very precisely. The jet energy measured in the opposite transverse direction to the photon should match this photon energy. This can be a powerful tool in the energy calibration of the hadronic calorimeter, a non-trivial problem due to energy lost in dead material and the nature of hadronic showers. This calibration applied at the level of jets is called the Jet Energy Scale (JES) and is important for any analysis using jets. Direct photons have been used for this at DØ [50], CDF [51] and RHIC [52] experiments as it is important to have an in-situ calibration of the hadronic calorimeter. This is also planned for ATLAS [53] and CMS [54]. Alternative methods for determining the JES are via in-situ top/W mass measurements and are discussed further in [55].

Studying the gluon x distribution is important for several key reasons. Firstly the error on the LO parton density function (PDF) for the gluon, figure 5.9a, is large with a minimum of 5% rising to 10% at low values of x, according to CTEQ [45]. These errors differ from those of MRST [56], which are much larger at values below 10^{-4}. The large uncertainty arises because there have been no measurements of

the gluon PDF in this range. The difference between the results of the two groups is because the CTEQ errors shown are extrapolated from the higher x region in a different way from MRST. The high x region is more striking as above $x = 0.1$ the error increases very fast and actually reaches 100% at around $x = 0.7$.

As well as the large errors on the LO PDF, figure 5.9b shows that there are large differences at higher orders when comparing NLO and next-to-next-to-leading order (NNLO) distributions[†]. One similarity between the distributions is that none of them show signs of the gluon distribution saturating at low x. If this doesn't happen then unitarity must eventually be violated with effects possible in the region probed at the LHC. This means that the gluon distribution has plenty to be studied over the whole x range.

Calculating the parton distributions at scales relevant to the LHC relies on the QCD evolution equations, as the parton distributions are usually only determined experimentally at lower scales by previous experiments, as shown by the difference in Q^2 going from HERA to the LHC in figure 5.6. Once the values are calculated for one scale they can be evolved up to the required scale (${p_{\mathrm{T}}}^2$). The most commonly used evolution equations are the DGLAP [57–59] scheme, which is adequate to describe all previous data. Others are BFKL [60–63] and CCFM [64–67]. The DGLAP evolution equations express the change of the parton densities with $\log(Q^2)$ at fixed x, the evolution being driven by splitting functions. These give probabilities of producing new partons via QCD radiation from an existing parton. One difference between the DGLAP and the other evolution equations is the ordering of partons arising from these splittings. For DGLAP the partons are ordered in transverse momentum, whereas BFKL, orders by x, and CCFM, orders by θ. The LHC operates in a new area of phase space so comparing its results to predictions evolved from other experiments will test which of these evolution schemes is the best approximation to QCD.

[†]NLO and NNLO PDFs cannot really be compared as $\hat{\sigma}$ is also order dependant.

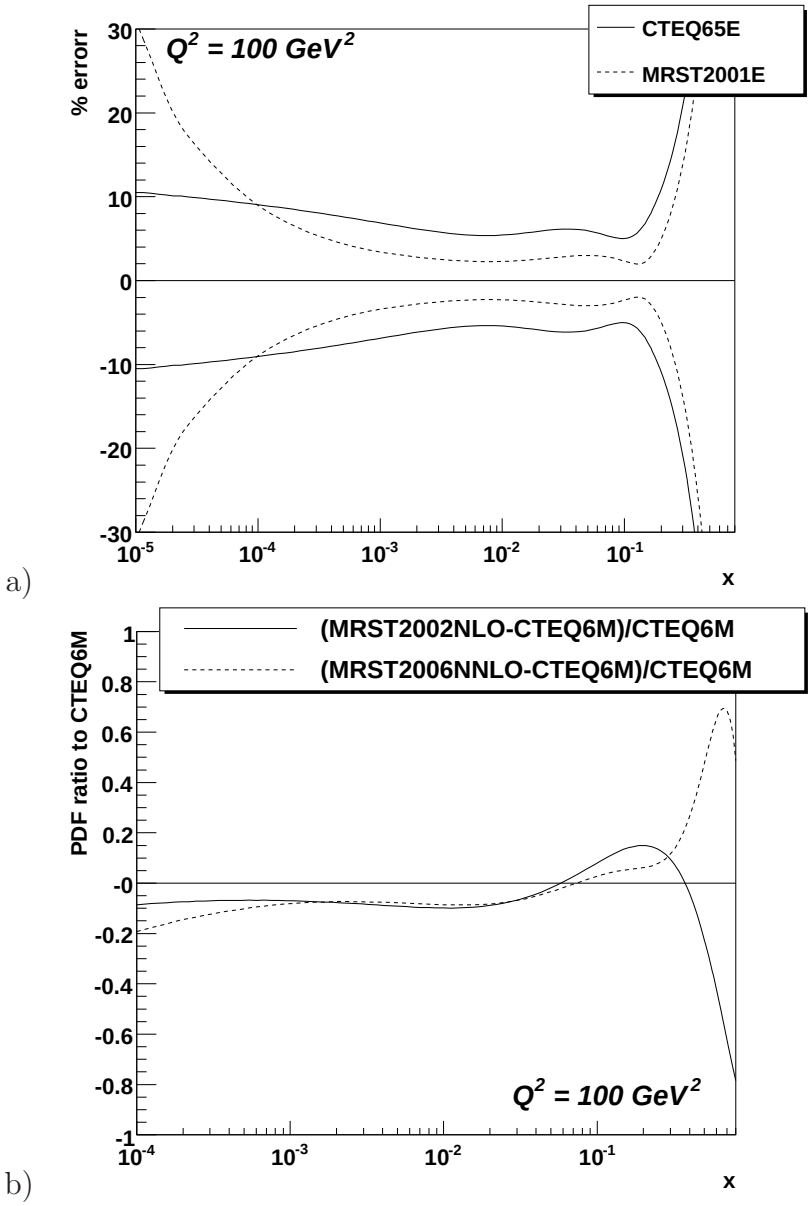

Figure 5.9: Gluon x distribution: a) LO errors from the CTEQ65E PDF and b) the differences between NLO(CTEQ6M), NLO(MRST2002NLO) and NNLO(MRST2002NNLO). Both plots were produced with [46].

An improved understanding of the gluon distribution is needed in order to interpret the results of searches for new particles produced from an incoming gluon, but there is also the opportunity to look for possible new physics through direct photons themselves. Excited quarks $qg \rightarrow q^* \rightarrow q\gamma$ [68], supersymmetry decay chains (non-pointing photons [20]) or any other final state containing a photon and a jet will all be selected in a direct photon analysis and could show up as a deviation of measurements from theoretical predictions.

Also the work used to identify photons in the direct photon channel and to separate photons from jet-induced background can be reused in any other processes with a photon in the final state. Most importantly direct photon events are the largest source of background in the $H \rightarrow \gamma\gamma$ search [19], as mis-identification of the jet in a direct photon event leads to an irreducible background of events with two photons. The probability of this mis-identification is closely related to the probability of mis-identifying a di-jet event as a direct photon process.

Chapter 6

Simulating Direct Photon Production

6.1 Introduction

Before data is taken by the LHC it is important to investigate the various models of the direct photon process. Differences between models and generators need to be well understood so that data taken by experiments can be interpreted through comparisons with theory. In this chapter, studies of the most frequently used generator in ATLAS, Pythia [69], are described, including running the generator as part of the ATLAS software chain and stand-alone. The results are compared to other generators, Herwig [70] and JetPhox [71], and there is a discussion of the effect of varying PDFs.

6.2 Generators

A generator, lying at the heart of a Monte-Carlo simulation in particle physics, can be classified by the approach it takes to simulate each step of a proton-proton collision, usually the hard process, I/FSR QCD and QED radiation, hadronisation, underlying event and hadron decays. A matrix element calculation of the particular hard process is the first step. This matrix element can be calculated at different orders of QCD, with the most common being LO. Some specialist generators produce this matrix element at higher orders, for example MC@NLO [72]. The output from these can be fed into other programs to produce a more complete simulation of an event after applying the parton shower and hadronisation steps, although care has to be taken not to duplicate any extra partons already produced in the higher order matrix element.

Figure 6.1 shows an illustration of expanding this hard process into a full event. A model of a parton shower, i.e. QCD I/FSR, is applied to the partons involved in the hard process as well as partons produced through perturbative decays and multiple scattering. The I/FSR of gluons and photons is intended as an approximation to higher order corrections to the matrix element. However this approximation does not always accurately model hard jet radiation.

Next the non-perturbative process of hadronisation is simulated, which takes all final state partons and tries to combine them into hadrons, as required due to colour confinement. There are two commonly used models for this: the Lund String Model and the cluster model. The Lund String Model [73] is a simulation of the production of $q\bar{q}$ pairs from the gluon field connecting two quarks at large distances. As the distance between two quarks increases, then the field lines between them narrow into a small region, which looks like a string. At some point the energy/force stored in the string causes it to split, producing quark-antiquark pairs. In the cluster model, colour-neutral clusters are created by following the colour flow through the gluons

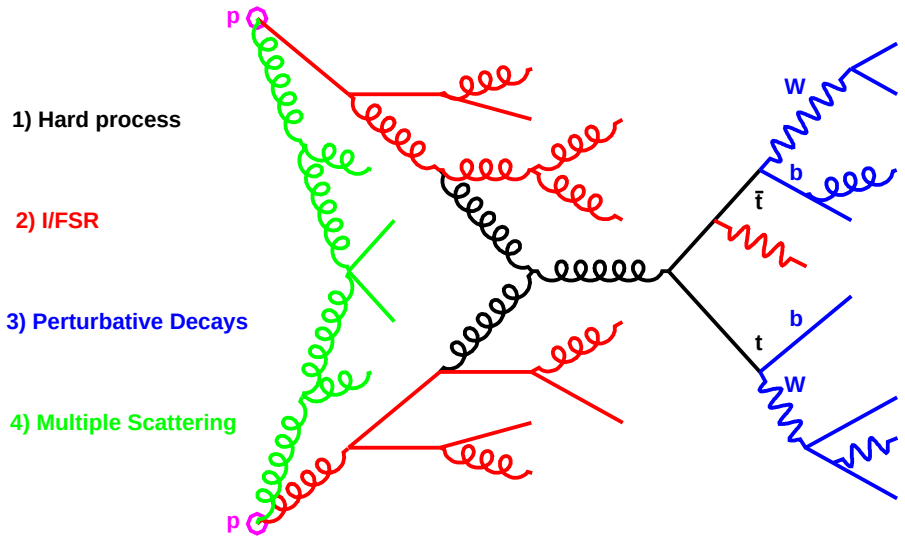

Figure 6.1: A representation of all QCD effects included in a typical simulation of a $t\bar{t}$ event.

produced in the parton shower. This event structure is more closely correlated to perturbative results from the parton shower, whereas the Lund String Model carries out non-perturbative splitting of $q\bar{q}$ pairs. The hadrons created are then decayed if they are unstable.

The outcome of the hard scattering collision is now described by hadrons, leptons and photons, but as the colliding particles at the LHC are protons, an underlying event description is needed. This creates hadrons from the remainder of each of the incoming particles, i.e proton beam remnants. Multiple scattering effects can also be included, as discussed later in section 6.5.2.

6.3 Pythia

Pythia is one of the event generators which contains all of the steps outlined above. It is a LO generator which can produce many $2 \rightarrow 2$ processes. It uses a p_{T} ordered

DGLAP parton shower, the Lund String Model of hadronisation and, within ATLAS, its own QED radiation is often switched off (for leptons) and replaced with PHOTOS [74], a dedicated QED radiation program. The output from Pythia is a predicted cross-section and a list of particle four momenta for each event, stored in the `Truth Container` when used in the ATLAS software. This list contains all the particles collided and subsequently created, which can be selected as described in appendix B.

In Pythia the Compton, annihilation and dual gluon direct photon processes can all be generated directly. The Bremsstrahlung process arises from photons created by the parton shower in di-jet events. Background photons, as described in section 5.5, will come from meson decays in di-jet events. Table 6.1 shows Pythia's predicted cross-sections for direct photon and di-jet events. This shows that the di-jet cross-section is far larger than that from any of the direct photon processes, with the dual gluon process being insignificant compared to the other LO direct photon processes. Also shown is the effect of running at $\sqrt{s} = 10$ TeV rather than the nominal LHC energy of 14 TeV, as mentioned in section 2.3, which shows that the di-jet cross-section increases slightly more than the LO direct photon cross-section.

Table 6.1: The Pythia cross-sections (for $p_{\mathrm{T}} > 20$ GeV and $|\eta| < 2.5$) of each direct photon process, the dominant di-jet process ($gg \rightarrow gg$) and the total from all di-jet processes.

Process	σ (nb) @ 10 TeV	σ (nb) @ 14 TeV	Increase in σ
Compton	67.6	96.0	1.42
Annihilation	4.95	6.40	1.29
$gg \rightarrow g\gamma$	0.05	0.08	1.57
$gg \rightarrow gg$	2.51×10^5	4.11×10^5	1.64
all di-jet	3.99×10^5	6.26×10^5	1.57

6.3.1 LO Direct photons in Pythia

A stand-alone generator level study has been carried out to investigate the LO direct photon process. Working with a generator stand-alone is a first step to simplify the analysis, as it removes any complications and time consumption from detector simulation and event reconstruction. Using Pythia[†], LO direct photon events, the Compton and annihilation processes, have been produced. Pythia was set up to run at the nominal LHC centre of mass energy, 14 TeV, in the range $|\eta| < 6$ to cover the whole ATLAS η range and avoid any migration effects from beyond the range of generation. Samples were created with p_{T} cuts of 5 GeV and 100 GeV applied to the initial particles from the hard interaction. Table 6.2 shows the number of events generated in each sample (along with the luminosity each sample corresponds to) and the effect of reducing the η range to $|\eta| < 2.5$, i.e. the tracking region of the ATLAS detector. This has less effect for the 100 GeV sample, as the plateau in the η distribution of the photon narrows with higher p_{T}. Figure 6.2 then separates the two LO direct photon processes and shows that the Compton process ($qg \rightarrow q\gamma$) is dominant over the whole p_{T} range.

Table 6.2: LO direct photon events generated with Pythia, see text for details

p_{T} cut GeV	Number generated	Sample luminosity (pb^{-1})	Number passing $\|\eta\| < 2.5$
5	12×10^{6}	2.3×10^{-1}	4.3×10^{6}
100	16×10^{6}	5.4×10^{3}	11.3×10^{6}

As the Compton process is the dominant LO direct photon process measurements have a high sensitivity to the gluon distribution. The kinematic coverage of the interacting q and g in terms of their x values is represented in figure 6.3. The peak of the distribution is at a relatively high x_q and low x_g, as the gluon dominates at

[†]Using Pythia v6.4.9.

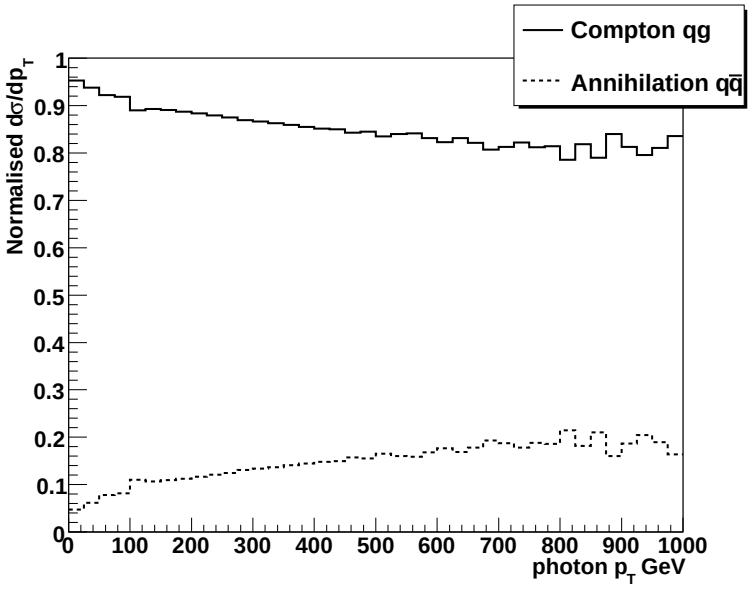

Figure 6.2: Fraction of generated LO direct photon events arising from the two subprocesses: Compton $qg \rightarrow q\gamma$ and annihilation $q\bar{q} \rightarrow g\gamma$.

low x, which is true for both of the p_{T} cut samples. The figure also shows that the x_q distribution reaches closer to $x = 1$ than x_g in the tail of the distribution, again due to the details of the PDFs because in the high x region the quarks dominate.

The observable range of x_g, in figure 6.3, is from 2×10^{-5} up to 0.7 for the 5 GeV p_{T} cut with the lowest x increasing to about 5×10^{-4} for the 100 GeV cut. The reduction in the detectable x range follows equation 5.2 and is visible in figure 5.6. Plotting x_q versus x_g works well at the truth level, as the partons in the hard-process can easily be identified and their momentum fractions are known. However this is not possible in data, instead momentum fractions for the two incoming partons x_1 and x_2 could be estimated from[†]:

$$x_{1,2} = \frac{x_T}{2}(e^{\pm\eta_\gamma} + e^{\pm\eta_{jet}}) \tag{6.1}$$

where x_T would be calculated from the photon using equation 5.1. As discussed already, the larger of x_1 and x_2 is likely to be the incoming quark. The distributions

[†]Based on the equations A.1 and A.2.

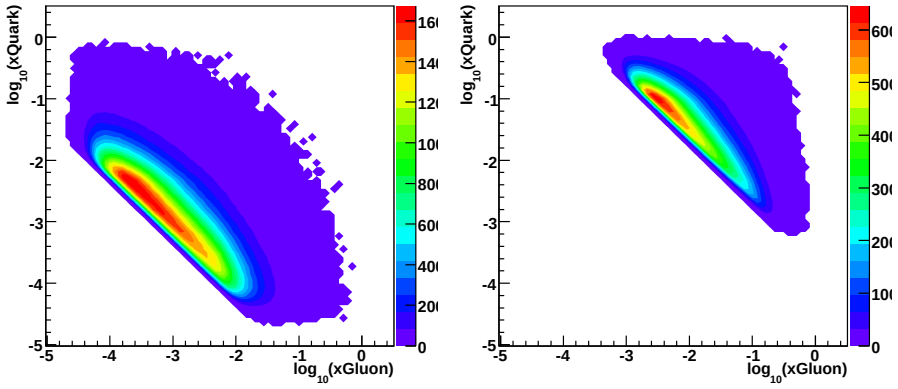

Figure 6.3: Distribution of x_q and x_g for the 5 GeV (left) and 100 GeV (right) p_{T} cuts on Compton events.

of x_1 and x_2 calculated from data could then be compared to Monte-Carlo predictions generated with different PDFs. Studying x_g in this way can also be done in di-jet events, although an advantage of using direct photons is that the calculation of x_T can just use the well known photon p_{T} (rather than the less accurate jet p_{T}). Differences between PDFs can also be seen in direct photon events, without any jet requirements, by studying the photon p_{T} and η distributions. As x is proportional to p_{T} but depends on the exponential of η, changes in x will result in larger changes in η than in p_{T} as is studied further in section 6.6.4.

6.4 Herwig

Herwig is another LO generator, including a parton shower, based on a different model to Pythia. Instead of its parton shower being ordered by p_{T} it creates an angular ordered shower, following the "colour dipole model" [75] (where gluons are emitted from dipoles, made of a colour-anticolour pair). It then uses the cluster model of hadronisation, rather than the Lund String Model used in Pythia. With tuning based on data, the predictions from Pythia and Herwig have often become

close to each other. As with Pythia, Herwig also uses external programs: PHOTOS and Jimmy. PHOTOS is used for QED radiation, but Herwig++[†] now has its own internal model. Jimmy [76] is an underlying event model and is discussed further in section 6.5.2.

6.5 Pythia v Herwig

Comparisons between these generators will show any differences arising from the different methods used in each program, which may be resolved by the first results taken from the LHC. The cross-sections for LO direct photon events, binned in p_{T}, are given in table 6.3. These show that Herwig consistently has a lower cross-section for LO direct photons than Pythia. This highlights a difference in the internal models, as the same phase space cuts and PDF are used for both and as the difference is independent of p_{T} it can not be caused by intrinsic k_{T} effects. To explore the differences between Herwig and Pythia further figure 6.4 compares some basic distributions for LO direct photon events. Other than the overall normalisation, the only difference can be seen in the η distribution, where Herwig seems to be falling off at the edge of the η range whereas Pythia is flat. These differences in normalisation and η (and understanding their origins) will become important when comparing PDFs, as discussed in section 6.6.4.

6.5.1 Isolation

The final area to study for making a direct photon cross-section, to go with the p_{T} and η ranges, is a variable which is sensitive to the photon isolation. In the generator the isolation is calculated by looking for other final state particles in an

[†]Herwig++ is the latest version of Herwig, both Herwig and Pythia (Pythia8) now use C++ instead of the Fortran versions used in this document.

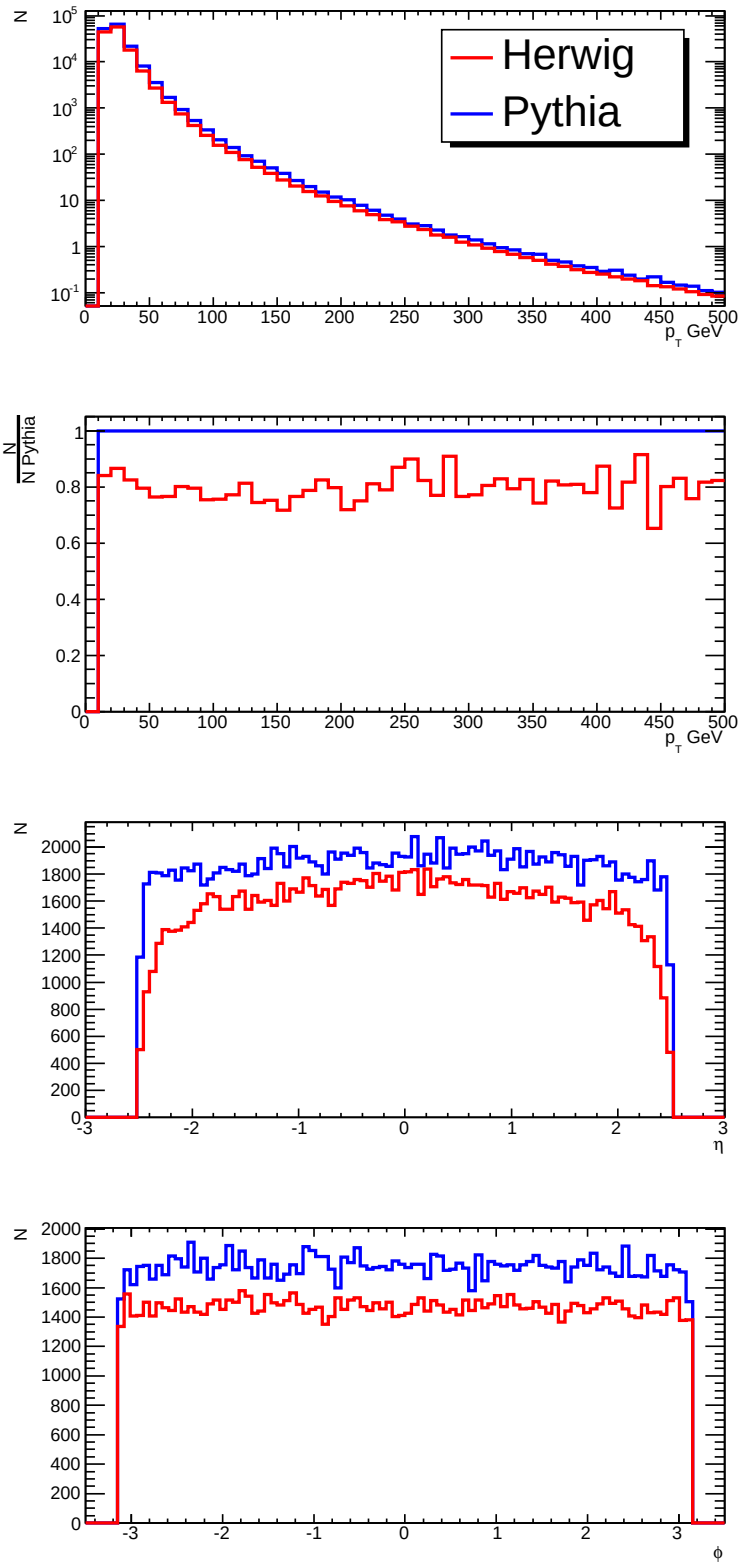

Figure 6.4: Comparison of the p_{T}(on a log scale and as a ratio), η and ϕ distributions, from Herwig and Pythia for direct photons with $p_{\mathrm{T}} > 10$ GeV and $|\eta| < 2.5$.

Table 6.3: Comparison of Herwig and Pythia cross-sections for LO direct photons with $|\eta| < 2.7$ and CTEQ 6L PDF.

Process	p_{T} Region (GeV)	Herwig σ (nb)	Pythia σ (nb)
Direct Photon	17-35	1.3×10^{2}	1.5×10^{2}
Direct Photon	35-70	1.6×10^{1}	1.9×10^{1}
Direct Photon	70-140	1.8×10^{0}	2.1×10^{0}
Direct Photon	140-280	1.6×10^{-1}	1.9×10^{-1}
Direct Photon	280-560	9.9×10^{-3}	1.2×10^{-2}
Direct Photon	560-1120	0.4×10^{-4}	0.5×10^{-4}

$\eta\phi$ cone of $\Delta R = 0.2$ around the photon. The technicalities of making an isolation measurement (including the reason behind this choice of cone size) are discussed in section 7.6.4.

An isolation variable that is appropriate over all p_{T} regions is:

$$\frac{et\ in\ cone\ 0.2}{photon\ p_{\mathrm{T}}} = \frac{transverse\ energy\ in\ a\ cone\ (with\ \Delta R = 0.2) - photon\ p_{\mathrm{T}}}{photon\ p_{\mathrm{T}}} \tag{6.2}$$

where any low values in this variable will then represent isolated photons. This variable is plotted in figure 6.5 for LO direct photon events generated by Herwig and Pythia. The LO direct photon events also contain information on the isolation variable for background and Bremsstrahlung photons, which can be accessed by studying the jet or hadronic system which is produced back-to-back with the photon. The background photons are typically not as isolated as the LO direct or Bremsstrahlung (although statistically limited) photons, as they originate from meson decays inside a jet. The agreement between Herwig and Pythia is good showing that isolation is a relatively model-independent variable to include in the selection of direct photon events, although the normalisation of the background and Bremsstrahlung photons will increase when looking at di-jet events, due to the di-jet

cross-section being larger than that for LO direct photons.

6.5.2 Underlying event

When the two protons collide the hard process products, e.g. direct photons or jet constituents, are not the only particles in the event. The remainder of the two protons, i.e. the proton remnants, create other particles near to the beam line, as they will continue to travel near to the initial proton's direction. In addition there can also be multiple interactions between different constituents of the two protons. Together with ISR these effects are collectively known as the underlying event. This is different from pile-up, which comes from other colliding protons in the same bunch. Understanding the underlying event is important especially when using isolation cuts, as it can affect the energy around the particle to be selected.

There are several concepts involved in modelling the underlying event. Here only simulations based on multiple hard scatterings are considered (cf. Herwig also has a soft model). There is then a p_{T}^{min} cut-off between hard and soft scatters, to avoid divergences as $p_{\mathrm{T}} \to 0$. There also has to be a matter distribution of each of the colliding hadrons, which are disk shaped due to being relativistically length contracted in their direction of travel. These hadrons will not necessarily collide head on, so an impact parameter, b, defines how much of the two hadrons overlap. Lastly after an interaction the colours and PDFs of quarks/gluons remaining need to be well modelled. Pythia has its own underlying model dependant on the impact parameter using a double Gaussian matter distribution with interactions ordered in decreasing p_{T} and PDFs that are rescaled after an interaction to conserve momentum. Herwig uses Jimmy [76] to model the underlying event, which is also dependant on the impact parameter but with a different (eikonal) model. Both of these models are discussed in [77], which also shows how these models are tuned to di-jet data taken by CDF and predictions for measurements at the LHC.

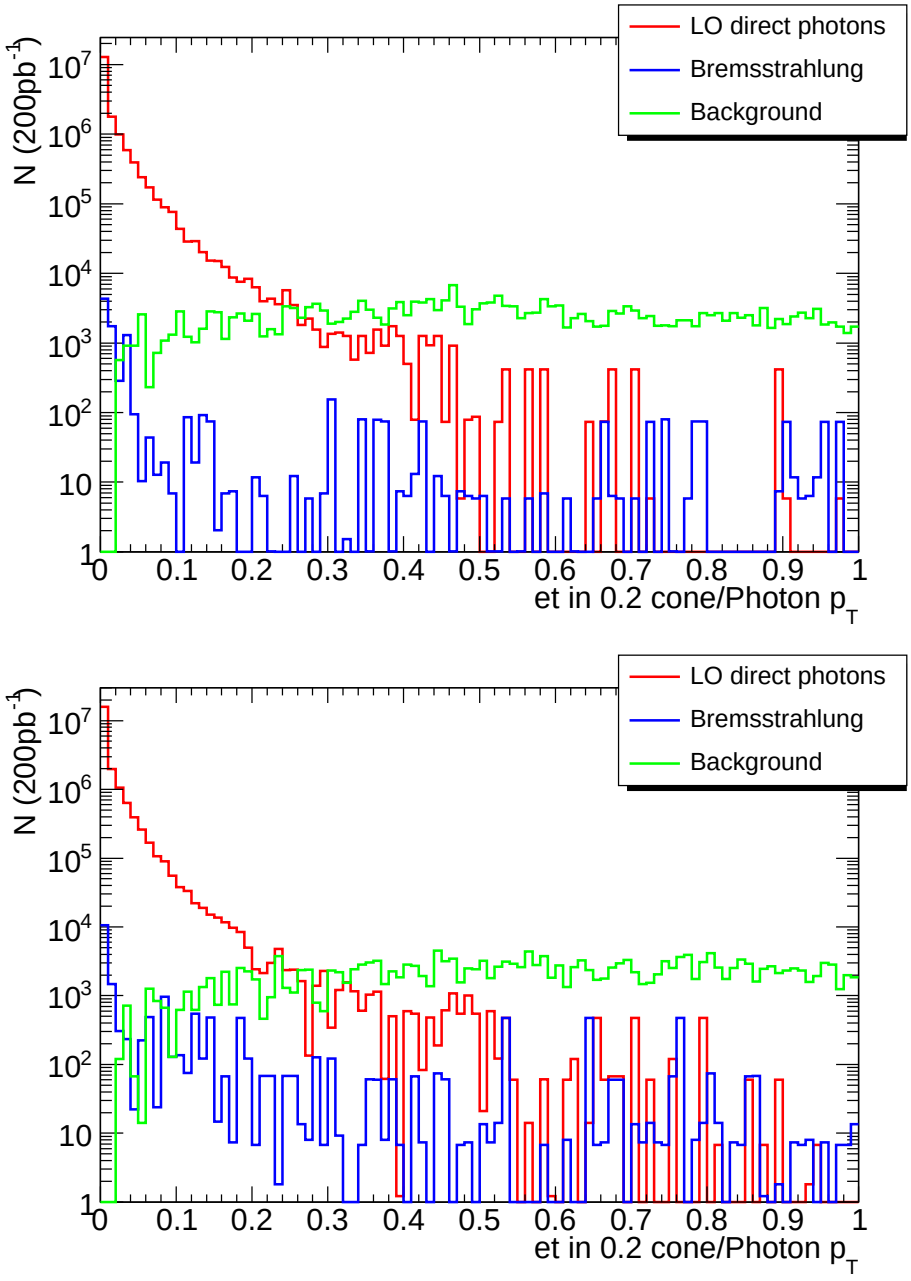

Figure 6.5: Isolation comparisons for direct photon events in Herwig(top) and Pythia(bottom), see text for further details.

The models of the underlying event from Pythia and Herwig are studied here in LO direct photon events. Firstly there are some quantities to define (as used in di-jet event studies at CDF) to enable this comparison. The selected photon is taken to define the ϕ axis. Relative to this three regions are defined in which activity is measured:

- *Towards*: $|\Delta\phi| < 60^\circ$
- *Transverse*: $60^\circ < |\Delta\phi| < 120^\circ$
- *Away*: $|\Delta\phi| > 120^\circ$

With this setup each region covers the same amount of phase space. In a truly back-to-back, in ϕ, LO direct photon event the *transverse* region will be empty, apart from any underlying event, so studying this region will give the best handle on the underlying event contribution. The quantities investigated in these regions, also for $|\eta| < 2.5$, are:

- Charged p_{T}: Scalar p_{T} sum of all final state charged particles
- Charged N: Number of final state charged particles
- E_{T}: Scalar E_{T} sum of all final state particles

These quantities are averaged over the number of events and produce the plots in figures 6.6 and 6.7. Figure 6.6 shows the trend that the charged particle density and p_{T} is highest in the *away* region, as the jet travels in this direction. The remaining regions show very similar results for charged particles, as the photon leaves no charged particles and only particles from secondary scatters are present (whose ϕ distribution is uncorrelated with the primary hard interaction). However, for the E_{T} quantity, where the photon itself is included, the *away* and *toward* regions match, but the *transverse* region is again just filled with underlying event.

Figure 6.7 shows these distributions zoomed in to the lower p_{T} region, where the underlying event should have more of an impact. From these distributions it can be

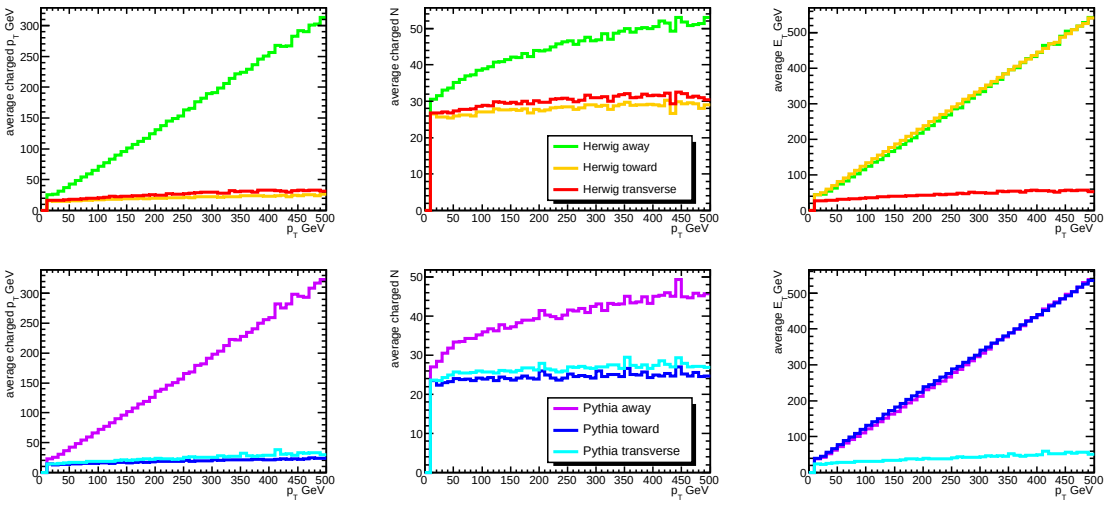

Figure 6.6: Underlying event in LO direct photon events from Herwig (top) and Pythia (bottom).

seen that Pythia and Herwig show good agreement in the shapes expected in each region, although the normalisations are slightly different. Small differences in shape do appear in the low p_{T} region of the *away* region, but as they are not present in the *transverse* regions this may not be from a difference in the underlying event models. What is clear, is that data from the LHC will enable further study of the differences between these models.

6.6 NLO

The generators discussed so far produce the lowest order direct photon processes (i.e. the LO and dual gluon processes), with the parton shower in di-jet events providing a model of the Bremsstrahlung contribution. This approximation can be tested by comparison with an NLO calculation, which should provide a better approximation to the hard sub-process. For direct photons the only available tool is the JetPhox generator [71], which performs the NLO cross-section calculation and is also able to produce events to create simple distributions. However, it doesn't have its own

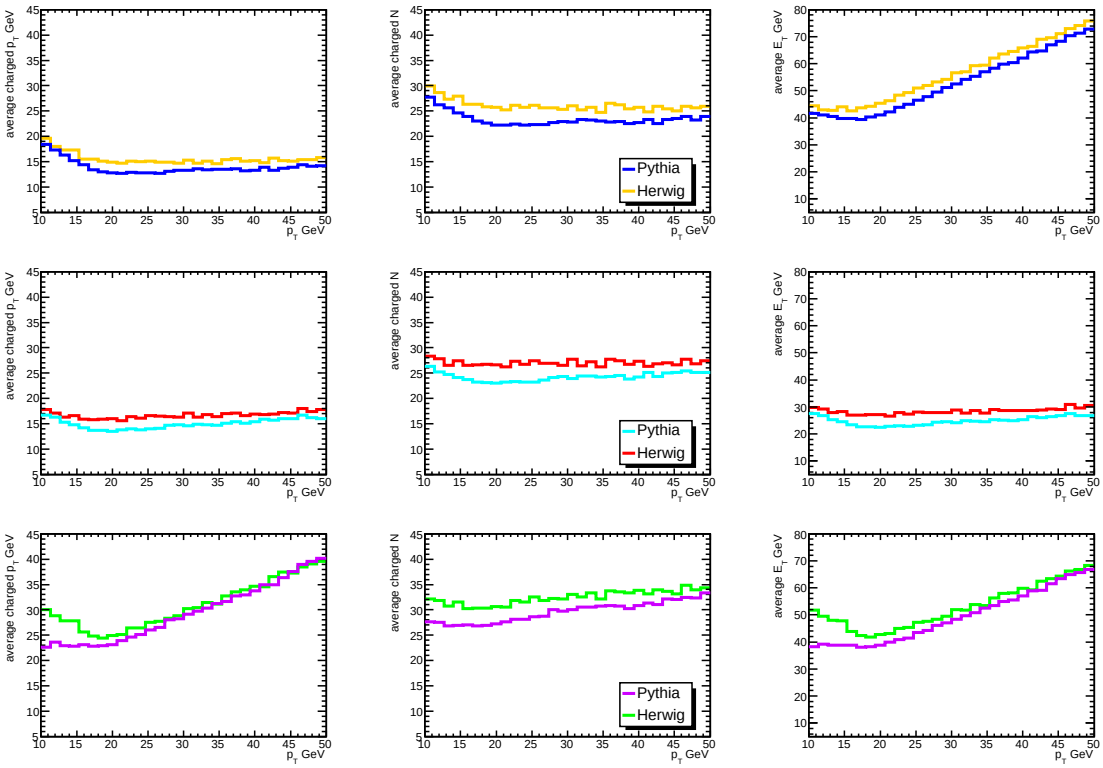

Figure 6.7: Underlying event comparisons for LO direct photon events from Herwig and Pythia. Plots separated into regions (from top to bottom): *toward*, *transverse* and *away*, see text for details.

parton shower or other underlying event simulation, or the ability to be fed into another generator to provide this.

Results published based on JetPhox calculations [78] showed agreement with all previous data, removing many of the worries about the intrinsic k_{T} problem discussed in section 5.4. This seemed to have been achieved through the proper inclusion of the higher order processes. However, more recently, with a larger dataset, DØ [79] has shown discrepancies (as before) with theoretical predictions, so it will be interesting to repeat this comparison at the LHC.

6.6.1 JetPhox parameters

Similarly to other generators, JetPhox[†] reads an input file containing all the parameters to control the event generation. After setting the collisions to resemble those at the LHC:

- Proton proton collisions at 14 TeV.
- Photons produced with 20 GeV $< p_{\mathrm{T}} <$ 1000 GeV and $|\eta| < 2.5$.

each of the parameters can be studied to see its effect on the calculated cross-section. By default the cross-section calculated includes a jet selection, which requires a k_t algorithm[‡] jet with a distance parameter of 1.0, 20 GeV $< p_{\mathrm{T}} <$ 1000 GeV and $|\eta| < 5$. The output of the calculation comes in two parts: "direct" and "one fragmentation", at both LO and NLO (denoted in JetPhox as Born and h.o. respectively). The "direct" and "one fragmentation" results have no real distinction beyond LO and as an NLO calculation is required all the contributions are combined in table 6.4 (see appendix C for the separated results), which gives JetPhox cross-sections and their dependencies on the key parameters.

[†]Using JetPhox v1.0.

[‡]See section 7.7 for details on jet algorithms.

Table 6.4: Results from altering one parameter at a time in JetPhox, see text for details.

Run	default	new	Total σ (nb)
0	default	-	179
1	default	add box	179
2	$\sqrt{s} = 14$ TeV	10 TeV	126
3	default isolation	off	186
4	default isolation	$< 0.1 p_{\mathrm{T}}$ in a 0.2 cone	159
5	photon+jet mode	inclusive	251
6	PTM= 0.05 GeV	0.08 GeV	179
7	$M = 0.5$	1	168
8	$M = 0.5$	2	146
9	$\mu = 0.5$	1	165
10	$\mu = 0.5$	2	150
11	$M_{ISR} = 0.5$	1	175
12	$M_{ISR} = 0.5$	2	164
13	$M_{FSR} = 0.5$	1	175
14	$M_{FSR} = 0.5$	2	174
15	combined final selection see section 6.6.2		214

Comparing the default run 0 with run 1 in the table shows the effect of adding the box (dual gluon) process, giving the same total cross-section to the precision quoted, as adding this process only adds 5.98×10^{-2} nb ($< 0.1\%$) to the Born "direct" cross-section. This confirms the previous result in table 6.1, that this is a very small contribution to the direct photon cross-section. Pythia results are also confirmed in run 2 where running at 10 TeV rather than 14 TeV would decrease the cross-section by a factor of 1.4.

The isolation requirement will be studied later on in section 6.6.3, but it is also studied as part of this parameter variation. Within JetPhox, which has no underlying event model, the isolation is defined by the transverse momentum of hadrons (${p_{\mathrm{T}}}^{\mathrm{had}}$) produced within a cone, which can be compared to either a fixed threshold or the photon p_{T}:

$$ {p_{\mathrm{T}}}^{\mathrm{had}} < Threshold \text{ (GeV)} \quad \text{or} \quad {p_{\mathrm{T}}}^{\mathrm{had}} < Fraction \times {p_{\mathrm{T}}}^{\gamma} \tag{6.3} $$

By default the isolation criterion uses a cone of radius 0.4, with a fraction of $2\times{p_{\mathrm{T}}}^{\gamma}$. To switch this loose isolation criterion off completely, the suggestion is to use a fixed energy cut of 7000GeV, as is done in run 3. Run 4 then uses the isolation requirement that will be later used in the event selection, as detailed in section 7.6.4, applying a $0.1 \times {p_{\mathrm{T}}}^{\gamma}$ cut with a cone of radius 0.2. Run 3 shows that the default isolation criteria reduces the cross-section by 4% whereas the criteria in run 4 reduces it by 15%, when both are compared to the cross-section with no isolation criteria.

Run 5 is an important change to make, as it changes the cross-section definition to an inclusive cross-section, i.e. removing the jet requirements. This is important for matching to the results in chapter 7 and makes a large difference to the cross-section. In contrast run 6 results in no difference to the total cross-section, to the precision quoted. This run is included here for completeness of all parameters changed from the default setting and investigates the JetPhox PTM parameter[†].

[†]This JetPhox internal parameter is altered, to 0.08 GeV, following the JetPhox steering file description of how it should relate to the minimum photon p_{T} (i.e. 20 GeV).

Runs 7 to 14 investigate the effect of changing the factorisation scale (M) and renormalisation scale (μ), defined in section 5.3. Both by default are set to $0.5 \times {p_{\mathrm{T}}}^{\gamma}$, and this factor is varied independently for each to $1.0 \times {p_{\mathrm{T}}}^{\gamma}$ and $2.0 \times {p_{\mathrm{T}}}^{\gamma}$. For M it is also possible to vary the initial and final state (I/FSR) factorisation scales independently. In these runs the total cross-section is altered by less than 20%, although the separated results in appendix C have large changes. As shown by the η distributions in figure 6.8, varying both the M and μ scales together results in the cross-section decreasing when the scale value increases (with any change in shape originating from statistical fluctuations and the fitting procedure used). The standard choice in this analysis is to set both scales to $1.0 \times {p_{\mathrm{T}}}^{\gamma}$, rather than the 0.5 set by default.

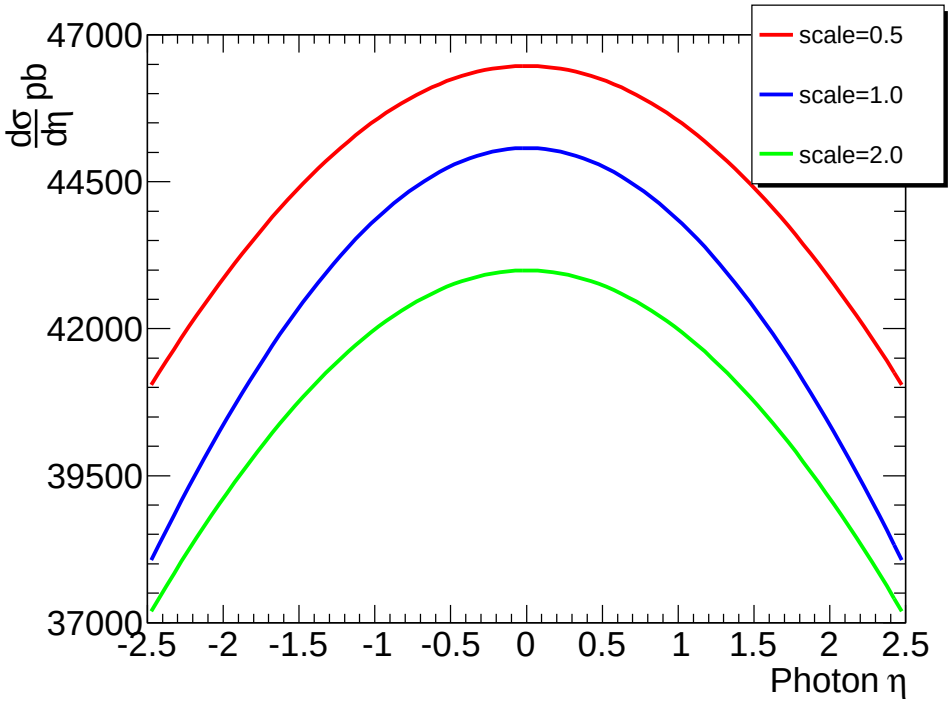

Figure 6.8: Illustration of the effect of varying both the M and μ scales to 0.5, 1.0 and $2.0 \times {p_{\mathrm{T}}}^{\gamma}$, for the sum of LO + NLO contributions. Distributions created in JetPhox as described in section 6.6.4.

6.6.2 Final parameter setting

After varying the parameter settings independently they can then be applied in combination. The final setting is shown in run 15 in table 6.4, equating to a cross-section of 214 nb (with each step of the combination shown in table C.2). To summarise, the parameters altered (to match those used in the next chapter) from the default are:

- Proton proton collisions at 14 TeV.
- Photons produced with 20 GeV $< p_{\mathrm{T}} <$ 1000 GeV and $|\eta| < 2.5$.
- Inclusive, i.e. no jet requirement.
- Renormalisation scale: $1.0 \times {p_{\mathrm{T}}}^{\gamma}$.
- Factorisation scale: $1.0 \times {p_{\mathrm{T}}}^{\gamma}$.
- PTM=0.08 (see discussion of run 6).
- Add box (i.e. all possible diagrams).
- Isolation using a cone of radius 0.2 with a cut of $< 0.1 {p_{\mathrm{T}}}^{\gamma}$.

6.6.3 Isolation

In [80] the isolation parameter is investigated for the Tevatron. This results in problems for isolation definitions with cone sizes of 0.1, whereby applying an isolation criteria results in a cross-section larger than the cross-section from a calculation without any isolation criteria. As already mentioned the isolation cut in JetPhox follows equation 6.3, and has already been studied in runs 3 and 4. To investigate the isolation parameter, five different cone sizes and four energy requirements were tested (by altering the isolation criteria in the final parameter setting) as shown by the total cross-sections in table 6.5 (again see appendix C for the separated results).

Looking at the cuts applied the 2 GeV and $< 0.1 p_{\mathrm{T}}$ requirements yield very similar cross-sections, matching to within 2% for all of the cone sizes. However the

Table 6.5: JetPhox cross-sections for different isolation requirements.

Run	Isolation	Total σ (nb)
16	0.1 cone $< 0.1 p_{\mathrm{T}}{}^{\gamma}$	234.2
17	0.1 cone < 2 GeV	234.9
18	0.1 cone $< 0.5 p_{\mathrm{T}}{}^{\gamma}$	229.6
19	0.1 cone $< 2.0 p_{\mathrm{T}}{}^{\gamma}$	241.5
20	0.2 cone $< 0.1 p_{\mathrm{T}}{}^{\gamma}$	213.5
21	0.2 cone < 2 GeV	213.6
22	0.2 cone $< 0.5 p_{\mathrm{T}}{}^{\gamma}$	218.2
23	0.2 cone $< 2.0 p_{\mathrm{T}}{}^{\gamma}$	238.9
24	0.4 cone $< 0.1 p_{\mathrm{T}}{}^{\gamma}$	192.1
25	0.4 cone < 2 GeV	191.3
26	0.4 cone $< 0.5 p_{\mathrm{T}}{}^{\gamma}$	206.5
27	0.4 cone $< 2.0 p_{\mathrm{T}}{}^{\gamma}$	236.2
28	0.7 cone $< 0.1 p_{\mathrm{T}}{}^{\gamma}$	172.7
29	0.7 cone < 2 GeV	170.8
30	0.7 cone $< 0.5 p_{\mathrm{T}}{}^{\gamma}$	196.2
31	0.7 cone $< 2.0 p_{\mathrm{T}}{}^{\gamma}$	233.8
32	1.0 cone $< 0.1 p_{\mathrm{T}}{}^{\gamma}$	157.5
33	1.0 cone < 2 GeV	154.5
34	1.0 cone $< 0.5 p_{\mathrm{T}}{}^{\gamma}$	188.4
35	1.0 cone $< 2.0 p_{\mathrm{T}}{}^{\gamma}$	232.0
36	iso "off"	243.4

fractional cut will be kept as it is safer in a reconstructed selection, see section 7.6.4. When comparing the different cone sizes used, the cross-section always reduces with increasing cone size for the same cut, which is understandable as a bigger cone should contain more hadrons and so is more likely to fail the same cut. For all cones and cut the sum of the LO + NLO contributions is always less than the non-isolated case. This suggests that for this parameter setting all of these isolation criteria are safe to use, including the 0.1 cone which did not work in the Tevatron setup.

6.6.4 PDF Sensitivity

As mentioned in section 6.3.1, the differences between PDFs should be most noticeable by investigating the η distribution. It was also found in [4] that the η dependence is most closely correlated to the x dependence. Comparisons between Pythia and Herwig already showed differences in normalisation and η distributions, figure 6.4, so these would need to be well understood before PDF comparisons with data could be reliably interpreted.

Using the final parameter setting in JetPhox, events are produced in order to obtain differential cross-sections in η and p_{T}. To compare several PDF sets the "direct" and "one fragmentation" η distributions are combined to create LO + NLO distributions. To reduce the sensitivity to statistical fluctuations from the data points, Gaussian fits are used (using a Gaussian seemed to fit the data adequately). The fit is required to be centred on $\eta = 0$ as required by symmetry. Figure 6.9 then shows the result of this fitting procedure for one of the PDF sets.

Following this procedure all the PDFs available within JetPhox can be compared. Figure 6.10 shows this comparison for LO + NLO combined, including the relative deviation compared to the default PDF in JetPhox, CTEQ 6. The largest differences between the PDFs is observed around $\eta = 0$, apart from CTEQ 5 which differs at large η. The MRST PDFs are lower than those from CTEQ, although they are

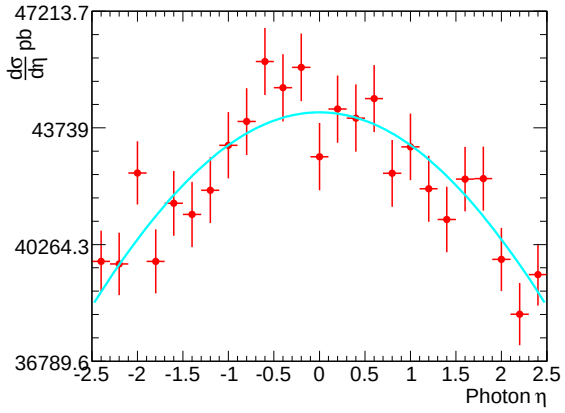

Figure 6.9: Comparison of the fitted Gaussian to the η distribution for LO + NLO for the CTEQ 6.1 PDF.

older so contain less precise input data. Overall the largest difference is up to 10% at $\eta = 0$, but when comparing the MRST 04 (the latest MRST PDF available in JetPhox) to CTEQ 6 this reduces to less than 5%. Achieving a measurement of this accuracy is likely to need a large amount of data, to be able to reduce the systematic error on the measurement (as is discussed later in section 8.4).

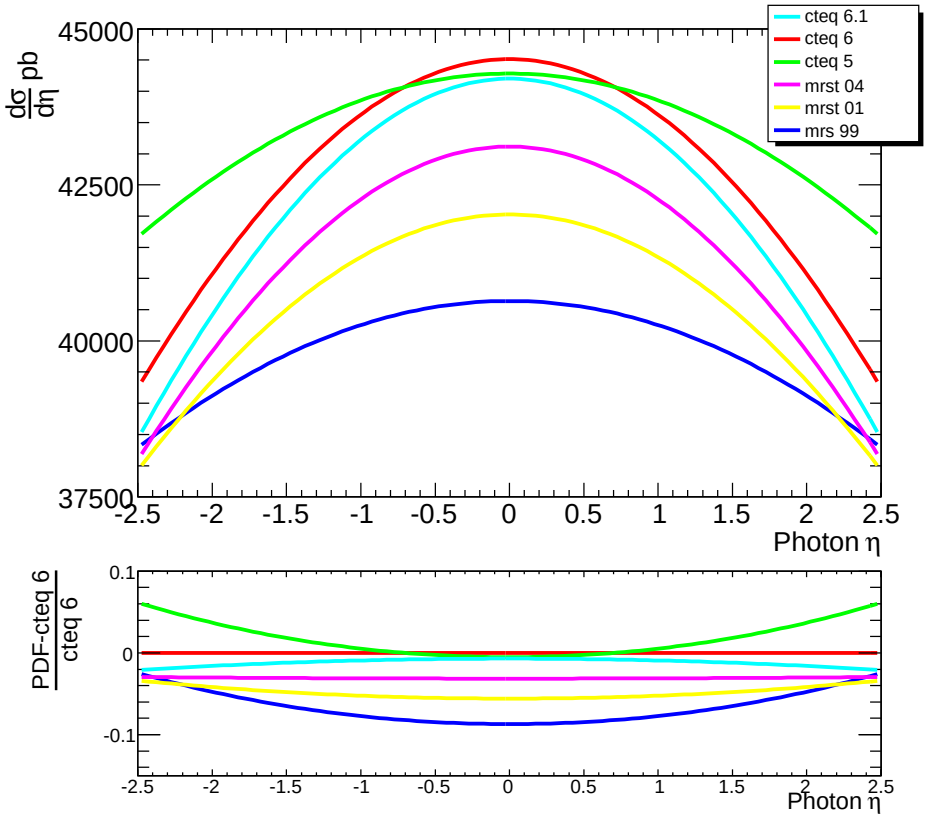

Figure 6.10: Comparison of the η distributions from several different PDFs for LO + NLO.

Chapter 7

Selecting and Reconstructing Direct Photon Events

7.1 Introduction

To model real events the full ATLAS simulation must be applied to events generated as described in chapter 6. The simulation is designed to match what we expect the detector performance to be like. Based on the simulation output, variables can be studied to work out optimal ways of selecting direct photon events and reconstructing their properties. Details of the simulation and the most useful detector variables are documented in this chapter.

7.2 Data Formats

When events are taken by ATLAS they will be stored in a `RAW` format. From this the offline reconstruction (ATHENA) produces Event Summary Data (`ESD`), containing data from the full tracker, calorimeter and muon detector. These files are rather

large, due to the very high number of cells and hits, so ATHENA also produces the Analysis Object Data (AOD) format. Contained in the AOD are lists of objects (for example: tracks, calorimeter clusters, jets, photons, electrons), which are not as detailed as in the full ESD format, resulting in much smaller file sizes. Further reductions can be made to produce specific Derived Physics Data (DPD), with data chosen depending on the physics analysis. Lastly there is also the TAG format, which is useful for applying a pre-selection before carrying out a more detailed analysis on AODs or ESDs.

This reconstruction process is reproduced in the simulation of ATLAS events. The simulation uses the EVGEN file from the Monte-Carlo generator, which consists of a listing of four vectors of particles created in the event including all those which decay into other particles. The final state particles, i.e. ones that would be seen in the detector, are then passed through a detector geometry and material simulation (GEANT [81]), a representation of how the detector would respond to these particles passing through it. The output is then digitised, i.e. the detector readout is simulated, into DIGI files, a replication of the RAW data that would be produced from real events. This then feeds into the reconstruction chain to create replicas of all the data formats produced with real events, as shown in figure 7.1.

7.3 Filters

The simulation samples are generated for each relevant process, in different regions of phase space, and then pass through the simulation chain described above. The first step of generating events is very quick, many thousands of events can be produced in seconds. However to simulate the detector response and reconstruct an entire event can take up to thirty minutes, so before passing through these steps the generated samples have filters applied to remove unnecessary events for the particular analysis, for example events that are outside of the phase space of the measurement.

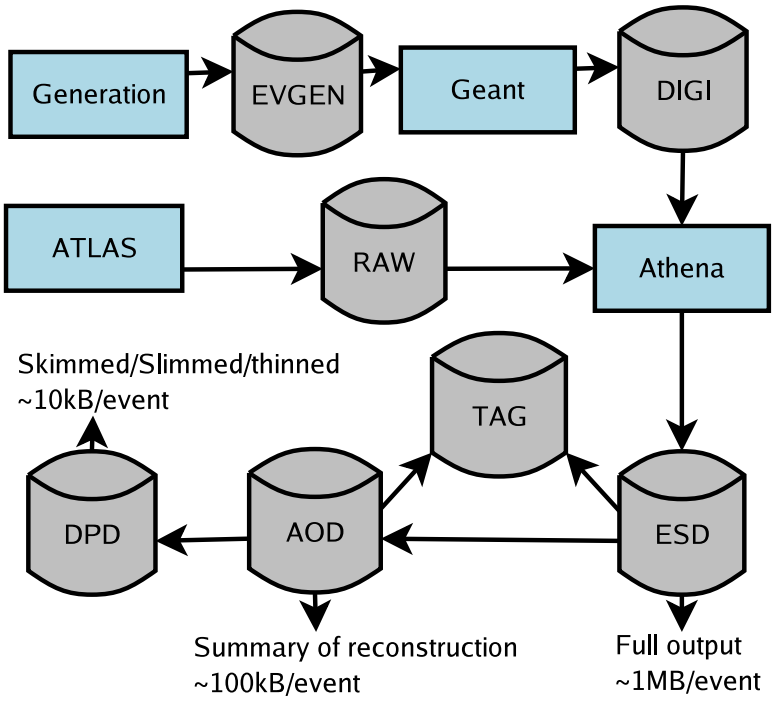

Figure 7.1: Chain of reconstruction for real and simulated data.

In the samples of interest there are photon and jet filters applied. The photon filter is rather simple, requiring a pre-defined number of photons to pass minimum p_{T} and maximum $|\eta|$ cuts. It then returns true if enough photons pass the cuts. The jet filter is more complex than the photon filter as there are no jets defined at the generator level, just hadrons. Instead a grid of cells (with $\Delta\eta \approx 0.6$, $\Delta\phi = 0.6$) is created, in which the energies of all final state truth particles (excluding muon's and neutrino's) are combined. The cells are then merged to create "objects" of 2×2 or 4×4 cells, respectively, depending on whether a "tight" or "loose" filter is required. Then, as with the photon filter, the jet filter requires that enough of these "objects" pass the required p_{T} and η cuts.

7.4 Analysis Sample

The cross-sections in table 6.3 relate to the direct photon and di-jet samples produced by ATLAS. Prior to entry in this table, the direct photon events are filtered by the photon filter, as discussed in appendix D.1. The di-jet samples, however, have no filter applied to them. This means many of the events will lie outside the phase space of this measurement and given the relatively small probability that a direct photon can be faked in a di-jet event, this sample therefore suffers from very poor statistics as a sample of background or Bremsstrahlung photons.

An alternative sample has a filtered combination of the direct photon and di-jet processes. Originally this sample was created as a general sample for study of backgrounds to processes involving photons and electrons and is discussed further in appendix D.2. This sample only has a minimum p_{T} requirement, so avoids problems of large weights being applied when merging samples with small statistics and different p_{T} cuts, as is the case with the binned di-jet and direct photon samples in table 6.3. Most importantly this combined sample has a jet filter applied, which means less events need to be analysed than in the normal di-jet events, reducing statistical fluctuations.

The combined sample has a minimum p_{T} cut of 15 GeV on the hard processes, which is followed by the tight (2×2 cells) jet filter requiring one "object" with $p_{\mathrm{T}} > 17$ GeV and $|\eta| < 2.7$. These cuts are summarised in table 7.1, which also documents the cross-section, number of events produced for this sample and the equivalent integrated luminosity.

One last point on this selected sample (which also applies to the other individual direct photon samples) is that the dual gluon process is not included as one of the direct photon processes. However this process is not essential to the analysis as it has a very small cross-section compared to the LO processes. This was seen in results from JetPhox, in section 6.6.1, and was confirmed by generating a separate

Table 7.1: Details of the sample used in this analysis, where both σ and N events include the filter efficiency.

Processes	p_{T} cut	tight jet filter	σ (nb)	N events	Luminosity
Direct photon + di-jets	> 15 GeV	1 "object" $\lvert\eta\rvert < 2.7$ $p_{\mathrm{T}} > 17$ GeV	1.91×10^{5}	7754830	0.04 pb^{-1}

sample, within the ATLAS software, with a minimum p_{T} cut of 7 GeV (i.e. at low p_{T} where the dual gluon contribution should be largest) and $|\eta|$ <2.7. This resulted in a dual gluon process cross-section of 2.52 nb compared to the LO cross-section of 1.49×10^{3} nb, i.e. the dual gluon process represents less than 0.2% of the LO cross-section.

7.5 Trigger

As outlined in section 2.9, the ATLAS trigger has three levels and all three have to be passed for an event to be written out. The last two levels of the trigger are both based on software, so are easily reproduced in the offline simulation. However the first level is purely hardware based, so it has its own dedicated simulation to reproduce its results. The photon trigger requires an EM calorimeter cluster above an energy threshold for the first level, whereas the other levels apply a looser version of the offline isEM photon selection, detailed in section 7.6.

The energy thresholds applied define the names for each of the triggers. At L1 there is no distinction between electrons and photons, so triggers are labelled EM# (where # represents the value of the p_{T} cut in GeV). These then relate to g# triggers applied in the later levels of the trigger (g for gamma, with # again representing the p_{T} cut which may be higher than at L1) . If the p_{T} cut is too

low, then the rate at which this trigger accepts events will be too high, which would cause problems with trying to write out too much data. To avoid this a trigger can be prescaled so that only a fixed fraction of events are kept, i.e. if the prescale is 10 every 10th event passing this item will be kept. These prescaled triggers are useful for monitoring the efficiency of the triggers with higher thresholds, but those with low p_{T} requirements are so heavily prescaled that the rate at which events are passed is actually lower than the first unprescaled triggers [82]. To minimise statistical uncertainties the lowest unprescaled triggers are generally used for the first physics analysis.

For photons the first trigger which is unprescaled, and hence the trigger to be used in this analysis, is the g20 item, which applies an 18 GeV cut at L1 before applying a 20 GeV cut in the higher levels of the trigger. Figure 7.2a shows the efficiency of this g20 item, as a function of photon p_{T}, at keeping events where there is a LO direct photon or Bremsstrahlung photon, with $p_{\mathrm{T}} > 20$ GeV and $|\eta| < 2.5$. This shows that the trigger efficiency reaches around 80%. It does not reach 100% efficiency for selecting these events due to the fact that it is already applying some of the photon isEM selection, described in the next section. Figure 7.2b shows where the rejected events lie, showing rejection at high η and in the calorimeter crack region, see 2.7. However, figure 7.2c shows that $> 90\%$ of events that have a photon passing this offline photon selection will have passed the photon trigger, as the cuts are looser in the trigger. In the latest releases of the ATLAS offline software both of these efficiencies would be higher, as errors [83] in the g20 trigger implementation (whereby all isEM cuts were applied in the higher levels, to the extent that some cuts were tighter in the trigger than isEM) have been fixed. However these errors will not effect this study as the effect is uniform in η as shown in figure 7.2b apart from the main rejection regions, which come from the isEM binning as described in section 7.6.3.

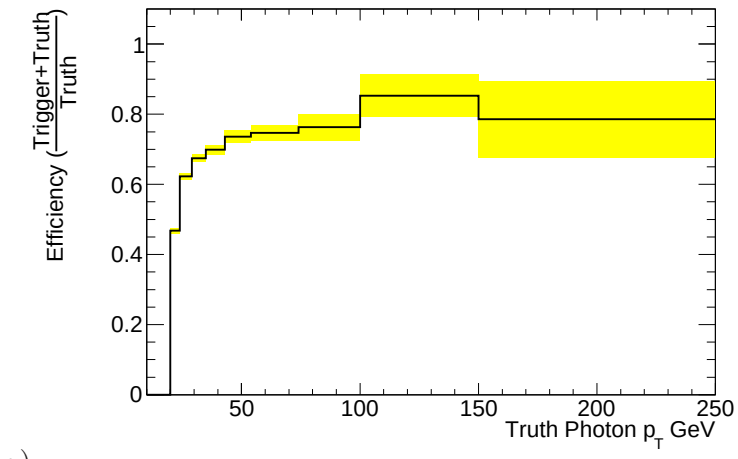

a)

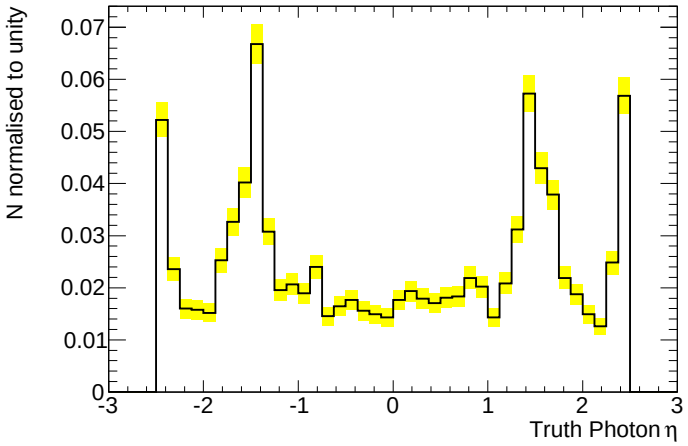

b)

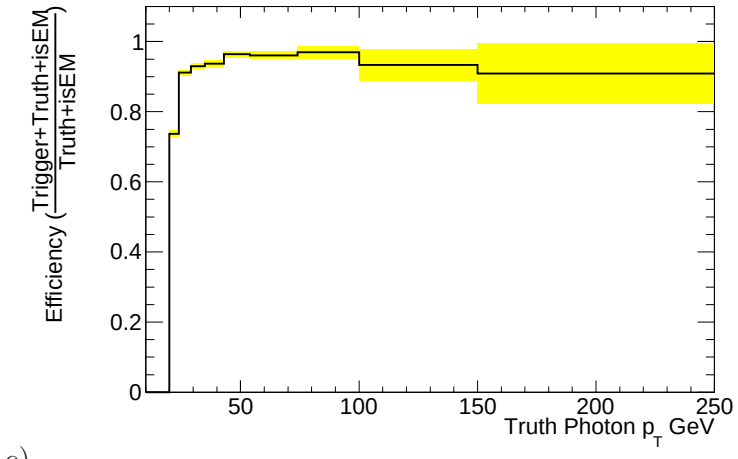

c)

Figure 7.2: The effect of applying the g20 photon trigger when trying to select events with either a LO direct photon or a Bremsstrahlung photon, with $p_{\mathrm{T}} > 20$ GeV and $|\eta| < 2.5$: a) efficiency as a function of p_{T}, b) rejection of signal events as a function of η and c) the efficiency after applying the additional requirement that there must be at least one reconstructed photon passing the isEM selection in the event.

7.6 Photon Reconstruction

Photons, and electrons, are reconstructed from clusters of deposits in the EM calorimeter. The electron/photon separation is mainly dependent on the reconstruction of the electron track. However the reconstruction algorithm allows a photon to be matched to a track if it has been identified as a conversion. Around 80% of photons will convert before reaching the EM calorimeter, but most of these convert in the solenoid, leaving no track in the Inner Detector.

As described in section 5.5, the main background for direct photons comes from meson decays to multiple photons originating from a jet. An example of what the shower shapes for a typical photon and a jet look like is shown in figure 7.3. In this case a clear separation is possible between the photon with no associated track and a slim shower and a jet with many tracks and a wider and deeper shower extending well into the HCAL. Due to the isolation and shower shape requirements described below, the probability for a jet to fake a photon is low, but the di-jet background to direct photons remains important as the cross-section is much larger than that for direct photons. For the jet to fake a photon most of the energy has to end up in the EM calorimeter. This mainly occurs for $\pi^0 \rightarrow \gamma\gamma$ decays inside the jet, when the π^0 has taken most of the jet energy (i.e. high z).

7.6.1 isEM

The bulk of the π^0 background is removed on the basis of the shower shape of the photon candidate, by using p_{T} and η dependent identification cuts. As described in section 2.7 and shown in figure 2.12 the EM calorimeter consists of three layers in the barrel region, along with a presampler. As mentioned there, the first layer is used to look at the width of the shower, to discriminate π^0 decays, and the second to measure the energy deposition. These general principles can be seen in the shower

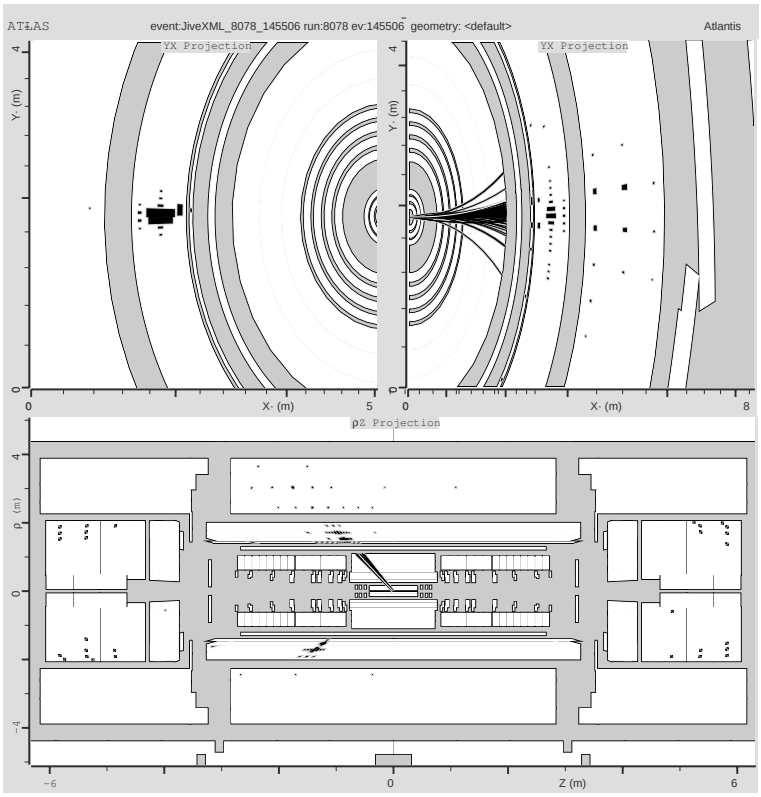

Figure 7.3: Example showers for a 786 GeV photon (left) and a 722 GeV jet (right) displayed in Atlantis.

shape variables and cuts used in the selection and reconstruction.

7.6.2 Variables

Each reconstructed photon, stored in the `Photon Container`, has a list of variables (from the `EMshower` object) associated to it, which make up the basis of the photon identification. These variables are present in the `AOD` so that the identification can be repeated/altered offline, rather than having to look at the individual cells in an `ESD`. In the first two layers, see figure 2.12, the variables are:

- First layer energy: `e2tsts1` is the energy of the strip which has the second largest energy in the first layer and `emins1` is the energy of the strip which

has the smallest energy among strips which are located between the first and second most energetic strips.

- First layer width: weighted by energy looking at 3 (`weta1`) or 40 (`wtots1`) strips (with number i) around the strip with maximal energy (i_{max}):

$$width = \sqrt{\frac{\sum Energy_i \times (i - i_{max})^2}{\sum Energy_i}}$$

- First layer shower: `f1` is the ratio of the first layer cluster energy to the entire cluster (E_1/E) and `fracs1` is $\frac{E_7 - E_3}{E_3}$, where E_n is the energy in n strips centred around the strip with highest energy.
- Second layer energy: `e233` is the sum of energy (uncalibrated) in 3×3 cells, similarly: `e237` in 3×7 cells and `e277` in 7×7 cells.
- Second layer width: lateral width, weighted by the energy of all cells using the η position of each cell:

$$width = \sqrt{\frac{\sum(Energy \times \eta^2)}{\sum Energy} - \left(\frac{\sum(Energy \times \eta)}{\sum Energy}\right)^2}$$

  in 3×5 cells, with (`weta2`) and without (`widths2`) a correction to avoid bias from the finite cell size.

There is also a third layer variable `f3core`, which is the fraction of the energy in the third layer (3×3 cells) compared to the full cluster ($e333/E$). The cells behind this layer, from the first layer of the HCAL, are also used by the variable `ethad1` to quantify leakage into the HCAL. For isolation studies the energy around the photon is accessible via the `etcone20` variable. This calculates the transverse energy in a cone of $\Delta R = 0.2$ subtracting the energy of the photon cluster and is discussed further in section 7.6.4. Finally for photons there are also boolean flags to determine if the photon came from a conversion. The flag `convtrackmatch` indicates that the track associated to the photon is a track from a conversion vertex , whereas `convanglematch` indicates that both tracks from a conversion vertex are within an angle of 0.05 (in both θ and ϕ) of the photon cluster.

7.6.3 Cuts

A selection of the variables defined in section 7.6.2 are chosen to create an optimal selection of photons and rejection of backgrounds. As mentioned above the cuts vary with p_{T} and η, taken from the cluster associated to the photon. The cuts are determined for two sets of intervals, for both p_{T} and η, one for the variables describing the first layer (strips) of the EM calorimeter[†] and one for the remainder of the variables. These intervals are:

- p_{T} (GeV): < 30, 30-40, 40-50, 50-60, 60-70, 70-80 and > 80.
- $|\eta|$: < 0.7, 0.7-1.0, 1.0-1.5, 1.5-1.8, 1.8-2.0, 2.0-2.5.
- strips p_{T} (GeV): < 25, 25-30, 30-40, 40-50, 50-60, 60-70, 70-80 and > 80.
- strips $|\eta|$: < 0.7, 0.7-1.0, 1.0-1.37, 1.52-1.8, 1.8-2.0, 2.0-2.37.

The variables selected, combined and renamed, form the cuts shown for three example regions in table 7.2[‡]. The table shows the large dependences on η and p_{T} for some of the variables. These variables have been optimised [5] by studying the simulated response to a single photon, compared to the response of a jet or a single π^0, with the largest discriminating power coming from the `hadleakage` and `ratio1` variables for rejecting jets and the `emax2r` and `deltae` variables for rejecting neutral pions. The optimisation of the cuts has only been performed in low p_{T} bins, as required for low mass $H \rightarrow \gamma\gamma$ studies. Repeating this procedure for direct photons and extending the bins to higher p_{T} could improve the background rejection [4].

Using these cuts the photon selection has been optimised [5] to maximise photon efficiency (% of photons kept) and jet rejection (a rejection of 1000 means 1 in 1000 jets passes the photon selection). The results of this optimisation can be seen in

[†]There are no thin strips in the regions $|\eta|$=1.37-1.52 and $|\eta|$=2.37-2.5, so these regions fail the isEM selection.

[‡]`iso` is actually set (artificially at 1000) to not be applied, see sections 7.6.4 and 7.6.5.

Table 7.2: Variables used by the isEM selection. Brackets show the variables as defined in section 7.6.2 that make up a derived quantity. Cuts are shown for three example p_{T} and η ranges, energies or p_{T} are in MeV when used in these variables.

Region → Variable ↓	$\lvert\eta\rvert < 0.7$ $p_{\mathrm{T}} < 25$ GeV	$2 < \lvert\eta\rvert < 2.37$ $p_{\mathrm{T}} < 25$ GeV	$\lvert\eta\rvert < 0.7$ $p_{\mathrm{T}} > 80$ GeV
`hadleakage` (`ethad1`/p_{T})	≤ 0.006	≤ 0.007	≤ 0.006
`iso` (`etcone20`/p_{T})	< 1000	< 1000	< 1000
`e277`	≥ 0.1	≥ 0.1	≥ 0.1
`ratio1` (`e237`/`e277`)	≥ 0.925	≥ 0.915	≥ 0.952
`ratio2` (`e233`/`e237`)	≥ 0.6	≥ 0.8	≥ 0.92
`weta2`	≤ 0.0108	≤ 0.0123	≤ 0.0097
`emax2r` (`e2tsts1`/(1000.+0.009×p_{T}))	≤ 0.13	≤ 0.3	≤ 0.46
`f1`	≥ 0.005	≥ 0.005	≥ 0.005
`deltae` (`e2tsts1-emins1`)	≤ 100	≤ 140	≤ 200
`wtots1`	< 2.15	< 1.3	< 2.3
`fracs1`	< 0.262	< 0.180	< 0.250
`weta1`	< 0.65	< 0.62	< 0.66

table 7.3, where selection efficiencies of 85% are achieved with very high background rejection. The signal efficiency is similar for both samples tested, but the background rejection is larger in the combined sample. This is due to jets in direct photon events mainly coming from quark jets (as $qg \rightarrow \gamma q$ dominates), whereas the di-jet events in the combined sample mainly produce jets from gluons (as $gg \rightarrow gg$ dominates), for which the rejection is larger. These cuts can also be relaxed for background studies, as discussed in section 7.6.5.

Table 7.3: Results from applying isEM to the combined and direct photon samples for $p_{\mathrm{T}}^{\gamma} > 25$ GeV [5]. The rejection of backgrounds from jets (including any jets in direct photon events) and the efficiency for reconstructing truth photons are compared.

Data sample	Combined	γ+jet
Efficiency	84.6±0.2	84.5±0.2
Rejection	8240±270	1940±230

7.6.4 Isolation

The term isolation refers to the amount of energy around the particle of interest, as already discussed in section 6.5.1. This can come from the underlying event, or from the hard interaction itself in the case of a mis-identification. At LO, a direct photon may have energy nearby from the proton remnant or other underlying event effects, whereas a π^0 in a jet identified as a photon will generally have energy nearby from the remainder of the jet. Also a real photon can be radiated at a wide angle (the Bremsstrahlung process as discussed in section 5.3). Isolation is used to define the cross-section at the theoretical level and is the basis of the selection at the reconstructed level. Inevitably the cross-section then contains contributions for both LO direct photons and Bremsstrahlung photons.

Several variables are already included in the isEM definition to select on the

basis of the isolation. In the first layer, as described in section 7.6.2, there is the `fracs1` variable and there are also the ratios, in table 7.2, looking at the width in the second layer. To make full use of all four layers (including the presampler) there is another ratio ($e33/e37$) of cells. These variables are useful for detector level cuts, but are hard to relate to a generator level definition. Instead a better solution is to use a cone around the centre of the reconstructed particle. Different radii of cones can be selected for different purposes. The cone is defined in $\eta\phi$ space, and its radius is denoted by ΔR. Setting this cone size requires a careful choice: if it is too large then too much underlying event or detector noise can be included in the cone, but if it is too small then it can be smaller than the wider showers from high energy photons. It is usually preferred to have a larger cone size (typically at the Tevatron cone sizes between 0.4 and 1.0 are used) and to try to understand as well as possible the effects from the underlying event and detector noise.

Technical problems with the isolation cone in ATHENA releases 12 and 13, meant that a cone of $\Delta R = 0.2$ is the only size used in this study, via the variable `etcone20`. As with isEM, the isolation cut could have different criteria for different ranges of photon p_{T}. However it is simpler, both technically and theoretically, to have a cut that scales directly with the p_{T} of the photon candidate (as with `iso` in table 7.2). The distribution in this variable for all reconstructed photons is shown in figure 7.4. The reconstructed photons are classed as signal if they are matched to a LO or Bremsstrahlung photon with $p_{\mathrm{T}} > 20$ GeV and $|\eta| < 2.5$, otherwise they are counted as background. This shows that applying a cut at 0.1 picks out most of the direct photon events whilst rejecting the bulk of the background, which agrees well with the corresponding distributions at the generator level in section 6.5.1.

7.6.5 Data driven background estimation

The Monte-Carlo should be reasonably accurate at predicting the cross-section for one process relative to another, provided each has the same choices of scales, PDFs,

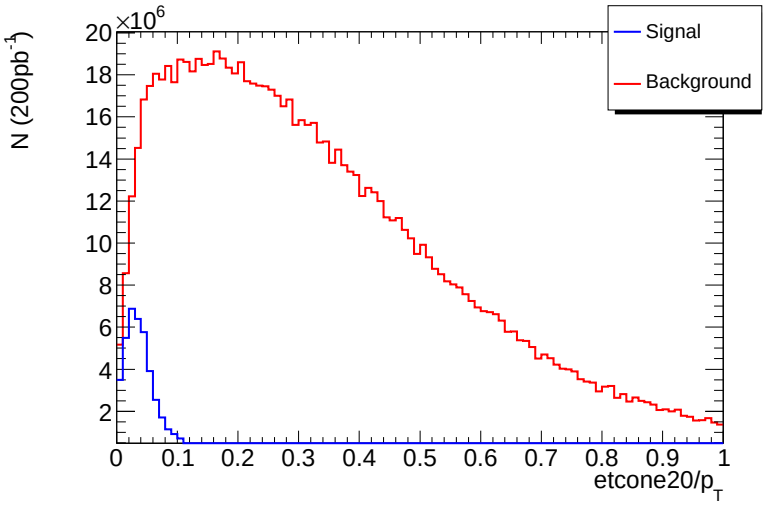

Figure 7.4: Isolation (`iso`) of all reconstructed photons, see text for details.

etc. However the overall normalisation of the cross-section of a process could well be wrong as there have never been collisions near the energy of the LHC before, meaning that any small errors in the results from previous data will become larger when extrapolated to the LHC. Therefore relying on Monte-Carlo simulations to set the normalisation of the background is subject to large uncertainties. The isolation variable used in figure 7.4 is actually mentioned above in the isEM selection, but is set to never be applied. As this variable is unused by the photon isEM optimised selection, it could be used to estimate the amount of background directly from data taken by ATLAS, removing the reliance on the Monte-Carlo. As shown in figure 7.5, the shapes of the `iso` isolation variable are different for background and signal even after the isEM selection has been applied. The corresponding distribution in data could then be fitted with these shapes as templates, to create an estimator for the relative amounts of signal and background present. This method would still rely on taking the shapes from Monte-Carlo, but these could be verified from data by looking at electron showers.

As already described in section 7.6.4 isolation is useful in matching the reconstructed cross-section to that at the generator level. So instead of using isolation to

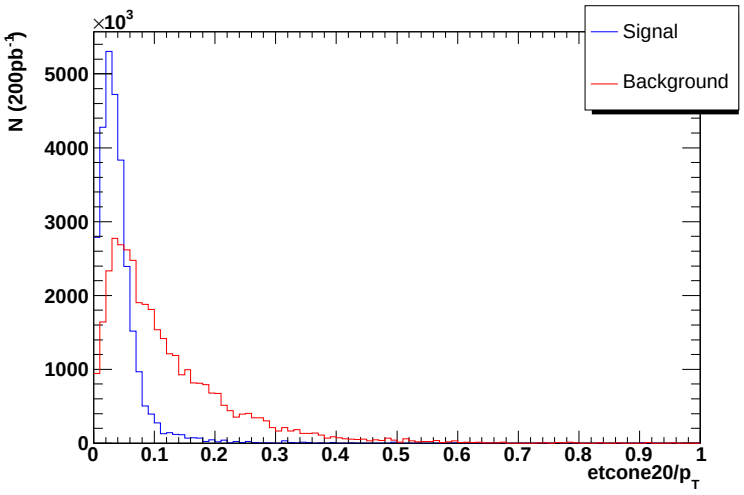

Figure 7.5: Isolation (`iso`) of reconstructed photons as in figure 7.4 but now after the photon isEM selection has been applied.

determine the background fraction, similar procedures can be followed by removing some of the variables from the isEM selection. The distributions in these removed variables can then be fitted to estimate the signal and background fraction in a data sample. In the isEM selection the cuts on the hadronic leakage (`hadleakage`) and the second layer cuts (`e277`, `ratio1`, `ratio2` and `weta2`) will reduce the background to almost entirely photons from π^0 decays. These are the main source of the background after the full isEM selection. So not applying the remaining cuts (all from the first layer), which remove most of these fakes, will yield a mixed sample of photons and pions, the normalisation of which can be controlled by looking at the first layer variables. Figure 7.6 shows the distributions of the remaining first layer isEM variables after the subset of isEM cuts has been applied. This shows that there is plenty of scope for finding the amount background by using this subset[†] of isEM, as several of the variables (e.g. `deltae`) have large differences between the shapes of the signal and background distributions. To be able to use this subset method of background evaluation effectively it would also have to be applied at the trigger

[†]At the time of writing a "medium" isEM selection for photons was being developed (to add to the full "tight" isEM selection), which was similar to the ideas behind the subset discussed here.

level, otherwise the high level triggers would bias these distributions.

7.6.6 Selection summary

In the final analysis (chapter 8) the cuts that will be applied to select the best reconstructed photons are the full isEM selection, for removing fake photons from jets, and also the isolation cut `etcone20`/p_{T}, which is not only useful in selecting events but is well matched to that used in the definition of the cross-section at the hadron level. These cuts make up the offline selection, which will be applied to events which have passed the g20 trigger item.

7.7 Jet Reconstruction

This analysis does not have any selection based on the jet(s) in the event. This would have to be revisited to be able to carry out the gluon PDF study, from section 5.6, as the η of the jet is required, as shown in section 6.3.1. The most logical additional selection for this would be to find a single jet back-to-back with the photon. At first sight, this would also seem perfect to remove Bremsstrahlung events, which would have another jet near to the photon. However NLO direct photon events with QCD radiation would create extra jets and so fail a back-to-back selection. This would mean that the final selection would include LO and Bremsstrahlung events, which would complicate the procedure for estimating the number of LO Compton process events, required to study the gluon PDF.

To reconstruct jets an algorithm is applied to energy deposits in the calorimeter. The chosen algorithm should be fast, easy to calibrate and well understood theoretically. ATLAS, as other experiments, formerly used two algorithms: Cone and k_t [84–86]. The Cone algorithm creates a sum of energy inside a cone in $\eta\phi$ space, whereas the k_t algorithm iteratively merges deposits closest together in 3-

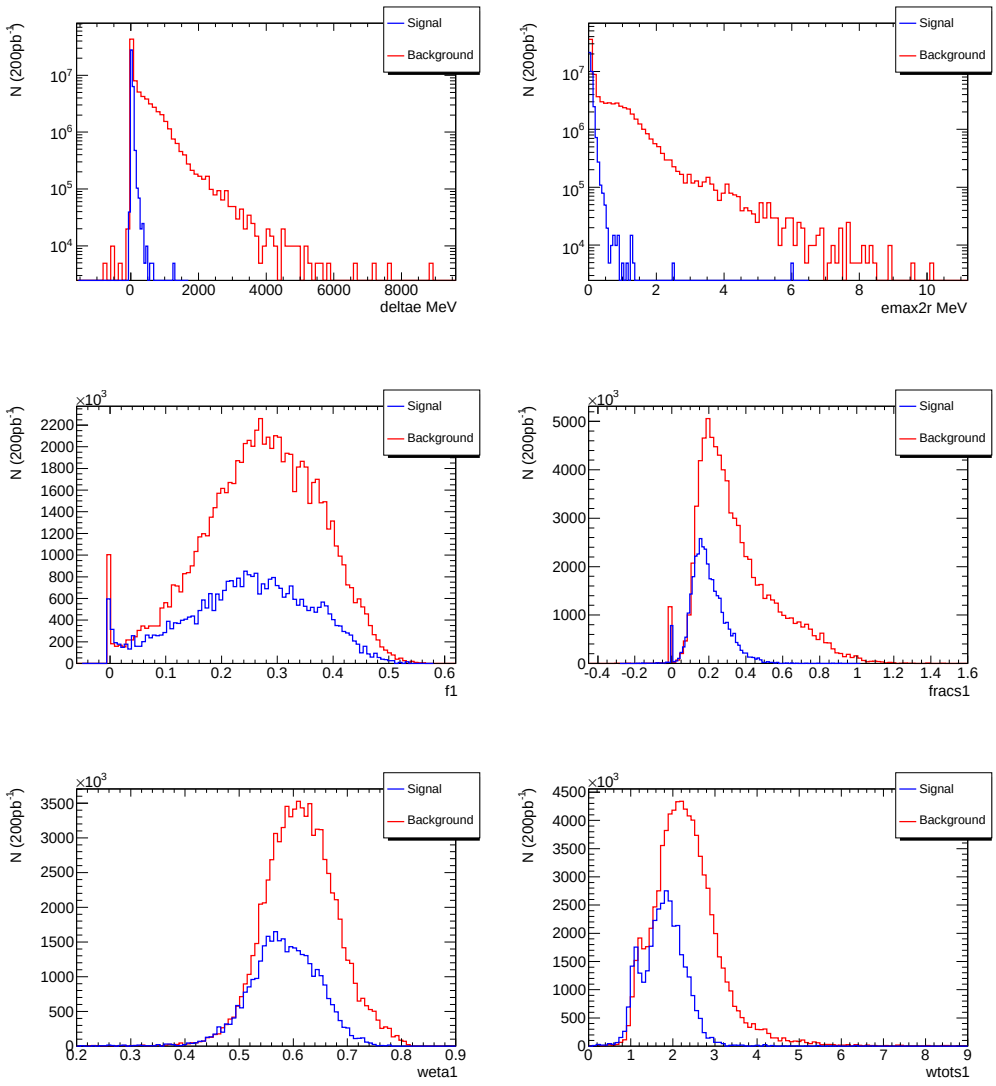

Figure 7.6: Distributions of all first layer variables not included when only a subset of isEM cuts, based on second layer quantities and hadronic leakage, is applied. See text for details.

momentum. The k_t algorithm is favoured as it is safer on a theoretical level, it avoids problems with jets splitting and soft radiation as discussed in [87]. In the latest releases of the ATLAS software new theoretically safe algorithms have become available: anti-k_t [88] and SIScone [89]. Of these the anti-k_t has been chosen as the ATLAS default jet algorithm. However, even with this choice of algorithm, there will initially be a large uncertainty on the jet energy due to not having a precise knowledge of the energy response of the calorimeter. Understanding this scaling, the JES, requires accurate calibration as discussed in section 5.6.

7.8 Alternative Cuts

The chosen selection cuts concentrate on information from the EM calorimeter. One possible expansion to improve this could be to use information from the inner detector to help with isolation studies. A technically simple method to achieve this would be to find a jet reconstructed around the photon (as the same calorimeter deposits can be reconstructed as both a photon and a jet) and find the number of tracks associated to this jet[†]. As shown in figure 7.7 this could be a useful cut before any selection is applied, but after applying the isEM and isolation cuts the signal (again defined as a reconstructed photon matching to a LO or Bremsstrahlung photon with $p_{\mathrm{T}} > 20$ GeV and $|\eta| < 2.5$) and background distributions are already similar and not much is gained by adding this selection requirement. Also shown in figure 7.7 is the missing transverse energy, $E_{\mathrm{T}}^{\mathrm{miss}}$, (calculated from all parts of the calorimeters), which although not showing any difference between signal the background distributions may be important when considering backgrounds other than those from di-jets, as discussed in the context of photon+jet measurements at DØ [79].

[†]For this analysis a k_t jet with distance parameter of 0.6 was used.

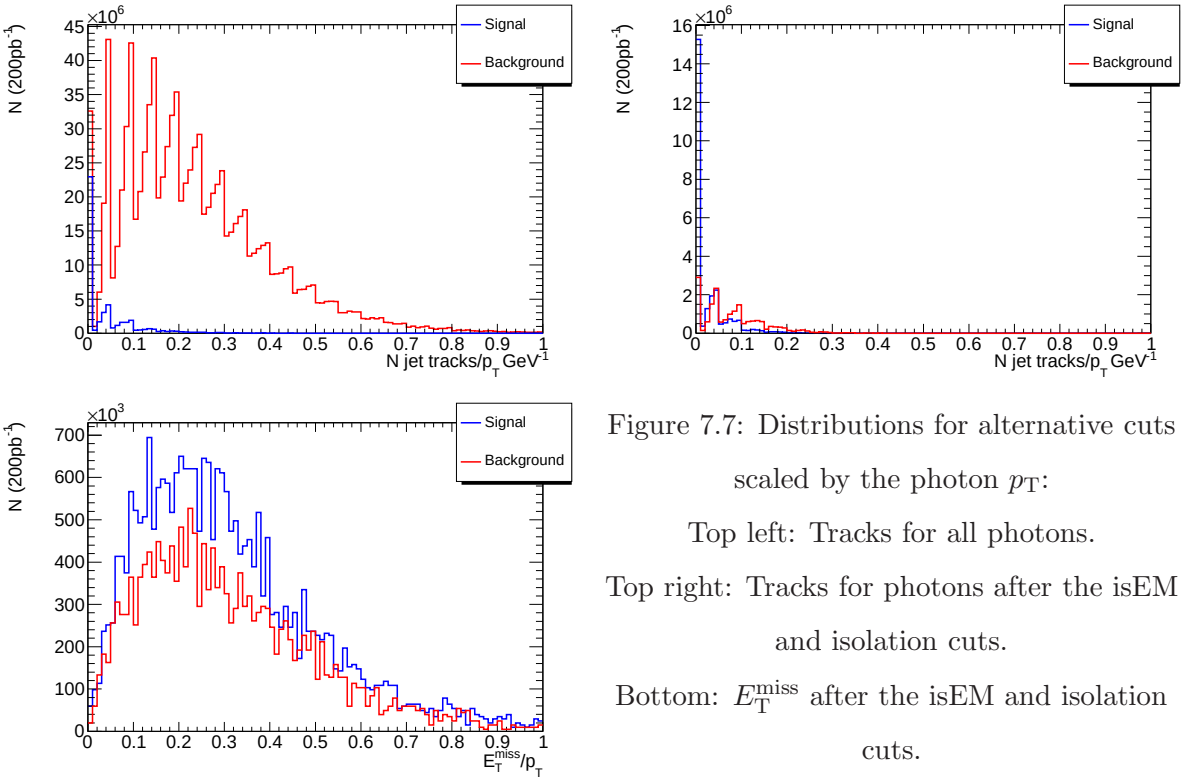

Figure 7.7: Distributions for alternative cuts scaled by the photon p_{T}:
Top left: Tracks for all photons.
Top right: Tracks for photons after the isEM and isolation cuts.
Bottom: $E_{\mathrm{T}}^{\mathrm{miss}}$ after the isEM and isolation cuts.

Chapter 8

Direct Photon Cross-section Measurement

8.1 Introduction

Laid out in this chapter is a procedure to measure an inclusive isolated photon cross-section for photons not originating from hadronisation (i.e. photons produced from meson decay are excluded). The criteria to select events are described in chapters 6 and 7 and are summarised in figure 8.1. The following sections give further details, as well as the values obtained for efficiency and background contamination. Finally the accuracy of the measurement is studied by looking at the achievable statistical and systematic errors.

8.2 Cross-section Definition

The p_{T} and η requirements for the cross-section definition are defined by experimental issues. As discussed in section 7.5 the selected trigger item is g20, which

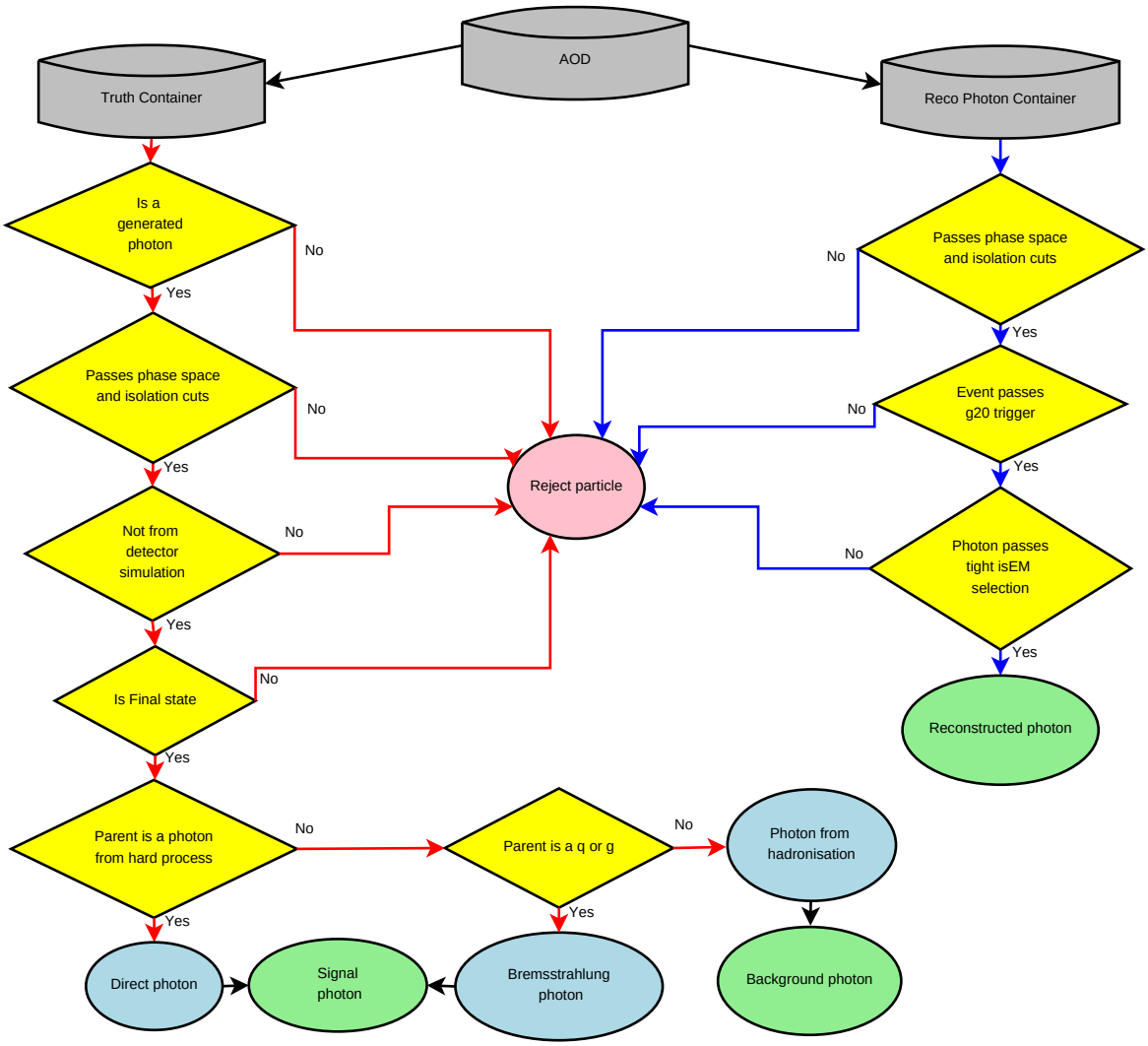

Figure 8.1: Flowchart showing the selection procedure for photons in the Monte-Carlo simulation study, starting from generated/simulated level (Truth Container) and the reconstructed level (Photon Container) contained in an AOD (from simulation or real data).

requires a minimum p_{T} of 20 GeV for a photon candidate. Due to the η range of the Inner Detector (see section 5.2), photons can only be reliably identified for $|\eta| < 2.5$. This phase space studied is the same at both the generator level and after reconstruction, although events are generated outside this region to account for smearing and bin migrations. Using this phase space definition, figure 8.2a shows the number of events containing one or more LO direct photons, Bremsstrahlung photons and hadronisation photons (i.e. photons produced from meson decay inside a jet), scaled to the planned integrated luminosity of 200 pb^{-1} of the LHCs initial run[†]. The chosen binning in p_{T} is explained in section 8.3.

In order to be a well defined physical observable, the cross-section must be defined in terms of hadron level observables. To relate the cross-section as closely as possible to the non-directly observable concept of direct photons, an isolation requirement is included in the cross-section definition, which will select most of the events which are generated as direct photons and will reject most photons from jets. The isolation criteria used, as discussed in sections 6.5.1 and 7.6.4, requires that the transverse energy in a cone of radius 0.2 (minus the photon energy) around the photon must be less than 10% of the photon p_{T}. Figure 8.2b shows that after applying the isolation requirement the majority of direct photon and Bremsstrahlung events pass this selection, whilst the number of photons from fragmentation in jets that pass this selection is significantly reduced.

This analysis is primarily interested in selecting photons directly from the hard process, rather than any originating from hadronisation. So from this point onwards, the small fraction of events from hadronisation that pass the truth level selection are considered as background. Therefore, after applying the phase space and isolation selections, the signal selection is completed by selecting the highest p_{T} photon that is either a LO direct photon or Bremsstrahlung photon. This truth level selection is then used in Pythia to create the differential cross-section in p_{T} as shown in

[†]As stated previously, section 2.3, this initial run will not be at the 14 TeV used in this study.

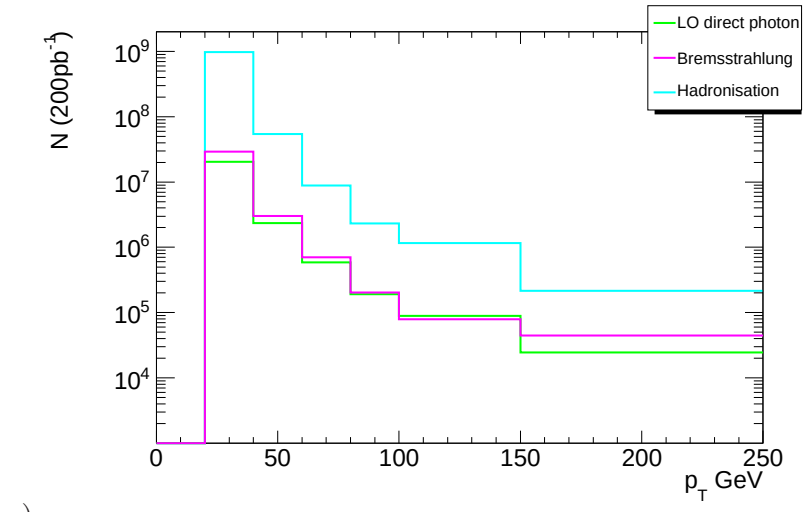

a)

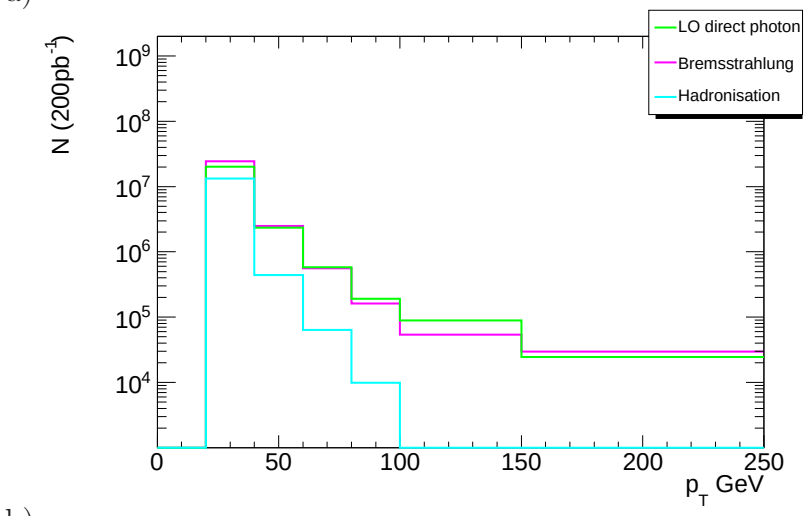

b)

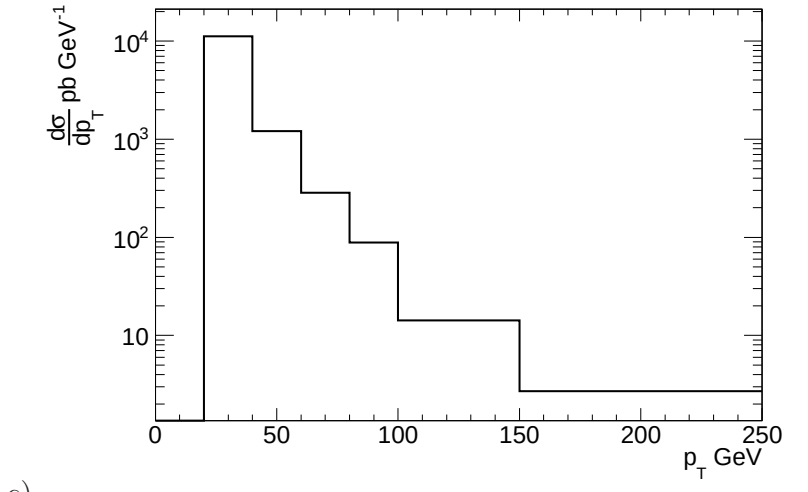

c)

Figure 8.2: Number of photons at the generator level passing a) the phase space selection and b) the isolation selection in addition. After these selections c) the cross-section from Pythia is created from the highest p_{T} LO direct photon or Bremsstrahlung photon.

figure 8.2c. Integrating this gives a cross-section of 256 nb for Pythia. The result from Pythia, consisting of LO direct photons and Bremsstrahlung photons from the parton shower, is approximately 20% higher than the NLO result of 214 nb predicted by JetPhox, see section 6.6.2.

8.3 Reconstruction Selection

The selection of a reconstructed photon is described in section 7.6. The highest p_{T} reconstructed photon is then selected after applying the same phase space and isolation cuts as at the truth level. This reconstructed photon is then matched to find the nearest truth photon passing the phase space and isolation cuts and lying within a cone of radius 0.2 around the reconstructed photon. If the nearest truth photon in ΔR is a LO or Bremsstrahlung photon the event is counted as signal. If the nearest is a hadronisation photon or there is no truth photon inside the cone that passes the phase space and isolation criteria, then the event is counted as background.

To be able to see the how many of the reconstructed events are signal events, a purity is defined as:

$$reconstruction\ purity = \frac{Number\ reconstructed\ and\ classed\ as\ signal}{Number\ reconstructed} \tag{8.1}$$

This is calculated on a bin by bin basis (not accounting for any bin migrations) and is shown in figure 8.3a after the phase space and isolation selection. At this stage, the background dominates. To improve the signal selection the isEM selection, as described in section 7.6.1, can be applied to keep events with only the best photon candidates. The sample then has a reconstruction purity, as shown in figure 8.3c, approaching 80% after the full isEM selection is applied. Importantly figure 8.3b shows that there is nearly a 20% difference between the purity from the subset of isEM requirements (as defined in section 7.6.5) and the full selection, meaning that this subset will be appropriate for estimating the background directly from data.

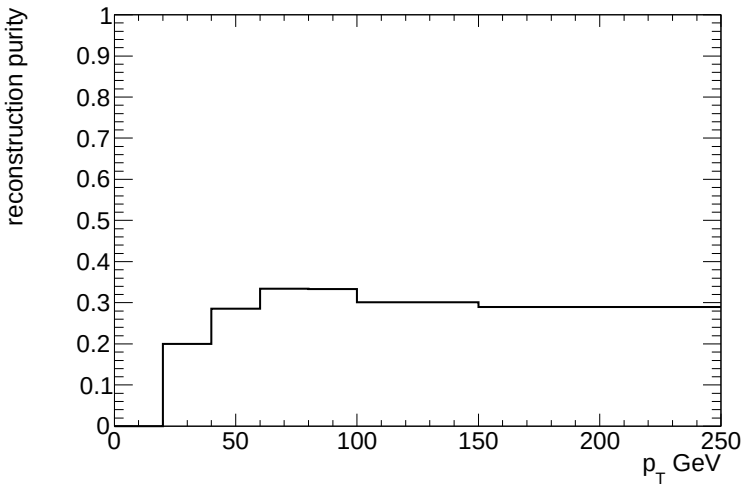

a)

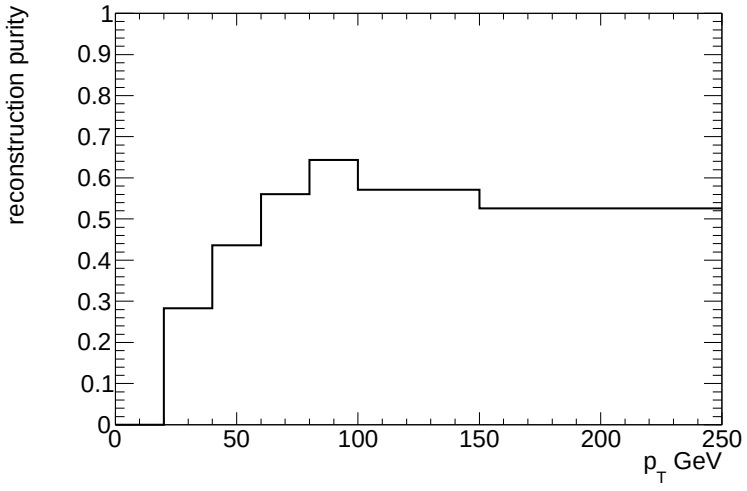

b)

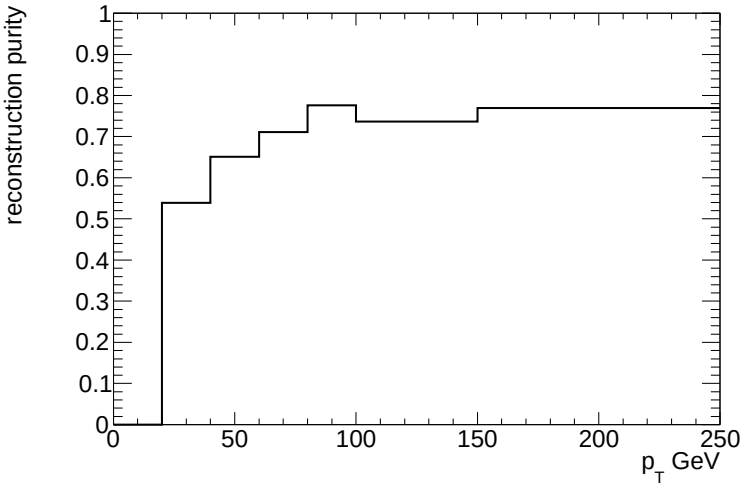

c)

Figure 8.3: Reconstruction purity after applying the selections: a) the phase space and isolation cuts, b) the subset of isEM requirements defined in section 7.6.5 and c) the full set of isEM requirements.

Not all events which are part of the cross-section definition will pass the g20 trigger. Comparing figures 8.3c and 8.4a results in a slightly improved purity, improved by 5% in the first bin and by $\sim 1\%$ in the later bins, which shows that the trigger selection is very similar to the full isEM selection.

After applying the trigger requirement all the reconstruction cuts have been applied. Figure 8.4b shows the number of events this set of requirements selects for 200 pb^{-1}: 21 million signal events in the first bin, reducing to 49 thousand in the last. Figure 8.4c then shows how this final selection of reconstructed signal events compares to the generator level cross-section definition in figure 8.2. This reconstruction efficiency for signal events is calculated for each bin (again not including any migration effects) by:

$$signal\ reconstruction\ efficiency = \frac{Number\ of\ signal\ reconstructed}{Number\ of\ signal\ generated} \tag{8.2}$$

This increases with photon p_{T}, and reaches the value from [5] in table 7.3. Once data has been taken by the experiment the differential cross-section will be calculated via equation 8.3, using the signal reconstruction efficiency and number of background events found above (denoted ϵ_{signal} and $N_{background}$ respectively).

$$\frac{d\sigma}{dp_{\mathrm{T}}} = \frac{N_{data} - N_{background}}{L \times \epsilon_{signal} \times \Delta p_{\mathrm{T}}} \tag{8.3}$$

As discussed in section 2.6.1, many photons will convert inside the detector before reaching the calorimeter. Flags, see section 7.6.2, are set if the photon is reconstructed as coming from a conversion. By asking for either of these flags to be true, it can be seen, figure 8.5, that in the final selection, around 10% of the reconstructed photons are from conversions, for both signal and background. This is the result without using any conversion recovery tools, which could increase the final signal selection efficiency.

The binning chosen in the plots in this chapter is not arbitrary. It is determined by the limited Monte-Carlo statistics available and leads to only small migrations

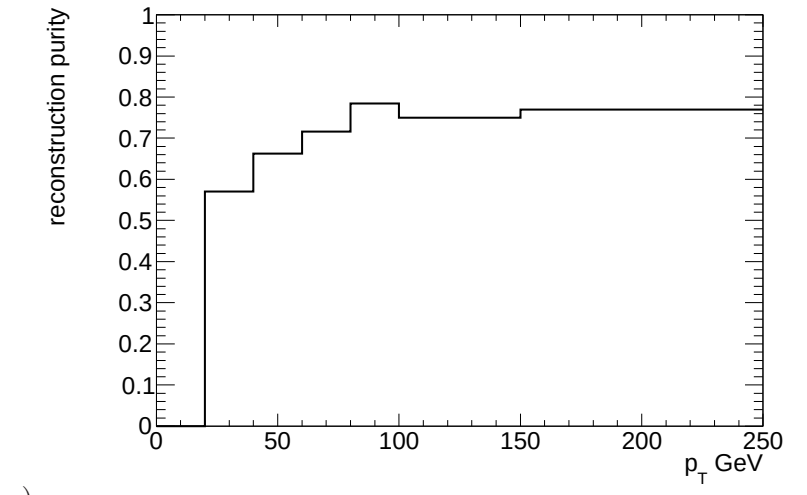

a)

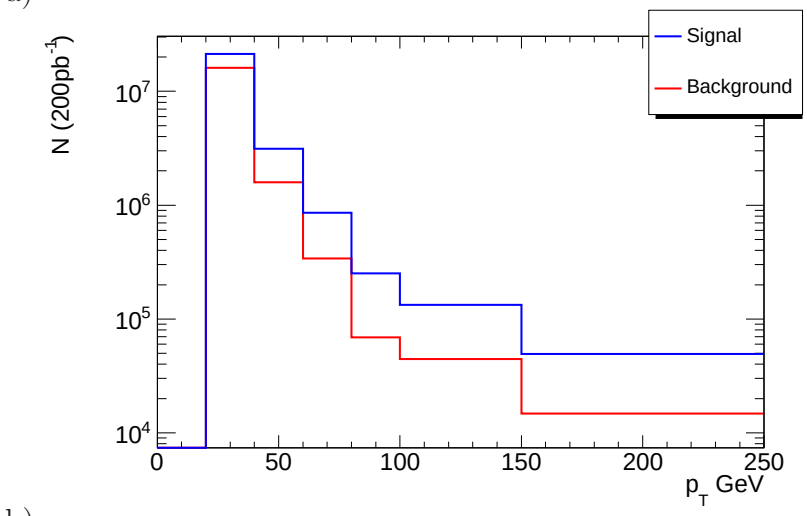

b)

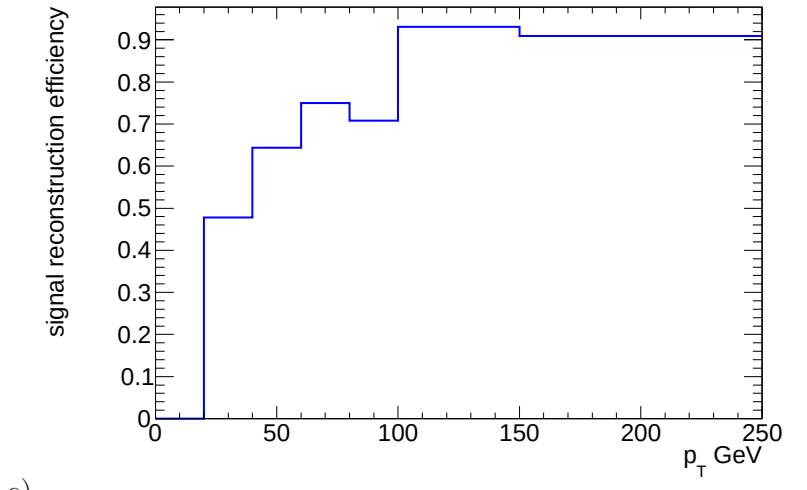

c)

Figure 8.4: Results for a) reconstruction purity b) number of events and c) signal reconstruction efficiency after adding the g20 trigger to the reconstruction selection, creating the final reconstruction selection.

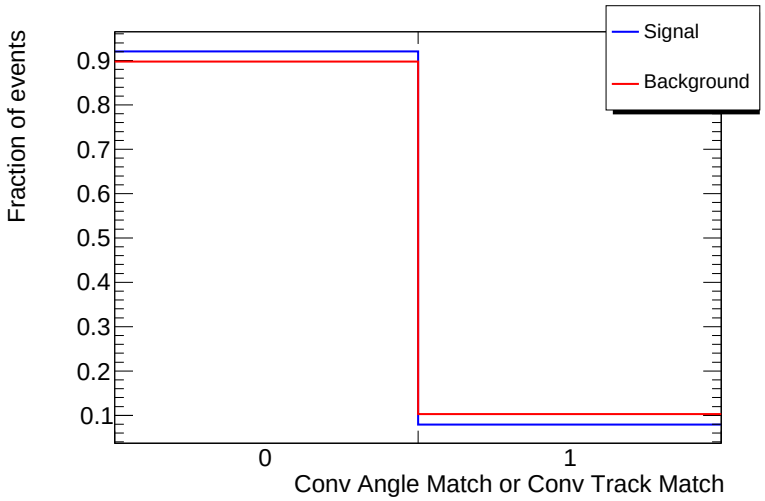

Figure 8.5: Fraction of reconstructed photons arising from conversions in the final selection.

of signal events between bins. This is quantified using a different purity definition to that in the above plots. It is defined as:

$$signal\,bin\,purity = \frac{Number\ of\ signal\ reconstructed\ and\ generated\ in\ bin}{Number\ of\ signal\ reconstructed\ in\ bin} \quad (8.4)$$

and, as shown in figure 8.6, each reconstructed bin contains over 80% of the photons that were also generated in the same bin. The size of the sample used is documented in section 7.4. After the final selection table 8.1 shows the statistical errors ($\frac{\sqrt{N_{signal}+N_{background}}}{N_{signal}+N_{background}}$) on the raw number of events, which are large in the final bins even with large bin sizes. With sufficient Monte-Carlo statistics a finer binning, and also differential studies in η as well as p_{T}, would have been possible. The statistical uncertainties on the cross-sections measured with a sample of 200 pb^{-1} will be negligible (see table 8.2).

Table 8.1: Percentage statistical errors on the predicted Pythia cross-sections calculated from the raw number of Monte-Carlo events before applying luminosity based weights.

p_{T} bin (GeV)	20-40	40-60	60-80	80-100	100-150	150-250
Statistical error	1.15	3.23	6.42	12.40	16.67	27.74

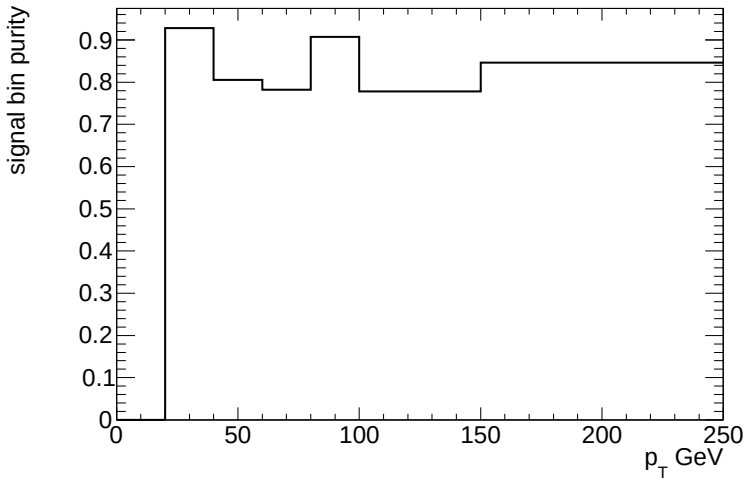

Figure 8.6: Signal bin purity.

8.4 Systematic Errors

In this section, the achievable systematic precision is assessed. From the detector there is no systematic effect from azimuthal misalignment, as the measurement is independent of ϕ. As the measurement is purely based on the reconstruction of the photon there are no jet uncertainties, which would need to be included to be able to expand this study to look at the gluon PDF as a function of x_{gluon}. For the measurement described the main sources of uncertainty are discussed below.

8.4.1 Luminosity.

The uncertainty on the luminosity is likely to be one of the largest contributions to the systematic error. The estimate is that it will be known to around 10%, although this may be optimistic in early data [90]. This is possible through monitoring the rate measurement of well known QCD processes, i.e. W and Z bosons, whereas calculating the error directly from the LHC machine parameters returns an error larger by a factor of $\sim 2-3$.

8.4.2 Trigger efficiency.

In comparison the error on the trigger efficiency is expected to be minimal. As discussed in section 7.5, nearly 100% of photons that pass the offline selection will pass the trigger requirements, as the trigger is just based on a looser selection of the offline cuts. Any threshold effects (see the turn-on curves in figures 7.2 and 8.4c) should also not affect the offline result and can be checked from data by using a (prescaled) lower p_{T} trigger. So any error will be most likely be negligible compared with the offline selection (i.e. the identification efficiency error in section 8.4.7).

8.4.3 η misalignment.

Similarly any error from η misalignment will be negligible for the phase space selection, due to the large bin in η. It may affect the simulated efficiency of the isEM selection to some extent, as its cuts are binned in η, but this error is handled by the separate error for identification efficiency, see section 8.4.7.

8.4.4 Photon energy scale.

For the photon energy scale, the reconstructed photon distribution can be varied relative to the truth level distribution to see the effect on the final cross-section distribution. The chosen value to vary by was 2%, as quoted in [1]. Varying the energy scale creates new predictions for $N_{background}$ and ϵ_{signal} to use in equation 8.3, with N_{data} coming from the sum of background and signal events from the default (i.e. no variation) selection. This results in an error of $\sim 5\%$, as shown in figure 8.7. The statistical fluctuations are a consequence of the limited available Monte-Carlo statistics.

8.4.5 Isolation requirements.

Following the same procedure as for the photon energy scale, the amount of energy in the isolation cone can be varied, although this time by a larger amount of 10%. This 10% reflects the accuracy of the JES measurement [1], which is a similar uncertainty for energy measurement in the calorimeters. As above this results in an error of $\sim 5\%$, again shown in figure 8.7 and once more is subject to large statistical fluctuations.

8.4.6 Background normalisation.

An accurate measurement of the background contamination of the sample directly from data will be key to reducing the large uncertainty from the error on the background normalisation. An example of a data-driven purity measurement is described in section 7.6.5, but these methods are only useful once sufficient data has been taken. For now a reasonable estimate of the background normalisation uncertainty is to take the current precision on the predicted di-jet cross-section. Following the procedure and values in [91], it can be seen that the di-jet NLO cross-section prediction is 477μb whereas LO is 367μb, which corresponds to a difference of 25%. As above, this 25% is used to create new predictions for $N_{background}$, which are then fed into equation 8.3 producing errors decreasing from 20% to 8% with increasing p_{T}, as shown in figure 8.7.

The error on the background normalisation gives an estimate on the amount of events that could produce background photons. However, the error from the modelling of hadronisation is more closely linked to the number of background events in this study. This is because the hadronisation model alters the mesons produced, which then alters the amount of mesons that decay into photons. Similarly it could also effect the isolation of the photons produced. The best method would be to repeat this analysis with other generators with different hadronisation models. Unfortunately no matching analysis sample of similar statistics was available to carry out such a comparison, so only the above error on the background normalisation is used. Repeating this analysis in a later release of the ATLAS offline software would make this comparison possible.

8.4.7 Photon identification efficiency.

Obtaining the identification efficiency error for a photon from data is complicated as there are few channels where it is easy to know for sure that you have reconstructed

a photon. An example is $Z \rightarrow \mu\mu\gamma$ which is hampered by having a low cross-section. However the error on the photon identification can be roughly estimated by comparison with that for an electron. An error of $1 \sim 2\%$ [5] can be achieved on electron identification, using $Z \rightarrow ee$ events, but relating this to photons will result in a larger error, more likely to be around 5%. Varying the amount of events that pass the selection, both background and signal, by 5% again creates new predictions for $N_{background}$ and ϵ_{signal} to be fed yet again into equation 8.3, producing an error of $\sim 7\%$ as shown in figure 8.7. The 5% level of accuracy on photon identification can be obtained independently by studying the effect of changing the photon selection used. As documented in [5] the same photon variables used in a cut-based way to create the isEM selection can be used instead as part of a likelihood technique. As shown in [1] this can achieve an improvement of 6% on the background rejection for the same signal efficiency. Another study of the isEM variables (in appendix E) also yields similar results.

8.4.8 Total Systematic Error

The systematic errors for each source are summarised in figure 8.7. The absolute value of each error from the shifts up and down are averaged to create symmetric errors, which are then added in quadrature to create the total error. Despite the clear need for better Monte-Carlo statistics, the plot shows that at low p_{T} the background normalisation is the largest contribution to the total systematic, but as p_{T} increases the luminosity error becomes the largest contribution, creating a total error that ranges between 15 and 20%.

This level of uncertainty will need to be greatly improved for precision measurements to be made. The systematics quoted are all for the first run of the LHC. As described in [1], in later running the electron (and hence photon) energy scale precision may reduce to 0.02% and the jet energy scale to 1%. Also in later running the electron identification efficiency error should improve to below 1% and similarly

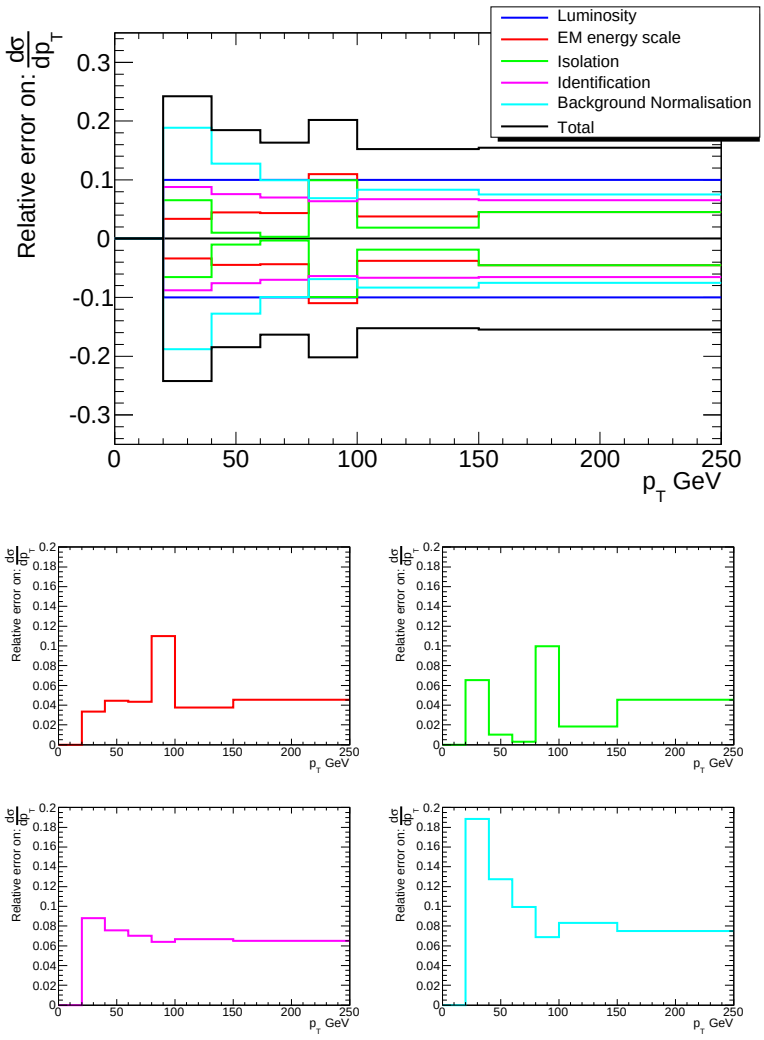

Figure 8.7: Relative sizes of the averaged shifts for each systematic error (top). Also, for clarity, several errors are shown individually (below). See text for more details.

the error on the photon identification efficiency should be significantly reduced after $Z \rightarrow \mu\mu\gamma$ measurements take place. The error on the background normalisation is rather large and should be greatly reduced after the first di-jet measurements and further by data-driven photon purity measurements. For the luminosity even though it may reduce to 5%, or even 3% [90] with the help of the ALFA detector (described in section 2.8), it may remain the largest contribution to the error in later running. Since it influences the cross-section in a manner which is 100% correlated between data points, this will not affect the understanding of the p_{T} or η distributions.

8.5 Cross-section Summary

In addition to the systematic errors on the final cross-section there are also statistical errors to consider. The statistical error is calculated based on N_{data}, i.e the sum of signal and background in figure 8.4b, used in equation 8.3. In total there are 43 million events expected, which gives a fractional error of $(\frac{\sqrt{N_{data}}}{N_{data}})^{\dagger}$ 0.02% overall. When looking at the binned distribution this error will be largest for the high p_{T} bins. However even the highest bin has 64 thousand events, giving an error of 0.4%, which is low because of the bin size chosen (as descried earlier in section 8.3).

Figure 8.8 shows the final simulated cross-section measurement defined for a real photon, either via the LO direct or Bremsstrahlung processes, with ${p_{\mathrm{T}}}^{\gamma} > 20$ GeV, $|\eta| < 2.5$ and $isolation^{\ddagger} < 0.1 \times {p_{\mathrm{T}}}^{\gamma}$, with the systematic and statistical errors shown for a luminosity of 200 pb^{-1}. This shows that systematic errors are heavily dominant, even with the statistical errors being scaled by a factor of 10 to improve visibility. The central values of the cross-section shown are from Pythia. Also shown is the differential cross-section from JetPhox, from section 6.6.2. Table 8.2 shows the

†From equation 8.3 the statistical error on the cross-section should be $\frac{\sqrt{N_{data}}}{N_{data}-N_{background}}$ but as $N_{background}$ is small the difference between this and $\frac{\sqrt{N_{data}}}{N_{data}}$ is negligible.

‡Transverse energy in a cone of $\Delta R = 0.2$ minus the photon energy.

cross-section integrated over each bin, along with statistical and systematic errors, which when combined gives a total cross-section of: 255.7±59.9(syst)±0.1(stat) nb.

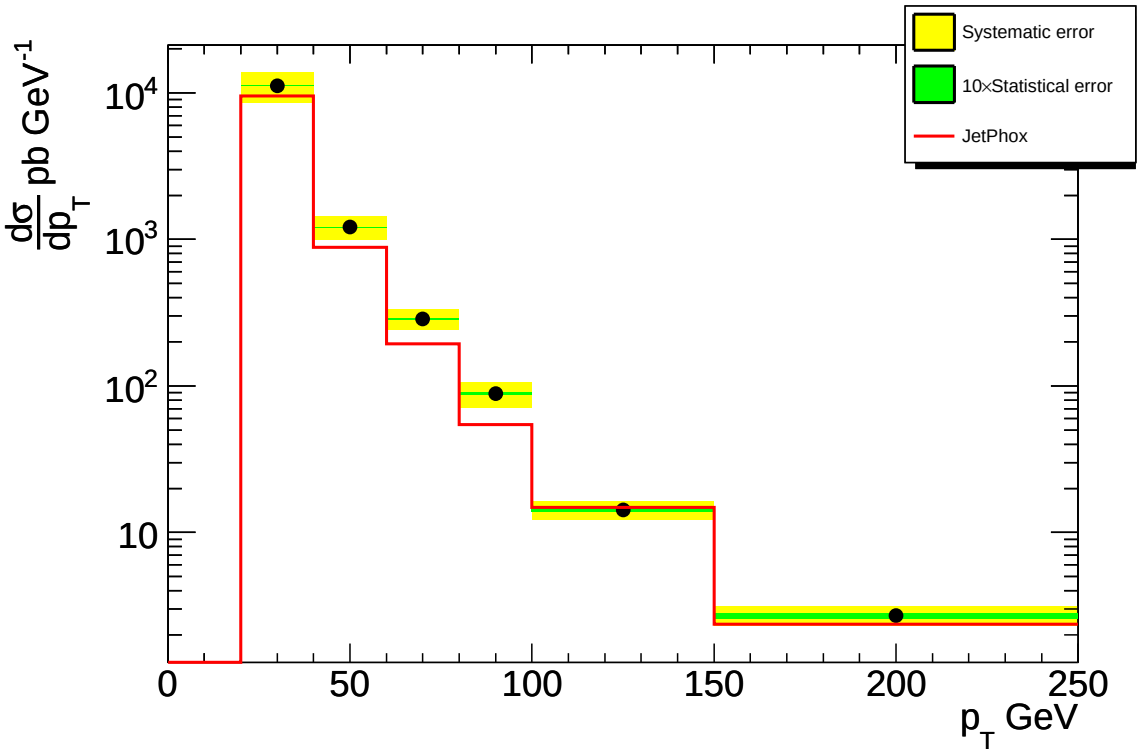

Figure 8.8: Differential cross-section data points from Pythia with systematic and statistical (×10) errors.

8.6 Next Steps

This chapter outlines a possible selection for an inclusive isolated photon measurement. However, the analysis would need several improvements before this process can be fully utilised. The main change would be increasing the size of the isolation cone around the photon. This would allow a higher E_{T} cut to be used, to make the isolation energy less sensitive to the influence of noise and the underlying event. The analysis would also have to be expanded, as already outlined in section 7.7, to include a jet selection to be able to reconstruct the momentum fraction, x, for

Table 8.2: Integrated cross-section in each bin, along with statistical and systematic errors.

p_{T} bin (GeV)	σ (nb)	Statistical error (nb)	Systematic error (nb)
20-40	223.00	0.04	53.99
40-60	24.26	0.01	4.48
60-80	5.71	0.01	0.93
80-100	1.773	0.003	0.358
100-150	0.714	0.002	0.109
150-250	0.271	0.001	0.042

studies of the gluon PDF. Matters are complicated by the Bremsstrahlung source of isolated photons, which would have to be well understood before PDF or underlying event studies could be carried out. Similarly studies using the subset of the isEM selection would need to be carried out to create estimators for the number of background events. The systematic errors considered should cover all main sources of error on this measurement except that when the LHC approaches design luminosity there is also the effect of pile-up to be considered, which will affect energy and isolation measurements.

As described earlier this analysis is performed at $\sqrt{s} = 14$ TeV, which is higher than the planned energy of the first run at the LHC. Updating the analysis to the latest release of the ATLAS offline software would allow studies, on ATLAS centrally produced data, with centre of mass energies more likely to be achieved during the first LHC run, and would also then match the software that data is taken with. This would also resolve the problems with the g20 trigger (section 7.5), isolation cone size (section 7.6.4) and also would provide a more accurate error on the background normalisation (section 8.4.6). Similarly the NLO prediction from JetPhox should be updated to version JetPhox1.1, to investigate any differences in its prediction

but also to test more recent PDFs (a direct link to LHAPDF [92] is now available rather than using libraries internal to JetPhox). The final differential cross-section is limited by the statistics of the analysis sample, with increased statistics a finer p_{T} binning based on the photon resolution (i.e. down to a few GeV) could be achieved along with double differential cross-sections (in $p_{\mathrm{T}}\eta$ or $p_{\mathrm{T}}x_g$).

Summary

This thesis has discussed the preparations for making a direct photon cross-section measurement at ATLAS, with the first LHC data, and has also described the role, and development, of the Atlantis event display.

Atlantis has already proved itself useful within the collaboration, for example in the ATLAS control room, but its features are constantly being updated to improve the functionality for the user. The new features described here have been well tested but unforeseen problems can occur so continued support for the software is required. Further work on the use of openGL will help Atlantis to continue to be the pre-eminent event display within ATLAS. Atlantis has also now been extended to help educate a new generation of physicists and to explain to the general public what the research in ATLAS is all about, through the MINERVA project. This is extremely important and new developments for use in homes, schools and undergraduate laboratory experiments will help improve the outcomes of this software.

Direct photons are an interesting process at the LHC with many motivations for their study, including constraining the gluon PDF and tuning underlying event models once ATLAS takes its first data. With the simulated first cross-section measurement found here of $255.7 \pm 59.9(\text{syst}) \pm 0.1(\text{stat})$ nb, based on 200 pb^{-1}, there will be millions of events produced in the first year of LHC running. The systematic errors of above 15% will have to be significantly reduced before direct photons can realise their full potential, but this should be possible in later running. However,

the first data will give an insight into how accurate our current Monte-Carlo models are and will point the way towards further developments and measurements.

Bibliography

[1] G Aad et al. The ATLAS Collaboration, The ATLAS Experiment at the CERN Large Hadron Collider, *JINST* **3**(08), S08003 (2008).

[2] ATLAS Collaboration, ATLAS: Detector and physics performance technical design report. Volume 1, CERN-LHCC-99-14.

[3] ATLAS Collaboration, ATLAS detector and physics performance. Technical design report. Vol. 2, CERN-LHCC-99-15.

[4] Thomas Ivan Hollins, SCT hybrid testing and the production of direct photons in the ATLAS experiment at the LHC, CERN-THESIS-2007-061.

[5] G. Aad et al., Electrons and Photons, Expected Performance of the ATLAS Experiment - Detector, Trigger and Physics, (2009), 0901.0512.

[6] http://atlas.web.cern.ch/Atlas/public/EVTDISPLAY/events.html.

[7] S. L. Glashow, Partial Symmetries of Weak Interactions, *Nucl. Phys.* **22**, 579–588 (1961).

[8] Steven Weinberg, A Model of Leptons, *Phys. Rev. Lett.* **19**, 1264–1266 (1967).

[9] A. Salam, in: 'Elementary Particle Theory', W. Svartholm, ed., Almquist and Wiksell, Stockholm, 1968.

[10] H. David Politzer, RELIABLE PERTURBATIVE RESULTS FOR STRONG INTERACTIONS?, *Phys. Rev. Lett.* **30**, 1346–1349 (1973).

[11] D. J. Gross and Frank Wilczek, ULTRAVIOLET BEHAVIOR OF NON-ABELIAN GAUGE THEORIES, *Phys. Rev. Lett.* **30**, 1343–1346 (1973).

[12] Combination of CDF and DØ Results on the Mass of the Top Quark, (2009), 0903.2503.

[13] Enrique Palencia, Observation of Electroweak Single Top Quark Production at the Tevatron, (2009), 0905.4279.

[14] M. Ciuchini, M. Pierini, and L. Silvestrini, B/s $--> $ K(*)0 anti-K(*)0 decays: The golden channels for new physics searches, *Phys. Rev. Lett.* **100**, 031802 (2008), hep-ph/0703137.

[15] G. Aad et al., B-Physics, Expected Performance of the ATLAS Experiment - Detector, Trigger and Physics, (2009), 0901.0512.

[16] G. Aad et al., Standard Model, Expected Performance of the ATLAS Experiment - Detector, Trigger and Physics, (2009), 0901.0512.

[17] R. Barate et al., Search for the standard model Higgs boson at LEP, *Phys. Lett.* **B565**, 61–75 (2003), hep-ex/0306033.

[18] Combined CDF and DØ Upper Limits on Standard Model Higgs-Boson Production with up to 4.2 fb^{-1} of Data, (2009), 0903.4001.

[19] G. Aad et al., Higgs Boson, Expected Performance of the ATLAS Experiment - Detector, Trigger and Physics, (2009), 0901.0512.

[20] G. Aad et al., Supersymmetry, Expected Performance of the ATLAS Experiment - Detector, Trigger and Physics, (2009), 0901.0512.

[21] Project to prepare the PS Complex to be a Pre-injector for the LHC http://ps-div.web.cern.ch/ps-div/LHC PS/LHC-PS.html.

[22] https://twiki.cern.ch/twiki/bin/view/Atlas/PileupPerformance.

[23] Jean-Pierre Koutchouk and F Zimmermann, LHC Upgrade Scenarios. oai:cds.cern.ch:1203211, Technical Report sLHC-PROJECT-Report-0013. CERN-sLHC-PROJECT-Report-0013, CERN, Geneva, Jul 2009.

[24] LHC building website http://building.web.cern.ch/building/.

[25] Atlas public website http://atlasexperiment.org.

[26] A. Airapetian et al., ATLAS calorimeter performance, CERN-LHCC-96-40.

[27] R. Achenbach et al., The ATLAS level-1 calorimeter trigger, *JINST* **3**(03), P03001 (2008).

[28] H. Drevermann, D. Kuhn, and B. S. Nilsson, Event display: Can we see what we want to see?, Presented at the 1995 CERN School of Computing - CSC '95, Arles, France, 20 Aug - 2 Sep 1995: Proceedings / Ed. By C.E. Vandoni - CERN, Geneva, 1995.

[29] DALI higgs event from http://aleph.web.cern.ch/aleph/dali/dali_form.html.

[30] Open GL homepage http://www.opengl.org/.

[31] DØ event display D0VE:
http://www-d0.fnal.gov/d0dist/dist/packages/d0ve/devel/doc/
http://www d0.fnal.gov/computing/graphics/d0veall/d0vealldoc.html.

[32] ROOT homepage http://root.cern.ch/.

[33] Hypatia public homepage http://hypatia.phy.bg.ac.yu/.

[34] M. Bonesini et al., Production of High Transverse Momentum Prompt Photons and Neutral Pions in Proton Proton Interactions at 280-GeV/c, *Z. Phys.* **C38**, 371 (1988).

[35] G. Ballocchi et al., Direct photon cross sections in proton proton and antiproton proton interactions at $\sqrt{s} = 24.3$-GeV, *Phys. Lett.* **B436**, 222–230 (1998).

[36] L. Apanasevich et al., Evidence for parton k_T effects in high p_T particle production, *Phys. Rev. Lett.* **81**, 2642–2645 (1998), hep-ex/9711017.

[37] E. Anassontzis et al., High p(t) Direct Photon Production in p p Collisions, *Z. Phys.* **C13**, 277–289 (1982).

[38] C. Albajar et al., Direct Photon Production at the CERN Proton - anti-Proton Collider, *Phys. Lett.* **B209**, 385–396 (1988).

[39] A. L. S. Angelis et al., DIRECT PHOTON PRODUCTION AT THE CERN ISR, *Nucl. Phys.* **B327**, 541 (1989).

[40] J. Alitti et al., A Measurement of the direct photon production cross- section at the CERN anti-p p collider, *Phys. Lett.* **B263**, 544–550 (1991).

[41] B. Abbott et al., The isolated photon cross-section in $p\bar{p}$ collisions at $\sqrt{s} = 1.8$ TeV, *Phys. Rev. Lett.* **84**, 2786–2791 (2000), hep-ex/9912017.

[42] V. M. Abazov et al., The ratio of the isolated photon cross sections at $\sqrt{s} = 630$ GeV and 1800 GeV, *Phys. Rev. Lett.* **87**, 251805 (2001), hep-ex/0106026.

[43] Darin E. Acosta et al., Direct photon cross section with conversions at CDF, *Phys. Rev.* **D70**, 074008 (2004), hep-ex/0404022.

[44] Darin E. Acosta et al., Comparison of the isolated direct photon cross sections in $p\bar{p}$ collisions at $\sqrt{s} = 1.8$-TeV and $\sqrt{s} = 0.63$-TeV, *Phys. Rev.* **D65**, 112003 (2002), hep-ex/0201004.

[45] J. Pumplin et al., New generation of parton distributions with uncertainties from global QCD analysis, *JHEP* **07**, 012 (2002), hep-ph/0201195.

[46] Hep data base on-line calculation and graphical display http://durpdg.dur.ac.uk/HEPDATA/.

[47] Ashish Kumar, Manoj Kumar Jha, Bani Mitra Sodermark, Ashutosh Bhardwaj, Kirti Ranjan, and R. K. Shivpuri, Study of direct photon production at the CERN LHC, *Phys. Rev. D* **67**(1), 014016 (Jan 2003).

[48] L. Apanasevich et al., k(T) effects in direct photon production, *Phys. Rev.* **D59**, 074007 (1999), hep-ph/9808467.

[49] Several talks given at QM 2008 http://www.veccal.ernet.in/∼pmd/qm2008/webpage/qm2008Program.htm.

[50] B. Abbott et al., Determination of the absolute jet energy scale in the DØ calorimeters, *Nucl. Instrum. Meth.* **A424**, 352–394 (1999), hep-ex/9805009.

[51] A. Bhatti et al., Determination of the jet energy scale at the Collider Detector at Fermilab, *Nucl. Instrum. Meth.* **A566**, 375–412 (2006), hep-ex/0510047.

[52] H. Gray, The Gamma-Jet process as a calibration tool for jet analysis, *APS Meeting Abstracts* , D4+ (Oct. 2004).

[53] Introduction to Jet, EtMiss Reconstruction, and Calibration https://twiki.cern.ch/twiki/bin/view/Atlas/IntroductionToHadronicCalibration.

[54] D. V. Bandurin, V. F. Konoplyanikov, and N. B. Skachkov, Jet energy scale setting with 'gamma + jet' events at LHC energies: Selection of events with a clean 'gamma + jet' topology and P(t) (gamma) - P(t) jet disbalance, (2000), hep-ex/0011014.

[55] G. Aad et al., Jets and Missing Transverse Energy, Expected Performance of the ATLAS Experiment - Detector, Trigger and Physics, (2009), 0901.0512.

[56] A. D. Martin, R. G. Roberts, W. J. Stirling, and R. S. Thorne, Uncertainties of predictions from parton distributions. I: Experimental errors. ((T)), *Eur. Phys. J.* **C28**, 455–473 (2003), hep-ph/0211080.

[57] V. N. Gribov and L. N. Lipatov, Deep inelastic e p scattering in perturbation theory, *Sov. J. Nucl. Phys.* **15**, 438–450 (1972).

[58] Guido Altarelli and G. Parisi, Asymptotic Freedom in Parton Language, *Nucl. Phys.* **B126**, 298 (1977).

[59] Yuri L. Dokshitzer, Calculation of the Structure Functions for Deep Inelastic Scattering and e+ e- Annihilation by Perturbation Theory in Quantum Chromodynamics. (In Russian), *Sov. Phys. JETP* **46**, 641–653 (1977).

[60] L. N. Lipatov, Reggeization of the Vector Meson and the Vacuum Singularity in Nonabelian Gauge Theories, *Sov. J. Nucl. Phys.* **23**, 338–345 (1976).

[61] E. A. Kuraev, L. N. Lipatov, and Victor S. Fadin, Multi - Reggeon Processes in the Yang-Mills Theory, *Sov. Phys. JETP* **44**, 443–450 (1976).

[62] E. A. Kuraev, L. N. Lipatov, and Victor S. Fadin, The Pomeranchuk Singularity in Nonabelian Gauge Theories, *Sov. Phys. JETP* **45**, 199–204 (1977).

[63] I. I. Balitsky and L. N. Lipatov, The Pomeranchuk Singularity in Quantum Chromodynamics, *Sov. J. Nucl. Phys.* **28**, 822–829 (1978).

[64] Marcello Ciafaloni, Coherence Effects in Initial Jets at Small q^2 / s, *Nucl. Phys.* **B296**, 49 (1988).

[65] S. Catani, F. Fiorani, and G. Marchesini, QCD Coherence in Initial State Radiation, *Phys. Lett.* **B234**, 339 (1990).

[66] S. Catani, F. Fiorani, and G. Marchesini, Small x Behavior of Initial State Radiation in Perturbative QCD, *Nucl. Phys.* **B336**, 18 (1990).

[67] Giuseppe Marchesini, QCD coherence in the structure function and associated distributions at small x, *Nucl. Phys.* **B445**, 49–80 (1995), hep-ph/9412327.

[68] O. Cakir and Rashid R. Mehdiyev, Excited quark production at the CERN LHC, *Phys. Rev.* **D60**, 034004 (1999).

[69] Torbjorn Sjostrand, Stephen Mrenna, and Peter Skands, PYTHIA 6.4 physics and manual, *JHEP* **05**, 026 (2006), hep-ph/0603175.

[70] G. Corcella et al., HERWIG 6.5 release note, (2002), hep-ph/0210213.

[71] P. Aurenche, T. Binoth, M. Fontannaz, J.-P. Guillet, G. Heinrich, E. Pilon, and M. Werlen, http://wwwlapp.in2p3.fr/lapth/PHOX_FAMILY/jetphox_soon.html.

[72] Stefano Frixione and Bryan R. Webber, Matching NLO QCD computations and parton shower simulations, *JHEP* **06**, 029 (2002), hep-ph/0204244.

[73] Bo Andersson, G. Gustafson, G. Ingelman, and T. Sjostrand, Parton Fragmentation and String Dynamics, *Phys. Rept.* **97**, 31–145 (1983).

[74] Piotr Golonka and Zbigniew Was, PHOTOS Monte Carlo: A Precision tool for QED corrections in Z and W decays, *Eur. Phys. J.* **C45**, 97–107 (2006), hep-ph/0506026.

[75] G. Gustafson, Dual Description of a Confined Color Field, *Phys. Lett.* **B175**, 453 (1986).

[76] J. M. Butterworth, Jeffrey R. Forshaw, and M. H. Seymour, Multiparton interactions in photoproduction at HERA, *Z. Phys.* **C72**, 637–646 (1996), hep-ph/9601371.

[77] S. Alekhin et al., The Underlying Event, HERA and the LHC - A workshop on the implications of HERA for LHC physics: Proceedings Part A, (2005), hep-ph/0601012.

[78] P. Aurenche, M. Fontannaz, J.Ph. Guillet, E. Pilon, and M. Werlen, A new critical study of photon production in hadronic collisions, *Phys. Rev. D* **73**, 094007 (2006), hep-ph/0602133.

[79] DØ Collaboration, Measurement of the differential cross section for the production of an isolated photon with associated jet in ppbar collisions at sqrt(s)=1.96TeV, *Phys. Lett.* **B666**, 435–445 (2008), arXiv:0804.1107v2.

[80] S. Catani, M. Fontannaz, J.Pj. Guillet, and E. Pilon, Cross section of isolated prompt photons in hadron-hadron collisions, *JHEP* **05**, 028 (2002), hep-ph/0204023.

[81] S. Agostinelli et al., G4–a simulation toolkit, *Nuclear Instruments and Methods in Physics Research Section A: Accelerators, Spectrometers, Detectors and Associated Equipment* **506**(3), 250 – 303 (2003).

[82] Atlas trigger rates calculation
http://atlas-project-trigger rates.web.cern.ch/.

[83] Private Communication: V. Perez-Reale and M. Tripiana.

[84] S. Catani, Yuri L. Dokshitzer, M. Olsson, G. Turnock, and B. R. Webber, New clustering algorithm for multi - jet cross-sections in e+ e- annihilation, *Phys. Lett.* **B269**, 432–438 (1991).

[85] S. Catani, Yuri L. Dokshitzer, M. H. Seymour, and B. R. Webber, Longitudinally invariant K_t clustering algorithms for hadron hadron collisions, *Nucl. Phys.* **B406**, 187–224 (1993).

[86] Stephen D. Ellis and Davison E. Soper, Successive combination jet algorithm for hadron collisions, *Phys. Rev.* **D48**, 3160–3166 (1993), hep-ph/9305266.

[87] C. Buttar et al., Standard Model Handles and Candles Working Group: Tools and Jets Summary Report, (2008), 0803.0678.

[88] Matteo Cacciari, Gavin P. Salam, and Gregory Soyez, The anti-k_t jet clustering algorithm, *JHEP* **04**, 063 (2008), 0802.1189.

[89] Gavin P. Salam and Gregory Soyez, A Practical Seedless Infrared-Safe Cone jet algorithm, *JHEP* **05**, 086 (2007), 0704.0292.

[90] H. Jung et al., The ALFA Detector and Physics Program, Proceedings of the workshop: HERA and the LHC workshop series on the implications of HERA for LHC physics, (2009), 0903.3861.

[91] G. Aad et al., Introduction, Expected Performance of the ATLAS Experiment - Detector, Trigger and Physics, (2009), 0901.0512.

[92] http://hepforge.cedar.ac.uk/lhapdf/.

Glossary

p_{T} = Transverse momentum		$\rho = \sqrt{x^2 + y^2}$	$\eta = -\ln(\tan(\theta/2))$
s = centre of mass energy		$\Delta R = \sqrt{\Delta\eta^2 + \Delta\phi^2}$	z = Fragmentation energy fraction
CERN	European Organization for Nuclear Research		
ATLAS	A Toroidal LHC ApparatuS	LHC	Large Hadron Collider
LEP	Large ElectronPositron Collider	SLHC	Super Large Hadron Collider
Pixel	silicon pixel tracking detector	TRT	Transition Radiation Tracker
SCT	silicon microstrip, "Semi-Conductor Tracker"		
EM	ElectroMagnetic	HCAL	Hadronic CALorimeter
LAr	Liquid-Argon	HEC	Hadronic Endcap Calorimeter
MBTS	Minimum Bias Trigger Scintillators	FCAL	Forward CALorimeter
MDT	Monitored Drift Tubes	RPC	Resistive Plate Chambers
CSC	Cathode Strip Chambers	TGC	Thin Gap Chambers
ROI	Regions Of Interest	L1(2)	Level-1(2) trigger
EF	Event Filter	ACR	ATLAS Control Room
SC	Synchro Cursors	GUI	Graphical User Interface
ZMR	Zoom/Move/Rotate	L1calo	Level-1 calorimeter trigger
MINERVA	Masterclass IN Event Recognition Visualised with Atlantis		
LO	Leading Order	I/FSR	Initial/Final State Radiation
NLO	Next-to-Leading Order	JES	Jet Energy Scale
NNLO	Next-to-Next-to-Leading Order	PDF	Parton Density Function

Appendix A

$2 \rightarrow 2$ Kinematics

For a $2 \rightarrow 2$ decay ($1 + 2 \rightarrow 3 + 4$), as described in section 5.2, the particles have the following four momenta (E, p_x, p_y, p_z):

$$p_1 = \frac{\sqrt{s}}{2}(x_1, 0, 0, x_1) \qquad p_3 = p_T(cosh(\eta_3), cos(\phi), sin(\phi), sinh(\eta_3))$$
$$p_2 = \frac{\sqrt{s}}{2}(x_2, 0, 0, -x_2) \qquad p_4 = p_T(cosh(\eta_4), -cos(\phi), -sin(\phi), sinh(\eta_4))$$

Conserving energy and longitudinal momentum (using x_T as in equation 5.1):

$$x_1 = \frac{x_T}{2}(e^{\eta_3} + e^{\eta_4}) \tag{A.1}$$

$$x_2 = \frac{x_T}{2}(e^{-\eta_3} + e^{-\eta_4}) \tag{A.2}$$

$$\text{Rearranging equation A.2 gives : } \; e^{-\eta_4} = \frac{2x_2 - x_T e^{-\eta_3}}{x_T} \tag{A.3}$$

$$\text{Substituting into A.1 gives : } \; x_1 = x_T(\frac{e^{\eta_3} x_2}{2x_2 - x_T e^{-\eta_3}}) \tag{A.4}$$

Applying the constraint that $x_1 \leq 1$, gives the minimum value of x_2:

$$x_2 \geq \frac{x_T e^{-\eta_3}}{2 - x_T e^{\eta_3}} \tag{A.5}$$

which assuming $x_1 > x_2$ (i.e. $\eta_3, \eta_4 > 0$) will give x_{min}. Similarly this can be calculated from the Mandelstam variables with the constraint that $\hat{s} + \hat{t} + \hat{u} = 0$, in the massless limit, where:

$$\hat{s} = x_a x_b s \quad \hat{t} = -x_a p_T e^{-\eta_3}\sqrt{s} \quad \hat{u} = -x_b p_T e^{\eta_3}\sqrt{s}.$$

Appendix B

Generator Technicalities

In any generator, each particle type has a unique number (`PDGId`), for instance a photon has `PDGId=22`. As each particle is generated an identification number (`Barcode`) is incremented to indicate when it was added to the listing. Particles with a low `Barcode` are from the hard interaction, whereas large `Barcode` numbers come from the detector simulation, outlined in section 7.2. Each particle also has a status code (`ISTHEP`) to help distinguish the final state, i.e. detectable, particles from those produced as part of the simulation chain:

- `ISTHEP=1`: *A "final state" particle, which will not decay or fragment further in the simulated event.*
- `ISTHEP=2`: *A particle retained to preserve the full event record, which has decayed or fragmented so will not appear in the final state.*
- `ISTHEP=3`: *Referred to as a documentation particle, which usually means the incoming particles and those involved in the hard process.*
- `ISTHEP>3`: *Other documentation values used, specific to the generator.*

By using the `PDGId` and `Barcode` information all real (`ISTHEP=1`) photons from the generator can be selected. Photons with other status codes can help in distinguish-

ing which event process was generated. In Pythia a photon with `ISTHEP=3` is a photon emerging from the hard interaction, i.e. a direct photon. To appear in the final state this would then "decay" into a `ISTHEP=1` photon. In Herwig this status decay chain for a direct photon is slightly more complicated, following the chain: `ISTHEP`=124→144→2→157→1.

Appendix C

Full JetPhox Results

The results quoted here correspond to those in sections 6.6.1, 6.6.2 and 6.6.3, except that separate direct and one fragmentation contributions are given.

Table C.1: JetPhox contributions separated.

Run	direct		one fragmentation	
	Born σ (nb)	h.o. σ (nb)	Born σ (nb)	h.o. σ (nb)
0	70.3	15.3	80.4	13.3
1	70.4	15.3	80.4	13.3
2	52.9	89.7	56.7	75.0
3	70.3	14.5	94.4	66.4
4	70.3	68.5	10.5	97.7
5	70.4	73.0	80.9	26.6
6	70.3	15.4	80.4	13.3
7	91.4	-37.9	109.4	4.95
8	111.4	-105.2	142.7	-3.19
9	61.0	19.6	60.6	23.8

Run	direct		one fragmentation	
	Born σ (nb)	h.o. σ (nb)	Born σ (nb)	h.o. σ (nb)
10	54.0	21.5	47.4	26.9
11	91.4	-8.64	95.6	-2.83
12	111.4	-37.1	108.4	-18.2
13	70.3	-8.61	91.7	21.9
14	70.3	-32.5	104.4	31.9
15	79.5	103.2	11.8	19.0
16	79.5	121.2	11.8	21.7
17	79.5	128.5	8.8	18.2
18	79.5	67.3	44.9	37.9
19	79.5	39.4	82.8	39.8
20	79.5	103.2	11.8	19.0
21	79.5	109.3	8.8	15.9
22	79.5	59.7	44.9	34.1
23	79.5	38.4	82.8	38.2
24	79.5	84.5	11.8	16.2
25	79.5	89.4	8.8	13.6
26	79.5	51.9	44.9	30.2
27	79.5	37.3	82.8	36.5
28	79.5	67.7	11.8	13.6
29	79.5	71.1	8.8	11.4
30	79.5	45.2	44.9	26.6
31	79.5	36.5	82.8	35.0
32	79.5	54.7	11.8	11.4
33	79.5	56.7	8.8	9.5
34	79.5	40.4	44.9	23.6
35	79.5	35.9	82.8	33.7
36	79.5	35.5	94.5	33.9

Table C.2: Cross-sections from JetPhox after combining parameter choices from table 6.4 to create a final selection.

Addition	direct		one fragmentation		Total
to default	Born σ (nb)	h.o. σ (nb)	Born σ (nb)	h.o. σ (nb)	σ (nb)
+ run 5	70.4	73.0	80.9	26.6	251
+ run 9	61.2	62.4	60.9	32.4	217
+ run 7	79.5	37.6	82.8	36.4	236
+ run 6	79.5	37.3	82.8	36.5	236
+ run 1	79.5	37.3	82.8	36.5	236
+ run 4	79.5	103.2	11.8	19.0	214

Appendix D

Reconstructed Samples

D.1 Photon Filter

In the LO direct photon samples the photon filter requires at least 1 photon with $p_{\mathrm{T}} > 10$ GeV and $|\eta| < 2.7$. The fraction of events that pass this filter, compared with all events generated in the larger phase space with $|\eta| < 10$, is shown in table D.1. The fraction increases with p_{T} as the η plateau narrows with increasing p_{T}. The results from the filter have already been included in the cross-sections in table 6.3 to correspond to the required η range.

Table D.1: Fraction of LO direct photon events that pass the photon filter out of all generated.

p_{T} Region (GeV)	Herwig	Pythia	p_{T} Region (GeV)	Herwig	Pythia
17-35	0.57	0.56	140-280	0.94	0.93
35-70	0.68	0.66	280-560	0.99	0.99
70-140	0.82	0.81	560-1120	1.00	1.00

D.2 Combined Samples

As already stated in 7.4, the combined sample was originally designed to study the backgrounds for all electron/photon signatures. As well as containing both di-jet and LO direct photon processes it also has other additional processes (each with a unique process number `PYSUBS msub`), which are:

- `PYSUBS msub 1`: $f\bar{f}\rightarrow\gamma^*/Z$
- `PYSUBS msub 2`: $f\bar{f}\rightarrow W^{\pm}$
- `PYSUBS msub 81`: $f\bar{f}\rightarrow Q\overline{Q}$
- `PYSUBS msub 82`: $gg\rightarrow Q\overline{Q}$

where the Q and $\overline{Q}$ flavours are set to be the heaviest quark flavour. Table D.2 shows the effect of adding the above processes into the di-jet samples (in two example p_{T} ranges: 17 to 35 GeV and 140 to 280 GeV). In both cases the influence of the extra processes on the cross-section is negligible.

Table D.2: Di-jet sample cross-sections with and without extra processes found in the combined sample.

p_{T} range	Extra processes	σ (nb)
17 to 35 GeV	without	1.378×10^{6}
17 to 35 GeV	with	1.383×10^{6}
140 to 280 GeV	without	3.149×10^{2}
140 to 280 GeV	with	3.165×10^{2}

From these extra processes there may be extra photons produced, for example radiative photons from the quarks produced in processes 81 and 82. However, as these produce a difference of only $\sim$1% on the cross-section it is unlikely to make a noticeable difference overall, when comparing results from the individual di-jet and

LO direct photon samples to that of the combined sample. Should the measurement ever get to an accuracy around the percent level then a more in-depth study of the truth particles in each event of the combined sample should be carried out, but below this level of accuracy the combined sample should be comparable to the separate samples.

D.2.1 Jet filter

As well as checking the other processes inside the combined sample the jet filter needs to be checked to see that it doesn't remove the LO direct photon events. There are actually three versions of the combined sample, where the sample chosen for this analysis has the lowest p_{T} cut and largest statistics. The samples have minimum p_{T} cuts of 15 GeV and 33 GeV on the hard processes, which are followed by the (two tight and one loose) jet filter cuts of 17 GeV and 35 GeV, respectively, along with both requiring one jet in the region of $|\eta| < 2.7$. The "default" results in table D.3 summarise these different samples and the number of events that pass the selected filter. The effect of this filter on direct photon events is investigated by re-running the combined sample setup with LO direct photons removed ("no photon") and on their own ("only photon"). This shows that removing the LO direct photon processes has negligible effect on the sample cross-section. When producing just LO direct photon events, a similar fraction passes the jet filter compared to the photon filter in section D.1 and it also shows that LO direct photons are far more likely to pass the jet filter than the di-jet events. This could create a different ratio of signal to background for the same cross-section, when comparing to the individual LO direct photon and di-jet samples. However as LO direct photons have a far lower cross-section overall this effect should be small.

Table D.3: Analysis of the jet filter for the different combined samples, see text for details.

p_{T} cut	Run	Filter	σ (nb)	Pass %	Filtered σ (nb)
$p_{\mathrm{T}} > 17$ GeV	default	Tight	2.31×10^{6}	8.22	1.90×10^{5}
$p_{\mathrm{T}} > 17$ GeV	no photon	Tight	2.32×10^{6}	8.48	1.96×10^{5}
$p_{\mathrm{T}} > 17$ GeV	only photon	Tight	4.20×10^{2}	45.09	1.89×10^{2}
$p_{\mathrm{T}} > 35$ GeV	default	Tight	1.29×10^{5}	15.98	2.07×10^{4}
$p_{\mathrm{T}} > 35$ GeV	no photon	Tight	1.29×10^{5}	15.92	2.06×10^{4}
$p_{\mathrm{T}} > 35$ GeV	only photon	Tight	3.64×10^{1}	58.55	2.13×10^{1}
$p_{\mathrm{T}} > 35$ GeV	default	Loose	1.29×10^{5}	30.55	3.96×10^{4}
$p_{\mathrm{T}} > 35$ GeV	no photon	Loose	1.29×10^{5}	30.65	3.97×10^{4}
$p_{\mathrm{T}} > 35$ GeV	only photon	Loose	3.64×10^{1}	63.15	2.30×10^{1}

Appendix E

Identification Efficiency Uncertainty

To justify using the approximation that the photon identification error is the same as that for an electron, the isEM selection can be varied to see if it results in a similar sized shift in the identification efficiency. To vary the isEM selection it first had to be replicated using the available information in the software environment used. For technical reasons this was not a perfect replication of isEM selection, but was accurate to 99.8%[†].

Before varying the values of the isEM cuts, see section 7.6.1, the correlation between the isEM variables is investigated, as shown for selected example variables in figure E.1. From this study it is clear that some of the second layer and strip variables are correlated, so these variables are altered at the same time as well as independently.

To look at the sensitivity of isEM to each variable a shift of 1% was applied to each value. Although this 1% shift is to some extent arbitrary, it is a reasonable level of variation as most of the variables contributing to isEM are based on energy

[†]This was because it was based on the photon p_{T} and η rather than the cluster p_{T} and η.

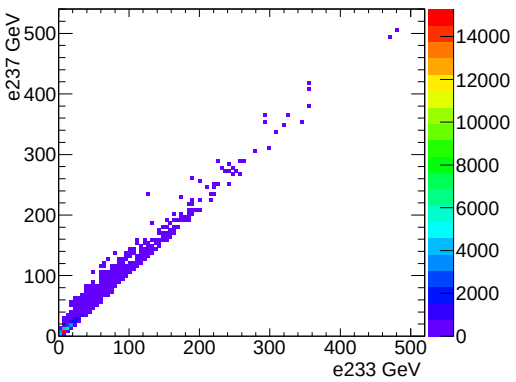

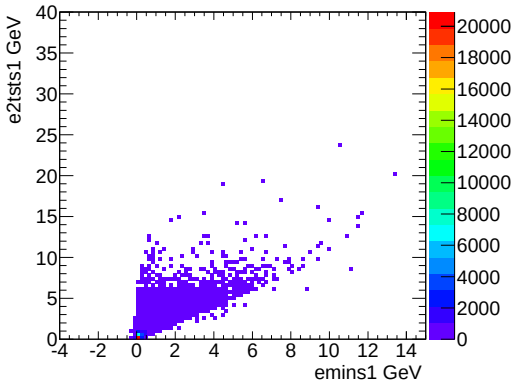

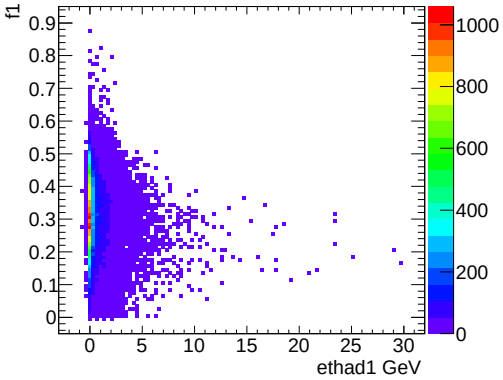

Figure E.1: Correlation between selected isEM variables.

or η measurements, which as already discussed should be accurate to roughly the 1% level. Table E.1 shows the change in the number of events passing isEM as a result of each shift. The differences in number passing from the upward and downward shifts are then averaged for each variable. By summing the averaged differences in quadrature, the total isEM difference in number of events passing isEM is 7.38%. However, as mentioned above, this does not take into account the strong correlations in some of the variables in particular, those at the bottom of table E.1. Altering correlated variables at the same time, rather than independently, reduces the difference to 3.2% .

These results are actually independent of what the reconstructed photon actually represents, i.e. this combines signal and background photons. Repeating this procedure for more signal-like selections resulted in an error of $\sim$ 3%, with and without taking account for the correlated variables as above. The results show that the largest error is from `ratio1` (`e237`/`e277`), but by construction this disappears when the correlated errors are considered. A better method to account for the correlations would involve altering the material in front of the calorimeter but this is a more technically difficult measurement. Similarly the 1% shift should be replaced with more shifts representative of the real errors on each variable. However, the resulting 3% difference in isEM is comparable to the 5% difference based on electron measurements or the 6% difference from using a different photon selection.

Table E.1: Shift in the number of events passing isEM cuts when varying the variables independently. Correlations are also considered for `e277`+`e237`+`e233` (replacing `ratio1` and `ratio2`) and `etmins`+`e2tsts1` (replacing `emax2r` and `deltae`). The % change values are compared to the 40824 events that pass the reproduced isEM.

	Apply 1% shift up		Apply 1% shift down		
Variable(s)	Number pass	% change	Number pass	% change	Average % change
η	40795	-0.071	40827	0.007	0.039
p_{T}	40807	-0.042	40829	0.012	0.027
`hadleakage`	40720	-0.255	40934	0.269	0.262
`e277`	40824	0.000	40824	0.000	0.000
`ratio1`	43043	5.436	37613	-7.865	6.651
`ratio2`	40864	0.098	40762	-0.152	0.125
`weta2`	40354	-1.151	41167	0.840	0.996
`iso`	40824	0.000	40824	0.000	0.000
`f1`	40828	0.010	40823	-0.002	0.006
strips η	40184	-1.568	41270	1.092	1.330
`emax2r`	40794	-0.073	40852	0.069	0.071
`deltae`	40783	-0.100	40866	0.103	0.102
`wtots1`	40243	-1.423	41273	1.100	1.262
`fracs1`	40529	-0.723	41079	0.625	0.674
`weta1`	39785	-2.545	41672	2.077	2.311
`e277`+`e237`+`e233`	40824	0.000	40824	0.000	0.000
`etmins`+`e2tsts1`	40753	-0.174	40894	0.171	0.173